Water-rock-microbe interactions in hydrothermal chimneys: Insights from reaction transport modeling

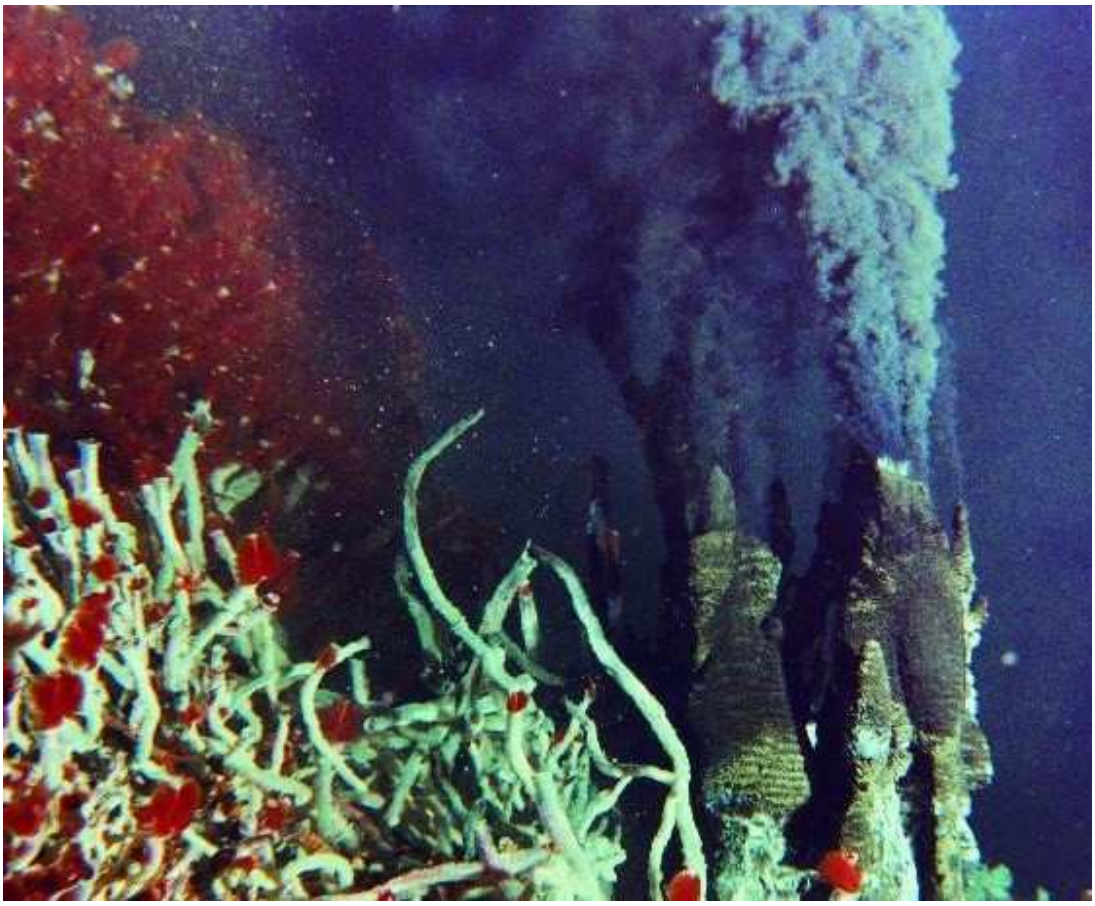

Nicole Geerlings, 0304220

Contents

1. Abstract

A 1-dimensional model of transport and chemical reaction is gradually developed to examine the interactions between pore fluid, microbial metabolism and mineral composition in the porous wall of a hydrothermal vent chimney. Diffusion and advection yield steady state profiles of temperature and concentration across a layer of anhydrite with constant porosity bound on one side by hydrothermal fluid and on the other by seawater. Slow reaction kinetics for redox reactions among S and C compounds resuls in chemical disequilibrium which chemoautotrophic microbes are capable of exploiting. The metabolisms of these microbes can be decribed by a redox reaction; methanotrophy, methanogenesis, anoxic oxidation of methane, sulfate reduction, sulfide oxidation have been implemented in the model.
Model calculations indicate that the large temperature gradient between the boundary on the hydrothermal vent side and seawater side has the most effect on the distribution of microbial metabolisms in the vent chimney. The large temperature gradient affects diffusion and advection rates, which are both temperature dependent. Besides temperature, the reaction rate constant of the bimolecular rate laws used to describe microbial metabolism affect the type of microbes that will be present at the hydrothermal vent.

2. Introduction

Hydrothermal systems are located at mid-ocean ridges and include features such as black smokers, white smokers and ecosystems that are independent of sunlight as a source of reducing power (Holm 1992). The presence of hydrothermal systems at mid-ocean ridges is a consequence of the injection of magma and its subsequent solidification and cooling (Shock 1992). In submarine hydrothermal systems, the biological communities receive no input of exogenous organic matter from photosynthesis, but exist primarily on the energy supplied by the geological environment. Because they do not require input of photosynthetic organic matter, they may represent analogues of the earliest biological communities to inhabit the Earth. Many chemolithoautotrophic communities exist in reducing environments with H_2 as the primary electron donor. There may be an energetic advantage to autotrophic growth in anoxic environments arising from the smaller amounts of energy required for synthesis of biomolecules under reducing conditions (McCollum and Amend 2005).

Chemolithoautotrophic organisms derive metabolic energy from the catalization of inorganic chemical reactions that are out of equilibrium due to kinetic factors. The potential for growth and reproduction of these chemolithoautotrophic organisms depends on how efficiently they can convert the available energy into biomass, and how they minimize the amount of energy lost as heat or organic by-products (McCollum and Amend 2005).

Hydrothermal fluids are generated in the vicinity of mid-ocean ridges and oceanic hot spots through the interaction of seawater with hot basalt erupted at or near the seafloor surface, They are hot, acidic, highly reduced and metal- and sulfide enriched in comparison to seawater. Venting of hydrothermal fluids occurs at both high-temperature (250-400°C) and low-temperature (~8-40°C) vents (McCollum and Shock 1997). This research will focus on high temperature hydrothermal vent systems only. Mixing of high-temperature (250-400°C) hydrothermal fluids with seawater results in the precipitation of minerals and the formation of chimney-like structures of sulfide and sulfate minerals, the so-called black smokers. During mixing, the slow reaction kinetics for redox reactions among S, C, Fe, and Mn compounds results in chemical disequilibrium which chemolithotrophic microorganisms can exploit for metabolic energy (McCollum and Shock 1997).

The fluid venting from black smoker chimneys at mid-ocean ridges is connected through fracture systems to seawater and is at hydrostatic pressure (Holm 1992; Shock 1992). Chimney walls are sufficiently permeable to allow escape of hydrothermal fluids by diffusion and advection as well as the influx of seawater, and mixing between seawater and hydrothermal fluids occurs within the interstices of the chimney wall (McCollum and Shock 1997). Fluid flow rates up to 10 l sec^{-1} are common in black smoker vents (Shock 1992).

Pressures from a few hundred bars to several kilo bars and temperatures from 2°C (deep seawater) to at least 900°C can be encountered in submarine hydrothermal systems. When temperature and pressure reach a certain level, H_2O may become supercritical. The critical point of seawater is somewhat higher than that of pure H_2O due to the properties of salt solutions (Shock 1992).

The interactions between the cold seawater and the hot, metal- and sulfide-rich vent fluids exert primary control on environmental conditions (e.g. pore fluid temperature, pH and chemical composition) within and at the exteriors of vent deposits. Conversely, these environmental conditions affect flow through pore space and connectivity. Processes such as mineral precipitation and dissolution modify the fluid flow, altering environmental conditions. Mineral precipitation (and dissolution and/or thermal cracking) changes pore geometry, which in turn

modifies directions and magnitudes of fluid flow. Mixing and fluid flow are extremely important in determining the saturation state of minerals at various points within the structure and whether conditions are suitable for organisms (on micro-, macro and mega-scale) within and on the vent structure (Zhu, Tivey et al. 2007).
The physical environment places constraints on the energy available to microorganisms but the ultimate source of energy for vent communities comes from the chemical differences between seawater and hydrothermal vent fluids. The primary control on the energetic requirements is the oxidation state of the environment (McCollum and Shock 1997).

The development of hydrothermal chimney structures at deep-sea vents can be divided into three general stages: initial precipitation of a permeable, diffuse shell (stage I), mineralogical maturation and solidification (stage II), and aging of the structure as venting ceases (Schrenk, Holden et al. 2008). The early stages of black smoker chimney growth are characterized by the emplacement of porous anhydrite ($CaSO_4$) walls that contain fine inclusions of sulfide minerals. Once in place, the anhydrite walls act to partially isolate hydrothermal fluids from seawater, resulting in stage II growth, which includes deposition of an inner lining of Cu-Fe sulfides, the precipitation of sulfides and anhydrite within pore spaces, and consequently a decrease in wall permeability. A final stage in the history of a seafloor vent deposit is its eventual cessation of hydrothermal discharge and collapse (Schrenk, Holden et al. 2008).

At present, hydrothermal vents are the sites of some of the most rapid production of biomass of any ecosystems on the Earth (Lutz and Kennish 1993). The flow of metabolic energy is the most fundamental property governing ecosystem structure and the productivity of hydrothermal chemolithoautotrophic communities is limited by the availability of these exploitable chemical energy sources (McCollum and Amend 2005).
Little is known about the ecology of high-temperature hydrothermal vent systems, which is mainly due to their inaccessibility. In order to place constraints on the metabolic systems present in these vent environments, studies of fluid chemistry and geochemical models of the mixing between hydrothermal fluids and seawater provide a means to study microbial habitats and may assess the metabolic energy available from chemolithoautotrophic reactions (McCollum and Shock 1997). The understanding of the different mechanisms and feedbacks within hydrothermal vent systems are of great importance in understanding which metabolic pathways might be possible.
Information about submarine hydrothermal systems comes from many directions. Measurements made directly on venting fluids provide useful, but limited, clues about processes operating at depth (Shock 1992). Because so few vents have been sampled and studied thoroughly, determination of the underlying patterns and controls on the distribution of microbes in a hydrothermal vent chimney remains challenging. Although it is generally accepted that the composition of microbial populations changes with temperature and geochemistry, spatial and temporal linkages between hydrothermal vent microorganisms and fluid discharge and chemistry are only beginning to emerge (Huber and Holden 2008).
The primary types of microorganisms observed and studied in diffuse hydrothermal fluid discharge using molecular, microscopic, and culturing techniques are sulfide- and iron-oxidizing proteobacteria, epsilon-proteobacteria, Aquificales, methanogens, anaerobic methane oxidizers, sulfate reducers and Thermococcales (Huber and Holden 2008). The proteobacteria, epsilon-proteobacteria and Aquificales are all members of the bacterial domain while the methanogens, anaerobic methane oxidizers and Thermococcales belong to the phylogenetic group of the Archaea. Sulfate reducers have been detected in both the Archaeal and Bacterial domain.
With the exception of the Thermococcales, which are obligate heterotrophs, all of the primary types of microorganisms observed in diffuse hydrothermal systems can be primary producers;

some are obligate autotrophs (e.g. methanogens) while others can grow both autotrophically and heterotrophically (e.g. sulfate reducers).

Conceptual models are needed for the interpretation of the experimental data and field observations while mathematical and numerical models allow integration of the hydrothermal processes into a quantitative framework. Due to the complexity of the multiple, interconnected, non-linear and time dependent processes that occur over a broad range of temporal and spatial scale at ocean spreading centers, this quantitative modeling is a difficult task and the present mathematical models within the microbial biosphere are still at a developmental stage (Lowell, Seewald et al. 2008).

2.1 State of the art

Reactive transport models integrate natural processes, field observations, and laboratory experiments into one theoretical framework. Processes incorporated into the model framework influence the evolution and the distribution of properties in the system to varying degrees. Therefore, reactive transport simulations are an excellent tool to investigate the role and relative importance of fundamental processes in hydrothermal vent systems.
Reactive transport models have been developed by merging two different modeling approaches. The first approach emphasizes the physical aspects of the geological environment such as fluid, gas, solid and heat transport while keeping the formulation of the chemical fluid/rock interaction simple or even absent. The second modeling approach focuses on the development and application of quantitative models for (irreversible) chemical reactions, which is mainly the interaction between fluid (seawater and hydrothermal fluid), rock and microbes. Fluid/rock reactions can be initiated through changes in the rock composition when a fluid that is buffered by a mineral assemblage comes in contact with another mineral assemblage. Fluid/rock interactions also occur when the rock composition is uniform but if the fluid is in disequilibrium with the rock. Both processes lead to reaction zones in the rock that move through space and evolve through time. If the rock composition is uniform, reactions can also be initiated by fluids carrying solutes along a temperature and/or pressure gradient. Another way for reaction to occur is when two (or more) fluids mix (Alt-Epping and Diamond 2008). In hydrothermal systems, all of the above described fluid/rock interactions occur and they often occur simultaneously.

The first models trying to reproduce hydrothermal vent systems and chimneys were produced in the mid-eighties. The first ones to use modeling to reproduce mineral assemblages observed in and around a sulfide chimney were Janecky and Seyfried (1984), who used the EQ3/6 software developed by Wolery (1978) to make equilibrium path calculations where increments of seawater were added to hydrothermal vent fluid. The resulting mineral composition was comparable to the actual mineral composition found at 21°N, EPR. After that, the EQ3/6 software has been used by many other scientists to look in greater detail at hydrothermal vent systems (Bowers et al., 1985; Bowers and Taylor, 1985).
Most numerical models have, so far, treated physical and chemical processes in hydrothermal vent systems either independently or have linked these processes by simplifying either on or the other. Despite the decoupling of physical and chemical processes, the models for hydrothermal systems have been successful in reproducing main observations such as temperature profiles and the order of mineral precipitation (Alt-Epping and Diamond 2008). Thus, much of the observed chemistry and mineralogy of hydrothermal vent chimneys can by explained by mixing of the hot hydrothermal fluids with seawater. However, these models remain limited since a simple

reaction path calculation does not consider the physical environment (e.g. porosity, tortuosity, thermal diffusivity) nor do they consider the biological environment.

However, the results from speciation and reaction path models suggest that the thermodynamic database developed initially by Helgeson and coworkers, extended by Wolery and others (EQ3/6) and now compiled in SUPCRT92 (Johnson, Oelkers et al. 1992), produces results that agree quite well with observations from various sites and settings over large ranges of temperature. The SUPCRT92 database will also be used in this research.

Reactive transport models for hydrothermal vent chimneys that link the physical environment and the chemical processes are sparse. The main reactive transport modeling in black smoker chimneys is done by Tivey and McDuff (1990) and Tivey (1995). They developed a quantitative model of transport and reaction to examine the interplay of physical and chemical processes controlling the evolution of black smoker chimneys. Tivey and McDuff (1990) explicitly provided variations in porosity, tortuosity, diffusion coefficients and concentration gradients. By doing this they were able to re-create the aging of black smoker chimneys inferred from petrologic studies. The study of Tivey (1995) extends the model developed in 1990 by examining the sensitivity of the mineral assemblages to differences in end-member fluid composition, and to rates of advection. Again, they managed to reproduce mineralogy found in different vent sites. What they did not include were biological processes carried out by chemolithotrophs. The models from developed by Tivey and coworkers demonstrate the sensitivity of the thermal and chemical gradients within the chimney walls to characteristics of the environment, in particular to those which influence mass transport such as rock porosity and permeability. The thermal and chemical gradients of black smoker chimney walls are impacted by both advection and diffusive transfer of heat and mass (Tivey and McDuff 1990; Tivey 1995). The thermal and chemical gradients, and mineralogical framework found within sulfide deposits are predicted to be the important determinants for the microbial ecology of such structures (McCollum and Shock 1997; Schrenk, Holden et al. 2008).

The significance of biological processes has been recognized over the past years as has the need to relate these processes to hydrological, thermal, and chemical models. To some extent, this has been done by McCollum and Shock (1990) who developed a thermodynamic mixing model to investigate the amount of Gibbs free energy available for different types of chemolithoautotrophic microorganisms at different mixing ratios between end-member hydrothermal fluid and ambient seawater. They found that, for the vent fluid used in their calculations (21°N, EPR), the mixing environments are favorable for oxidation of H_2S, CH_4, Fe^{2+} and Mn^{2+} at lower temperatures and methanogenesis and sulfate reduction at higher temperatures. They predict that thermophilic methanogens and sulfate reducers are most likely to be the predominant organisms in the walls of vent chimneys (McCollum and Shock 1998). What they did not include was the effect of the physical environment.

The current needs for modeling the impact of microorganisms on diffuse fluids and the subseafloor are to predict community composition, microbial distribution, rate of biogeochemical reactions, and biomass production. These must be coupled with the development of first-order flow models with varying physical and chemical constraints for the purpose of modeling the impact of microbial communities on fluid flow, rock properties and mineral composition (Huber and Holden 2008). The current knowledge of what type of microbes are present and how they are distributed over time and space in the dynamic geochemical environment that are hydrothermal vent chimneys is fragmentary. The development of fluid flow models of diffuse hydrothermal fluids and the organisms found within them will provide first-order estimates of what microbial processes are occurring within the vents.

Understanding the microbe-mineral interactions within hydrothermal vent deposits (i.e. chimneys) may be critical to evaluating the extent of habitable space within subseafloor environments and the impact of microorganisms within rock-hosted deep-sea ecosystems on global biogeochemical cycles. However, this will ultimately require the development of reactive

transport models that couple fluid flow, heat transfer, solute transport, geochemical reaction, and microbiological processes (Schrenk, Holden et al. 2008).
In this thesis, a one-dimensional reactive transport model is gradually developed that integrates the physical and chemical environment within a black smoker chimney. This includes chemolithoautotrophic reactions. The model focuses on transport and biogeochemical reactions and the feedback between microbial ecology and geochemistry.
Model calculations are used to illustrate which metabolic pathways are possible under certain conditions. The outcome of the models will be compared to field data experimental data and outcomes from the models described above.

3. Model set-up

This chapter described the model set-up for the final reactive-transport model (RTM) that simulates which metabolic pathways are possible under the physical and chemical conditions of a typical hydrothermal vent chimney (i.e. black smoker). RTMs provide the ground for predicting geochemical, biological and transport processes by integrating experimental, observational and theoretical knowledge (Aguilera D.R., Jourabchi P. et al. 2005) and are thus perfect for describing an hydrothermal vent chimney.
The porous layers of vent structures may be viewed as analogous to sedimentary layers subjected to diagenesis. One-dimensional transport of heat and mass across these layers depend on the temperatures, concentrations, and pressures that exist on either side of the wall, as well as the composition, porosity and permeability of the wall (Tivey and McDuff 1990).
The metabolic pathways are described by a simple redox reaction. The physical and chemical conditions described in this model are all taken from literature.

The model is developed in the web-distributed Knowledge-Based Reactive Transport Model (www.geo.uu.nl/~kbrtm) developed by Aguilera et al. (2005). With this modeling approach it is possible to implement complex reaction networks in RTMs. The selected reaction network is merged with existing transport models, creating a framework to assemble RTMs.

3.1 Partial differential equations

The core of a simulation experiment is a set of equations which describe the coupled processes of interest. These processes include hydrodynamic flow, solute transport, and biogeochemical reactions (Regnier, O'Kane et al. 2002).
A continuum representation of coupled mass transport and chemical reactions can be described mathematically by a set of partial differential equations (PDE's) in time and space (Regnier, O'Kane et al. 2002). Temperature and concentration (mass transport) as a function of position x within the chimney wall is calculated using a finite difference method, solving the partial differential equations (PDE's) (Tivey 1995).

$$\frac{\partial T}{\partial t} = \frac{\partial}{\partial x}(\kappa \frac{\partial T}{\partial x}) - \varphi u(\frac{(\rho C_p)_l}{(\rho C_p)_m}\frac{\partial T}{\partial x} = 0 \qquad (1)$$

$$\varphi \frac{\partial C_i}{\partial t} = \frac{\partial}{\partial x}(D_i^n \frac{\partial C_i}{\partial x}) + \frac{\partial}{\partial x}(D_i^n C_i \frac{\partial \ln \gamma_i}{\partial x}) - \varphi u(\frac{\partial C_i}{\partial x}) + \varphi \sum R_i = 0 \qquad (2)$$

Where T is temperature, t is time, κ is thermal diffusivity, φ is porosity, u is average linear velocity of fluid, ρ is density, C_p is the specific heat capacity, subscripts l and m denote the liquid and porous medium, D^n is the product of the sediment diffusion coefficient ($D^{'}$) and porosity, C is concentration, γ is the activity coefficient and R is the rate of all chemical reactions affecting species i.
Thermal diffusivity of layers within a hydrothermal vent are estimated by considering thermal conductivities, densities, specific heat capacities, proportions, and geometric arrangements of minerals and fluid that comprise each layer. Sediment diffusion coefficients are a function of temperature, tortuosity, and ionic strength (Tivey 1995).

3.2 Energy

The occurrence of a specific metabolic pathway depends on the amount of metabolic energy that is potentially available to a microorganism from a chemical reaction. Since pressures are hydrostatic, Gibbs free energy can be used to calculate the potential energy available:

$$\Delta G = \Delta G^0 + RT \ln Q \tag{3}$$

Reaction that are exergonic (i.e. $\Delta G<0$) give off energy as they proceed and may provide energy for microbial metabolism. The amount of potential energy available from the previous chemical reactions can be calculated by using the Gibbs free energy by taking into account the temperature dependence of ΔG^0 and accounting for changes in composition of the fluid during mixing. Q is the activity product of the compounds involved in the reaction and is thus a function of the fluid composition, but is also governed by mineral composition and gases present (Shock, McCollum et al. 1993). Since ΔG^0 is a function of pressure and temperature, ΔG is a function of P, T and fluid composition. Fluid compositions change as a result of the mixing between the hydrothermal fluid and the seawater which results in changes in ΔG and thus the potential energy available for certain metabolisms.
Values of ΔG^0 are calculated by summing the standard Gibbs free energies of formation of the individual compounds involved in the reaction

$$\Delta G^0 = \sum \Delta G^0_{f,products} - \sum \Delta G^0_{f,reactants} \tag{4}$$

Temperature changes with position in the hydrothermal vent due to mixing between hydrothermal fluid and seawater, this will affect the Gibbs free energy and thus the potential energy that is available to a microbe. For example, sulfide oxidation is most favorable at low temperature and becomes less energetically favorable with increasing temperature due to decreasing availability of O_2 as seawater mixes with the oxygen depleted hydrothermal vent fluid. Sulfate reduction becomes more favorable with increasing temperature due to increasing contribution of the H_2 and sulfide-rich vent fluid (McCollum and Shock 1997). Precipitation of sulfide or sulfate minerals or the spontaneous abiotic oxidation of H_2S or reduction of sulfate will reduce the amount of energy available for the microbial metabolism of sulfide oxidizers.
A simple reaction path model will not be sufficient to model the potential energy gain for different metabolisms since it does not take into account the physical conditions of the system (e.g. porosity, tortuosity, permeability, thermal diffusivity).

3.3 Transport of heat and mass across the chimney wall

Transport calculations in the model describe the steady state profiles of temperature and mass across a chimney wall of 3 cm and a constant porosity of 0.3. The chimney wall is bound on one side by 350°C hydrothermal fluid with a composition found in EPR 21°N and on the other side by seawater of 2°C with a composition of modern, deep seawater (table 1). A depiction of the hydothermal vant can be seen in figure 1.
It is assumed that conditions (concentrations and temperature) at the boundaries of the chimney wall remain constant with time (Dirichlet boundary condition). Boundary conditions place the model in its environmental context (Boudreau 1997). The fluids at the inner wall are constantly being replenished by m/s flow in the chimney channel. Rates of transport are high owing to large

gradients, high porosity and short length scales. Due to this, reactions do not significantly alter concentration profiles and local equilibrium is not archieved.
Due to the increased temperatures and pressures at the hydrothermal vent sides, the hydrothermal fluid being emitted is still in its liquid state, but the density is not as high as water under standard state. Therefore, concentrations are given in mmol kg^{-1} of porewater instead of mmol L^{-1} of porewater.

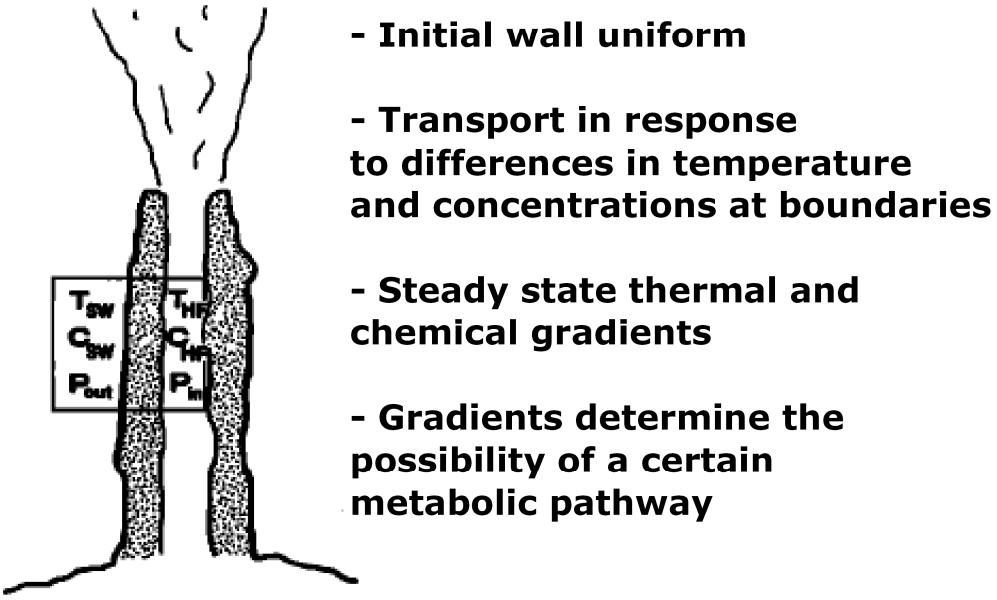

Figure 1: *Depiction of a hydrothermal vent chimney (Tivey and McDuff 1990) showing boundary conditions for model calculations, and describing feedback between transport and the metabolic pathways. HF and SW denote hydrothermal fluid and seawater, respectively.*

Species	EPR 21°N (mmol kg^{-1})	Seawater (mmol kg^{-1})
$CH_4(aq)$	0.112	0.0
$CO_2(aq)$	5.9947	0.0699
$HCO_3^-(aq)$	0.0053	2.2743
$CO_3^{2-}(aq)$	0.0	0.0157
$O_2(aq)$	0.0	0.0754*
$H_2(aq)$	2,716	0.0
$H_2S(aq)$	11.6536	0.0
$HS^-(aq)$	0.0074	0.0
$SO_4^{2-}(aq)$	0.0	28.3
Ba^{2+}	0.01	0.00014
Ca^{2+}	16.6	10.2
Cu^{+}	0.0097	0
Fe^{2+}	0.75	0
Pb^{2+}	0.000194	0
Zn^{2+}	0.089	0
pH	3.23	7.8
Temperature	350°C	2°C

Table 1: *Compositions of EPR 21°N vent fluid and seawater used in model calculations (Tivey and McDuff 1990).*
**from McCollum and Shock (1997)*

3.3.1 Transport of heat

When only transport by diffusion is taken into account, the change in temperature over time can be described by the simplified partial differential equation

$$\frac{\partial T}{\partial t} = \frac{\partial}{\partial x}(\kappa \frac{\partial T}{\partial x}) \tag{5}$$

Where κ is the thermal diffusivity constant, which can be calculated by the following formula

$$\kappa = \frac{\lambda}{(\rho C_p)_m} \tag{6}$$

Where $(\rho C_p)_m$ is the thermal capacity (at constant pressure) which is assumed to be approximately constant with temperature, but a function of layer composition. The volumetric heat capacity is calculated by weighting ρC_p of phases present within each layer based on their volume proportions. The parameter C_p is the specific heat capacity (J kg^{-1} K^{-1}) at constant pressure, which is the amount of heat required to raise the temperature of one unit mass of that substance by 1° (or K). The specific heat capacity of water is dependent on temperature but this can be neglected

as long as the pressure is high enough to keep the water in its liquid phase (Waples and Waples 2004). Assumed is that the pressure is a constant 250 bar and temperatures vary between 2°C and 350°C. Under these conditions, water does not become supercritical but remains in the liquid phase (see figure 1).
The specific heat capacity of saline water is slightly lower than that of pure water but the difference is too small to be of significance in modelling, waters of all salinities are assumed to have the same specific heat capacity (Waples and Waples 2004).
In the formula for thermal diffusivity, λ is the thermal conductivity. Thermal conductivity of a porous layer is a function of the minerals and fluid that comprise the wall, the geometry of pore spaces, minerals, and cracks; it is also influenced by temperature and pressure (Tivey and McDuff 1990).
Simple relationships between rock type and thermal conductivity exist, but these are not applicable when porosity exceeds 10% due to the introduction of large errors. When no direct measurements can be performed, which is the case for black smoker chimneys, thermal conductivity can be inferred from a number of indirect data (Clausen and Huenges 1995). Thermal conductivity decreases significantly with increasing porosity and temperature, but these effects are overshadowed by the high conductivity of sulfide relative to sulphate, the former always being three times more conductive. This contrast in thermal conductivities determines the nature of the temperature gradient across the chimney wall following deposition of an inner sulfide layer. Prior to deposition of significant amounts of sulfide, temperature effects on thermal conductivity dominate (Tivey and McDuff 1990). In our model, the chimney is believed to be comprised of pure anhydrite ($CaSO_4$), which means that the temperature effect dominates the thermal conductivtity
The thermal conductivity of many sedimentary and metamorphic rocks is strongly anisotropic (Clausen and Huenges 1995). Since black smoker chimneys are chemical sediments formed by precipitation of dissolved minerals, they are believed to be anisotropic as well which complicates the estimation of the thermal conductivity and thus modelling. The anisotrophy of the chimney wall is not taken into account in our model.
As stated previously, thermal conductivity is a function of the ambient temperature, which makes it complicated since the temperature at a specific position x is dependent on the thermal conductivity.
For sedimentary rocks, up to 300ºC there is a reduction of λ by nearly a factor of 2. Above temperatures of 300 ºC, there still is a decrease of thermal conductivity but it comes nearly to an end (Clausen and Huenges 1995).
The most data on λ is available for standard conditions (Clausen and Huenges 1995). In this research, data is needed for temperatures up to 350 ºC and pressures of 250 bars. Empirical relationships which define the dependence of the thermal conductivity on temperature are available but there is no real substitute for individual measurements.
An empirical relationship, found by Sass et al. (1992), states that for rocks

$$\lambda(T) = \frac{\lambda(0)}{1.007 + T(0.0036 \times \frac{0.0072}{\lambda(0)})} \tag{7}$$

$$\lambda(0) = \lambda(25) \times [1.007 + 25 \times (0.0037 - \frac{0.0074}{\lambda(25)})] \tag{8}$$

Where λ is the thermal conductivity in W $m^{-1}K^{-1}$ as a function of temperature, T the temperature in ºC, λ(0) is the thermal conductivity at 0 ºC and λ(25) the temperature at 25 ºC (Sass, Lachenbruch et al. 1992). In this research, the equations from Sass et al. (1992) were used to

correct for the temperature component on the thermal conductivity for the solid phase. There is some slight offset between the standard thermal conductivity at 25°C which is used as λ(25) and the thermal conductivity, λ(T) calculated at 25°C but the difference between these two values is too small and can be ignored.

The thermal conductivity of a liquid-saturated rock is dependent on the thermal conductivities of the dry rock and the saturating liquid as well as the physical properties of the rock. Liquid saturated rocks have higher conductivities than dry rocks, the amount of increase being a complex function of the amount of pore space, its nature and distribution, and the conductivity of the saturating fluid (Somerton 1992). The modelled hydrothermal vent system can be compared to a liquid-saturated rock in which the liquid is water. Water has the highest thermal conductivity of any fluid which might occupy the pore spaces in reservoir rocks, thus water saturation will have a disproportionally large effect on the conductivity of the fluid saturated rock (Somerton 1992).
When porosities exceed 1%, the thermal conductivity of the pore fluid significantly affects the bulk thermal conductivity of the saturated rock (Clausen and Huenges 1995). Since porosities of black smoker chimneys are at least 10%, the thermal conductivity of the pore fluid should be taken into account in calculations. The effect of the porosity varies whether the rock is porous or fractured. Porosity in porous rocks consists of “bottlenecks” formed at the contact between individual grains and the bulk pore space. The thermal conductivity increases with an increasing saturation of the pore space (Clausen and Huenges 1995). Assumed is that all the pore space in hydrothermal vent chimney’s is filled with pore fluid, so the degree of saturation of the pore space is 100% and no “bottlenecks” are present.
The International Association for the Properties of Steam has extensive tables on the variation of the thermal conductivity with temperature and pressure that can be used for scientific purposes (Sengers and Watson 1986). When the pressure is set to 250 bar (i.e. 25 MPa), the change in thermal conductivity with temperatures varying between 0°C and 350°C can be calculated with the polynomial following polynomial formula:

$$\lambda_f = 3\cdot10^{-14}T^5 - 2\cdot10^{-11}T^4 + 2\cdot10^{-8}T^3 - 1\cdot10^{-5}T^2 + 0.0021T + 0.574 \quad (9)$$

where λ_f is the thermal conductivity of the fluid phase in W m^{-1} K^{-1} and T the temperature in °C. The above described formula is implemented in the model to calculate the thermal conductivity of the fluid phase.

For a two-phase medium where the solid phase is continuous, the ratio of thermal conductivities (λ_2/λ_1) is smaller than 10, and the volume proportion of the fluid is less than 0.25, the average conductivity is

$$\lambda_r = \lambda_2 \times \frac{\left[1 - 2p(1-\frac{\lambda_1}{\lambda_2})/(2+\frac{\lambda_1}{\lambda_2})\right]}{\left[1 + p(1-\frac{\lambda_1}{\lambda_2})/(2+\frac{\lambda_1}{\lambda_2})\right]} \quad (10)$$

Where λ_r is the average thermal conductivity, λ_2 the conductivity of the second phase (e.g. anhydrite layer), p is the volume of phase 1 (e.g. fluid phase).
For three phase media (e.g. 2 solid phases and pore fluid), the equation following is used (Brailsford and Major 1964):

$$\lambda_r = \lambda_0 \times \frac{\left[p_0 + \frac{3\lambda_1 p_1}{2\lambda_0 + \lambda_1} + \frac{3\lambda_2 p_2}{2\lambda_0 + \lambda_2} \right]}{\left[p_0 + \frac{3\lambda_0 p_1}{2\lambda_0 + \lambda_1} + \frac{3\lambda_0 p_2}{2\lambda_0 + \lambda_2} \right]} \quad (11)$$

3.3.2 Transport of mass

Diffusion is the process by which matter is transported from one point of a system to another as a result of random molecular motions (Crank 1975). Diffusion acts to eliminate gradients of concentration (or chemical potential) by moving materials down the gradient (Boudreau 1997).
Transport of mass by only diffusion can be described by another PDE, which is similar to the one used for temperature

$$\frac{\partial C_i}{\partial t} = \frac{\partial}{\partial x}(D_i \frac{\partial C_i}{\partial x}) + \frac{\partial}{\partial x}(D_i C_i \frac{\partial \ln \gamma_i}{\partial x}) \quad (12)$$

Where D_i is the diffusion coefficient which is species dependent, C_i is the concentration of species i, γ_i is the activity coefficient which account for the non-ideal effects of the solution. The diffusion coefficient is defined as the rate of transfer of the diffusing substance across unit area of a section, divided by the space gradient of concentration at the section (Crank 1975).
Inclusion of the $\frac{\partial \ln \gamma_i}{\partial x}$ term is necessary since γ_i changes significantly with changing ionic strength and temperature. This is in contrast to most aqueous diffusion studies where temperature and ionic strength are relatively constant (Tivey and McDuff 1990).
Since diffusion is not the only process affecting species distribution, advection is also modeled. Tivey and McDuff (1990) used a modified Bernoulli equation to calculate the pressure difference within a vent chimney. With the use of Darcy's law, assuming a permeability of 10^{-14} m^2, they calculated advection rates of $\pm 3\times10^{-7}$ m s^{-1} for a 3 cm thick wall (TIVEY AND MCDUFF, 1990). This value for the advection rate is used in model calculations. The advection is assumed to be inward from the hydrothermal vent side; advection inward from the seawater side is neglected.

3.3.3 Calculation of the diffusion coefficient

A one-dimensional flux resulting from molecular/ionic diffusion in a porous medium can be described by Fick's first law

$$(F_D)_i = -D_i^0 \frac{dC_i}{dx} \quad (13)$$

The negative indicates the flux in a direction opposite to the gradient. D_i^0 is the value of the diffusion coefficient in a free solution, the so-called tracer diffusion coefficient. D_i and D_i^0 are different because of the path followed by solutes during diffusion in non-free solutions. The relation between D_i and D_i^0 depends on the composition and speciation of the solution (Oelkers and Helgeson 1988).

Equations based on empirical relationships have been developed for the calculation of tracer diffusion coefficients. They have been developed for electrolyte and non-electrolyte species. These empirical equations include the temperature dependency, dynamic viscosity and molar volume.

Uncharged (non-electrolyte) species are usually treated as spheres moving in a water continuum which leads to the Stokes-Einstein equation, which is a theoretical expression that describes the situation when the particles are much larger that the water molecules (i.e. friction goes towards ∞) (Boudreau 1997)

$$D_i^0 = \frac{kT}{6\pi\mu^0 r_0} = \frac{RT}{6\pi\mu^0 N r_0} \tag{14}$$

Where k is Boltzmann's constant, μ^0 is the dynamic viscosity of water, r_0 is the radius of the particle, T is the temperature in K, R the gas constant and N is Avagadro's constant.
The Stokes-Einstein equation is used to describe the tracer diffusion coefficients in previous models for hydrothermal vent systems (Tivey and McDuff 1990) but theoretical expressions are really approximations as they idealize both the fluid and the diffusing molecules/particles. Accuracies are limited to 20-30%. Therefore empirical relationships have been developed to calculate the tracer diffusion coefficient. One of the most widely used is (Wilke and Chang 1955; Hayduk and Laudie 1974):

$$D_i^0 = 4.72 \cdot 10^{-9} \frac{T}{\mu^0 V_b^{0.6}} \qquad (\mathrm{cm^2\ s^{-1}}) \tag{15}$$

where μ^0 is the dynamic viscosity of water in units of poise, T is the absolute temperature, and V_b is the molar volume of the non-electrolyte (at the normal boiling temperature of that solute). Values of V_b are found appendix 2.

For charged species (ions and electrolytes) the estimation of the tracer diffusion coefficient is more complicated. The most common way of calculation the tracer diffusion coefficient of an ion is by using the so-called Nernst-Einstein equation, which is given by

$$D_i^0 = \frac{RT\lambda_i^0}{|z_i|F^2} = \frac{k_b T\lambda_i^0}{|z_i|N_A e_0^2} \tag{16}$$

Where D_i^0 and λ_i^0 stand for the tracer diffusion coefficient in cm^2 sec^{-1} and the limiting equivalent conductance of the *i*th aqueous species in cm^2 Ω^{-1} $equivalent^{-1}$, respectively, R represents the gas constant, T refers to the temperature in K, z_i denotes the charge of the *i*th species, and F designates Faraday's constant, k_b is Boltzmann's constant, N_A is Avagadro's number and e_0 is the charge on an electron (Oelkers and Helgeson 1988).
The limiting equivalent conductance is calculated by the use of Stokes' law, which is given by

$$\lambda_i^0 = 10^7 \frac{F|z_i|e_0}{6\pi\mu^0 r_{s,i}} \tag{17}$$

Where μ stands for viscosity of the solution (poises), e_0 denotes electronic charge ($1.602*10^{-19}$ Coulomb) and $r_{s,i}$ refers to the Stokes' law radius of the *i*th ion in cm.

Stokes' law radii give an estimate of the effective radius of an ion as it moves through solution. Faster moving ions have smaller Stokes' law radii while slower moving ions have larger Stokes' law radii (Marcus 1994; Rieger 1994). The radii used in this research can be found in appendix 2.

When the viscosity of a solution is constant, the equation for the limiting equivalent conductance represents a proportionality between the limiting equivalent conductance and the reciprocal of the Stokes' law radius for aqueous ions with a given charge (Oelkers and Helgeson 1988). However, the viscosity of a solution is dependent on temperature, pressure and fluid composition. The change in dynamic viscosity (in poises) of pure water (μ^0) with increase in temperature can be calculated by the empirical formula found by the Dortmund Data Bank (DBB) (see figure 2):

$$\mu^0 = A \times 10^{\frac{B}{T-C}} \tag{18}$$

Where A=2.414 x 10^{-4} Poises; B=247.8K and C=140 K.

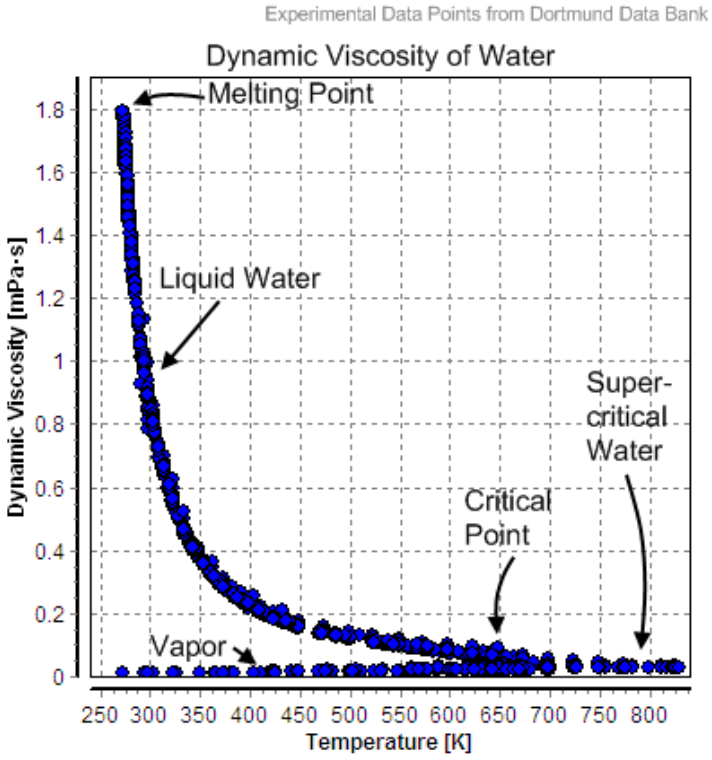

Figure 2: *The dynamic viscosity as a function of temperature for pure H_2O. The data points are found in the Dortmund Data Bank.*

The values and formula found by the Dortmund Data Bank correspond to data found by other researchers (Robinson and Stokes 1965; Yusufova, Pepinov et al. 1978) and is used to calculate the dynamic viscosity of water in the model.

Besides temperature, the diffusion coefficient is dependent on pressure and fluid composition. Assumed is that the pore fluid can be represented as 3.2 wt% NaCl-H_2O solution (Tivey and McDuff 1990). The limiting diffusion coefficients for all components were corrected for the viscosity of the salt solution (Li and Gregory 1974)

$$D_i^* = D_i^0 \frac{\mu^0}{\mu} \tag{19}$$

The temperature and pressure dependence on μ and D_i of a solution are closely related. Since the pressure effects on the dynamic viscosity are small, one can assume the same for D_i. Therefore, there is no correction made for the pressure effect on the diffusion coefficient (Li and Gregory 1974).

It has long been recognized that diffusion in a sediment-water mixture is slower than in an equivalent volume of water because of the convoluted path the ions and molecules must follow to circumvent solid particles. This changes the value of the tracer diffusion coefficient (Li and Gregory 1974):

$$D_i = D_i^0 \frac{\alpha}{\theta^2} \tag{20}$$

where θ is the tortuosity (dimensionless) and α is the ratio of the viscosity of the bulk fluid to the of the interstitial solution and is taken to be 1.
Tortuosity is defined as the ratio of the (average) incremental distance, dL, which an ion/molecule must travel to cover a direct distance, dx, in the direction of diffusion, i.e. dL/dx. The tortuosity factor is defined as $(dL/dx)^2$ or θ^2 and can be estimated from porosity using the relation (McDuff and Gieskes 1976)

$$\theta^2 = \phi F \tag{21}$$

where F is the formation factor, which is the ratio of the electrical resistivity of the porous medium to that of the pore fluid. The formation factor is empirically related to the porosity by (Tivey and McDuff 1990)

$$F = \phi^{-n} \tag{22}$$

A value of n=2 is taken to be appropriate for sandstone and used in this model (Tivey and McDuff 1990)

3.3.4 Calculation of the activity coefficient

Diffusion in response to thermal or electrical potential gradients or the effects of ion pairing are negligible when the effect of the activity coefficient is taken into account. In most studies of aqueous diffusion, temperature and solution concentration are fairly constant and therefore concentration equals activity (Tivey and McDuff 1990).
In this transport-reaction model, diffusion in response to activity coefficients is considered.
In a concentrated multi-component electrolyte solution consisting predominantly of sodium chloride, ions and electrolytes present in small concentrations (compared to that of the sodium chloride) should contribute negligibly to the ionic strength and total coordination of water molecules in the solution. In such an ion or electrolyte, close approximations of individual activity coefficients for the species present in small concentrations can be calculated from a Debye-Huckel algorithm (Helgeson 1969)

$$\log \gamma_i^*(T,\bar{I}) = -\frac{A_\gamma z_i^2 \sqrt{\bar{I}}}{1+\alpha_\gamma B_\gamma \sqrt{\bar{I}}} + B_\gamma^* \bar{I} \tag{23}$$

where z_i refers to the charge ion, γ_i^* is the activity coefficient of the *i*th ion present in small concentrations in the solution, $\bar{I}$ and B_γ^* are the true ionic strength an deviation function, respectively, for pure solutions of the supporting electrolyte. A_γ and B_γ refer to the molal Debye-Huckel coefficients and refers to the "distance of closest approach" of the ions in solution. A_γ, B_γ, $\bar{I}$ and α_γ are all functions of temperature. The Debye-Huckel coefficients can be described by (Helgeson 1969):

$$A_\gamma(T) = \frac{1.8246\times10^6 \sqrt{\rho_{H_2O}(T)}}{(\varepsilon_{H_2O}(T)T)^{3/2}} \tag{24}$$

$$B_\gamma(T) = \frac{50.29\times10^8 \sqrt{\rho_{H_2O}(T)}}{\sqrt{\varepsilon_{H_2O}(T)T}} \tag{25}$$

Where ρ_{H_2O} refers to the density of water and ε_{H_2O} to the dielectric constant of water, which are both temperature dependent, T refers to the absolute temperature. Values of A_γ and B_γ used in this model were calculated by Helgeson (1969) and can be found in table 4. A trendline trough these values gives us the polynomial formula that has been implemented in the model, with temperature being the only variable and r^2=1 for both cases:

$$A_\gamma(T) = 4\cdot10^{-8}T^3 - 4\cdot10^{-5}T^2 + 0.0163T - 1.6396 \tag{26}$$

$$B_\gamma(T) = -2\cdot10^{-24}T^6 + 6\cdot10^{-21}T^5 - 6\cdot10^{-18}T^4 + 4\cdot10^{-15}T^3 - 10^{-12}T^2 + 2\cdot10^{-10}T - 10^{-8} \tag{27}$$

where T is the temperature in Kelvin.

The ionic strength of the solution can be calculated by

$$\bar{I} = \tfrac{1}{2}\sum_i z_i^2 m_i = (1-\alpha_{NaCl})I \tag{28}$$

where z_i is the charge on the *i*th ion, m_i is the concentration of the *i*th species in mol/kg, α_{NaCl} defines the degree of association of the solute and *I* is the ionic strength of the solution which is 0.57 in the case of a 3.2wt% NaCl-H_2O solution.
Helgeson (1969) found values for the degree of association for 1.0, 2.0, 3.0 molal solution of NaCl. Extrapolation of these values towards a 0.57 molal NaCl solution gave us the α_{NaCl} values needed in this model (see table 4). The degree of association is 0 up to a temperature of 100°C which means that $\bar{I}$ equals *I*, which is 0,57 mol/kg. Above 100°C the degree of association can be described by:

$$\alpha_{NaCl} = 1\cdot10^{-5}e^{0,0178T} \tag{29}$$

The deviation function B_γ^* is described by a different Debye-Huckel algorithm and describes the departure of the log of the ionic activity coefficient from that predicted by the (standard) Debye-

Huckel equation at 25°C. It is the difference between the observed and predicted activity coefficient. The deviation function at a given temperature can be defined by (Helgeson 1969)

$$B_{\gamma}^{*}(\bar{I}) = \frac{\log \gamma_{\pm}^{*} + A_{\gamma}|z_1 z_2|\sqrt{\bar{I}}\,/(1+\alpha_{\gamma} B_{\gamma}\sqrt{\bar{I}})}{\bar{I}} \tag{30}$$

Where A_γ and B_γ are the Debye-Huckel coefficients, $\bar{I}$ is the true ionic conductivity, z_1 and z_2 are the electrical charge of the ions in the electrolyte, α_γ is the "distance of closest approach" and log $\gamma_{\pm}^{*}$ is the mean ionic activity coefficient of a strong electrolyte which can be described by the Stokes-Robinson equation (Helgeson 1969)

$$\log \gamma_{\pm}^{*}(T,\bar{I}) = -\frac{A_{\gamma}|z_1 z_2|\sqrt{\bar{I}}}{1+\dot{a}B_{\gamma}\sqrt{I}} - \frac{h}{v} - \log a_w - \log[1-0.018m(v-h)] \tag{31}$$

In which a_w is the activity of H_2O, m is the molality of the completely dissociated solute (which is equivalent to I in the case of NaCl), α_γ is the "distance of closest approach" of the ions in solution, v is the number of ions per mole of solute, and h is the average number of water molecules coordinated to v ions in solution. The Stokes-Robinson equation provides for the effect of ion hydration on the activity coefficient on the solute (Helgeson 1969).

Values for the deviation function B_γ^* were taken from Helgeson (1968) (see table 2). Values of the deviation function pass through a maximum with increasing temperature and are only slightly dependent on concentration at molalities of NaCl between one and three. The uncertainty in the data from which the B_γ^* values were calculated exceed the extent of this variation; therefore the effect of concentration can be ignored for hydrothermal solutions with molalities between 1 and 3 (Helgeson 1969). Assumed is that this is also the case in a 3.2 wt% NaCl-H_2O solution which has a molarility of ~0.57.

A trendline was put through the values of the deviation function found by Helgeson (1968) and gave a polynomial formula (r^2=0,9781) which was used in the model

$$B_{\gamma}^{*} = -7\cdot 10^{-9}T^{3} + 8\cdot 10^{-6}T^{2} - 0.0028T + 0.3647 \tag{32}$$

With the extrapolation of data from Helgeson (1968, 1969) values of A_γ, B_γ, $\bar{I}$ and B_γ^* can be calculated, the only unknown remains the "distance of closest approach" (α_γ). Unfortunately, values for α_γ for most ions at high temperatures are not available, nor can they be calculated with confidence. The best approximation that can be made in the present state of knowledge is to assume that α_γ-coefficients for ions are independent of temperature and employ the values at 25°C in the calculations of high temperature activity coefficients. For NaCl, the α_γ values from 25°C to 300°C vary between -0.7 and 0.5 angstroms from its value at 25°C. If the α_γ values for other salts (and ions) behave in a similar fashion, the error involved in calculating high temperature activity coefficients by assuming α_γ values at 25°C to be constant should be negligible compared to other uncertainties attending geochemical calculations. Because α_γ values tend to increase with increasing temperature, high temperature activity coefficients for individual ions calculated assuming constant α_γ values equal to their values at 25°C should be minimal approximations (Helgeson 1969).

The parameter α_γ depends on the nature of the electrolyte and its concentration. It also depends on the nature and concentration of the species present in the solution which participate in the formation of an ionic atmosphere. There is no direct method for the measurement of this

parameter (Ribeiro, Esterso et al. 2006), therefore, values were taken from calculations of Kielland (1937) and can be found in appendix 2.

Nonelectrolyte species are treated as dissolved gases, i.e. these species are not allowed to dissociate throughout the transport process. Diffusive transport of these nonelectrolyte species is driven only by gradients of concentration since activity coefficients are constant with temperature (Tivey and McDuff 1990)
This would mean that the activity coefficient of nonelectrolyte species is independent from the concentration of other species in the solution. However, in subcritical aqueous solutions when neutral species are significant there appears to be considerable non-ideal interactions between neutral species and charged species (Walther 1997). There are equations that include neutral-cation, neutral-anion and neutral-neutral interactions into the calculation of the activity coefficient for neutral species, where the activity coefficient of the neutral species is independent of the ionic strength (Pitzer 1991) but values for the parameters used in the so-called Pitzer equations are not available for temperature and pressure conditions found in hydrothermal vents. Also, the activity coefficient approaches unity once the molality of the nonelectrolyte species approaches zero (Sedlbauer and Majer 2000). The activity coefficient of the neutral species in this model are believed to approach unity.
With the formula's described above it is possible to calculate D_i and γ_i, which allows us to solve the PDE for mass transport. After this PDE is solved by the sequential noniterative approach (SNIA) (Aguilera D.R., Jourabchi P. et al. 2005), the reaction step is considered.

	25°C	**50°C**	**100°C**	**150°C**	**200°C**	**250°C**	**270°C**	**300°C**
B_γ **[a]**	0.041	0.043	0.046	0.047	0.047	0.034	0.015	0.0
A_γ **[b]**	0.5095	0.5354	0.6019	0.6915	0.8127	0.9907	1.0905	1.2979
B_γ $(\cdot 10^{-8})$ **[b]**	0.3284	0.3329	0.3425	0.3536	0.3659	0.3807	0.3879	0.4010
α_{NaCl} **[c]**	0,57	0,57	0,57	0,019135	0,05109	0,118505	0,1654	0,28095

Table 2: ***a.*** *Values computed (Helgeson 1969) using equation 39 from the mean ionic activity coefficients and those calculated from the Debye-Huckel equation.* ***b.****Computed (Helgeson, 1967) from equations 33 and 34 using density and dielectric constant data for water taken, respectively, from Keenan and Keyes (1936) and Akerlof and Oshry (1950).* ***c.*** *Values for α_{NaCl} are for a 0,57 mol/kg NaCl solution (3.2wt% NaCl-H_2O solution) and extrapolated from values found in Helgeson (1969)*

3.3.5 Mass balance equations

To make sure that the mass balance equation is correct, the flux at the hydrothermal vent side should equal the flux at the seawater side for species not involved in an equilibrium reaction (F_{in}-F_{out}=0). To calculate the fluxes at the boundaries a second accurate finite difference method is used.

$$F_{hv} = \frac{-3C_0 + 4C_1 - C_2}{2\Delta x} \tag{33}$$

$$F_{sw} = \frac{-3C_N + 4C_{N-1} - C_{N-2}}{2\Delta x} \tag{34}$$

Where F_{hv} and F_{sw} represent the flux at the hydrothermal vent side and the seawater side, respectively, C_0 is the concentration of a species at the first space step and C_N is the concentration of a species at the last timestep.

The models in this research all have a Dirichlet type boundary condition for each species on both sides of the hydrothermal vent. Conservation of mass at the boundary of a dissolved species in a 1-D system can be described by

$$[\varphi \cdot (uC_i - D_i^{'} \frac{\partial C_i}{\partial x}]_d \cdot n = \mathrm{Y} \tag{35}$$

Where $x=d$ is the arbitrary depth of the boundary condition, n is the outward unit vector along the surface. In a 1-D system, n equals +1 if n points towards the positive x-direction, in our case towards the seawater side, and n is -1 if it points in the negative x-direction, in our case towards the hydrothermal vent side. Y is the net amount of material supplies/removed from any reactions or "prescribed fluxes" at this boundary. This equation applies only to the depth $x=d$ and has no meaning anywhere else; it states that an input flux is balanced by the combined effects of diffusion and advection. Since there are no "applied fluxes" and only diffusion is assumed in the first place, the mass conservation equation at the boundaries becomes

$$[-\varphi \cdot D_i^{'} \frac{\partial C_i}{\partial x}]_{hv} = F_{hv} \tag{36}$$

$$[\varphi \cdot D_i^{'} \frac{\partial C_i}{\partial x}]_{hv} = F_{sw} \tag{37}$$

$$F_{hv} - F_{sw} = \sum_i \int_{hv}^{sw} R dx \tag{38}$$

$$\left[-\varphi \cdot D_i^{'} \frac{\partial C_i}{\partial x} \right]_{hv} - \left[\varphi \cdot D_i^{'} \frac{\partial C}{\partial x} \right]_{sw} = \sum_i \int_{hv}^{sw} R dx \tag{39}$$

Where

$$\sum_i R = \frac{d[C_i]_R}{dt} \tag{40}$$

3.4 Chemical reactions

Chemolithoautotrophic microbes gain their energy from out of equilibrium redox reactions, therefore, several redox reactions which have been linked to chemolithoautotrophic microbial metabolisms are considered in this model.
Besides redox reactions, acid-base reactions are taken into account because they alter the chemistry of the pore fluid, which will affect the extent of the redox reactions and thus the microbial metabolism. The reactions included are listed below.

3.4.1 The sulfur system

The oxidation of sulfide (H_2S, HS^-) and elemental sulfur (S^0) are widely accepted as the principal chemosynthetic reactions leading to production of primary biomass (Karl, Wirsen et al. 1980). For the sake of simplicity only hydrogen sulfide species (H_2S and HS^-) are considered as electron donors, since these are present in relatively high concentrations in hydrothermal systems. Sulfide oxidizing microorganisms gain metabolic energy by converting H_2S and HS^- to sulfate through the reactions

$$H_2S(aq) + 2O_2(aq) \rightarrow SO_4^{2-} + 2H^+ \quad (41)$$

$$HS^-(aq) + 2O_2(aq) \rightarrow SO_4^{2-} + H^+ \quad (42)$$

Conversely, sulfate reducing microorganisms convert sulfate to sulfide according to the reaction

$$SO_4^{2-}(aq) + 4H_2(aq) + 2H^+(aq) \rightarrow H_2S(aq) + 4H_2O \quad (43)$$

Also taken into account in the model is the sulfide dissociation reaction which is believed to be in equilibrium

$$H_2S(aq) \rightarrow HS^-(aq) + H^+(aq) \quad (44)$$

Since H_2S immediately reacts to HS^- by the equilibrium dissociation reaction described above when the pH is sufficient it is not necessary to include a reaction where sulfate is reduced to HS^-.

3.4.2 The carbon system

The reactions considered in the carbonate system are acid-base reactions which proceed spontaneously. They are believed to be in equilibrium with the hydrothermal system.

$$H_2CO_3 \leftrightarrow HCO_3^- + H^+ \quad (45)$$

$$HCO_3^- \leftrightarrow CO_3^{2-} + H^+ \quad (46)$$

Besides the carbon dissociation reactions, methanotrophy (methane oxidation) and methanogenesis (CO_2 and HCO_3^- reduction) are taken into account.

$$CH_4 + 2O_2 \rightarrow CO_2 + 2H_2O \quad (47)$$

$$CO_2 + 4H_2 \rightarrow CH_4 + 2H_2O \quad (48)$$

$$HCO_3^- + 4H_2 + H^+ \rightarrow CH_4 + 3H_2O \quad (49)$$

3.4.3 Other reactions considered

The Anoxic oxidation of Methane (AOM) is a very likely candidate for chemolithoautotrophy in hydrothermal vent systems. AOM is a collaboration between the carbon system and the sulfur

system where methane is oxidized by sulfate. This means that it is part of the carbon system as well as the sulfur system.

$$CH_4 + 4SO_4^{2-} \rightarrow HCO_3^- + HS^- \tag{50}$$

Also implemented in the model is the so-called Knallgas reaction, which is believed to take place inside a hydrothermal vent chimney.

$$H_2 + 0.5O_2 \rightarrow H_2O \tag{51}$$

Another important acid-base reaction considered in the model is the water dissociation reaction

$$H_2O \leftrightarrow H^+ + OH^- \tag{52}$$

The acid-base reactions are all believed to be in equilibrium. The redox reaction kinetics are modelled to be bimolecular but include a thermodynamic factor, which will be described below in this section. The complete set of reactions and their reaction kinetics used for that reaction are described in appendix 1.

For each individual species the change in time due to (kinetic) reactions can be described by the specific reactions involving this species and the stochiometry of this species in the specific reactions, as long as the reaction rate is bimolecular. These rate reactions give the production and/or consumption of this species:

$$\frac{d[CH_4]_R}{dt} = k_{mg} \cdot [CO_2(aq)] \cdot [H_2] - k_{mt} \cdot [CH_4] \cdot [O_2] - k_{aom} \cdot [CH_4] \cdot [SO_4^{2-}] \tag{53}$$

$$\frac{d[CO_2]_R}{dt} = k_{mt} \cdot [CH_4] \cdot [O_2] - k_{mg} \cdot [CO_2] \cdot [H_2] \tag{54}$$

$$\frac{d[HCO_3^-]_R}{dt} = -k_{mt2} \cdot [HCO_3^-] \cdot [H_2] + k_{aom} \cdot [CH_4] \cdot [SO_4^{2-}] \tag{55}$$

$$\frac{d[DIC]_R}{dt} = k_{mt} \cdot [CH_4] \cdot [O_2] - k_{mg} \cdot [CO_2] \cdot [H_2] - k_{mt2} \cdot [HCO_3^-] \cdot [H_2] + k_{aom} \cdot [CH_4] \cdot [SO_4^{2-}] \tag{56}$$

$$\frac{d[H_2S]_R}{dt} = k_{sr} \cdot [SO_4^{2-}] \cdot [H_2] - k_{so1} \cdot [H_2S] \cdot [O_2] + k_{aom} \cdot [CH_4] \cdot [SO_4^{2-}] \tag{57}$$

$$\frac{d[HS^-]_R}{dt} = -k_{so2} \cdot [HS^-] \cdot [O_2] + k_{aom} \cdot [CH_4] \cdot [SO_4^{2-}] \tag{58}$$

$$\frac{d[TRS]_R}{dt} = k_{sr} \cdot [SO_4^{2-}] \cdot [H_2] - k_{so1} \cdot [H_2S] \cdot [O_2] - k_{so2} \cdot [HS^-] \cdot [O_2] + k_{aom} \cdot [CH_4] \cdot [SO_4^{2-}] \tag{59}$$

$$\frac{d[SO_4^{2-}]_R}{dt} = k_{so1} \cdot [H_2S] \cdot [O_2] + k_{so2} \cdot [HS^-] \cdot [O_2] - k_{sr} \cdot [SO_4^{2-}] \cdot [H_2] - k_{aom} \cdot [CH_4] \cdot [SO_4^{2-}] \quad (60)$$

$$\frac{d[H_2]_R}{dt} = -k_{kn} \cdot [H_2] \cdot [O_2] - 4k_{mg} \cdot [CO_2] \cdot [H_2] - 4k_{mg2} \cdot [HCO_3^-] \cdot [H_2] - 4k_{sr} \cdot [SO_4^{2-}] \cdot [H_2] \quad (61)$$

$$\frac{d[O_2]_R}{dt} = -\frac{1}{2} k_{kn} \cdot [O_2] \cdot [H_2] - 2k_{mt} \cdot [CH_4] \cdot [O_2] - 2k_{so1} \cdot [H_2S] \cdot [O_2] - 2k_{so2} \cdot [HS^-] \cdot [O_2] \quad (62)$$

3.4.4 Mineral formation

Besides the interaction between microbes and hydrothermal vent fluid, there is also interaction between microbes and the minerals/rocks of which the vent is composed and interaction between the pore fluid and the minerals. For a more complete picture of a hydrothermal vent chimney, mineral precipitation and dissolution should be taken into account.
The formation of a black smoker chimney can be separated into different stages. The first stage of growth of a hydrothermal vent is due to the mixing of seawater and hydrothermal fluid and results in the precipitation of a porous layer of anhydrite. This anhydrite wall partially isolates the hydrothermal solution from the seawater, resulting in so-called stage I growth which includes precipitation of minerals within the pore spaces of the wall, replacement of earlier formed minerals and deposition of an inner channel lining of Cu-Fe sulfides (Schrenk, Holden et al. 2008). Mineral precipitation and dissolution reactions are not implemented directly in this model, but with the outcome of the model, the Saturation Indices (SI) of the different minerals can be calculated.

$$SI = \log \frac{IAP}{K} \quad (63)$$

where IAP denotes the activity production of the mineral and K denotes the mineral equilibrium constant, which is dependent on temperature and pressure. The saturation index of a mineral predicts whether of not this mineral will precipitate. If SI>0 , the mineral will precipitate. If SI<0, the mineral will not precipitate. The saturation index only assumes thermodynamics and will therefore gain no insight into the kinetics of precipitation or dissolution reactions.
The saturation indices for the minerals anhydrite ($CaSO_4$), barite ($BaSO_4$), chalcopyrite ($CuFeS_2$), covellite (CuS), galena (PbS), pyrite (FeS_2), pyrrhotite, sphalerite (ZnS) and wurzite (ZnS) are considered in the model. These are minerals that can be formed by the metals and sulfides present in the pore fluid due to mixing of hydrothermal vent fluid and seawater and have been found to be present in hydrothermal vent chimneys (Tivey 1995).

Because the precipitation reactions are not modeled directly but results are used to predict whether or not a mineral will precipitate, the species Ba^{2+}, Ca^{2+}, Fe^{2+}, Cu^{+}, Pb^{2+} and Zn^{2+} are only subjected to diffusion and advection as described in chapter 2.3. A complete overview of the mineral formation reactions and the calculation of the corresponding IAP can be found in appendix 1.
Due to the large temperature gradient, mineral equilibrium constants are temperature dependent. The change in the equilibrium constants affects the saturation index of a mineral, which determines if a mineral will precipitate or not. The effect of temperature (and pressure) on the

equilibrium constants for the different mineral formation reactions was calculated by the use of the OrganoBioGeoTherm (OBIGT) software which uses the SUPCRT92 database. OBIGT has been developed by John J. Donovan and provides a graphical front-end to SUPCRT92, enabling the user to calculate the standard molal thermodynamic properties of aqueous, solid, and gaseous species and reactions between them as a function of temperature and pressure. For more information, see www.predcent.org/download/OrganoBioGeoTherm.
The dependency of the equilibrium constants as a function of temperature, assuming a constant pressure of 250 bars, was then used to calculate the saturation indices of the minerals.

3.4.5 Thermodynamics of microbial reactions

There is a close relationship between geochemical conditions and the microbial community; the microbes promote reactions that change geochemical conditions and the geochemistry controls the nature of the microbial community. Redox reactions in a geochemical environment are promoted by the enzymes in the ambient microbial community. Microbes use their collective of enzymes to catalyze redox reactions, harvesting some of the energy released for their own purpose (Bethke 2008). Therefore, the rate laws applied to enzyme kinetics can also be applied to redox reactions that are catalyzed by microbes.

An enzymatic reaction can be represented in a general form by

$$\sum_S v_S S \leftrightarrow \sum_P v_P P \tag{64}$$

S represents the reactant or substrate, P represents the product. The stochiometric coefficients of the substrate and product are represented by v_S and v_P, respectively (Jin and Bethke 2007). Redox reactions that supply energy to microbes can be represented by

$$\sum_D v_D D + \sum_A v_A A \leftrightarrow \sum_{D^+} v_{D^+} D^+ + \sum_{A^-} v_{A^-} A^- \tag{65}$$

Where D and D^+ represent the species on the reduced and oxidized sides of primary electron-donating half-reaction, A and A^- are the species on the oxidized and reduced sides of the terminal-accepting half-reaction, and v_D, etc., are the half-reaction coefficients (Jin and Bethke 2002). The microbes catalyze redox reactions, harvesting some of the energy released and storing it as adenosine triphosphate (ATP). This is an unstable molecule and hence rich in energy.

$$ADP + PO_4^{3-} \rightarrow ATP + H_2O \tag{66}$$

In this model, bimolecular rate laws are used in which the rate is dependent on the concentrations of the reactants and the second-order rate constant (k_i). The reactions considered in the model and their corresponding bimolecular rate laws are described in appendix 1.
The rate equations used are limited in a way that they do not consider all of the chemical species consumed and liberated by the electron donating and accepting half-reactions. They account only for the forward reaction even though any enzyme catalyzes a reaction in both the forward and reverse direction simultaneously, albeit not necessary at equal rates. Common rate equations also do not account for the thermodynamic requirement that a microbe conserves energy from its environment (Jin and Bethke 2005).

A rate law that is kinetic- as well thermodynamically consistent should account for the concentration of each chemical species involved in the microbial respiration and the availability of energy in the geochemical environment. Jin and Bethke (2002, 2005) and Bethke (2008) developed such a rate law by implementing a so-called thermodynamic factor. This means that our bimolecular rate law becomes:

$$R = k_i [D][A] F_T \tag{67}$$

Where F_T is the thermodynamic potential factor, k represents the rate constant and [D] and [A] give the activities of the electron donor and electron acceptor, respectively.
The thermodynamic potential factor accounts for the effect of the thermodynamic driving force. Therefore, the thermodynamic potential factor has a value between 0 (no reaction) and 1 (no thermodynamic inhibition).
The thermodynamic factor can be described by:

$$F_T = 1 - \exp\left(\frac{\Delta G_r + m\Delta G_P}{\chi RT}\right) \tag{68}$$

Where ΔG_r is the free energy change (J mol^{-1}) of the redox reaction, ΔG_P is the free energy change (J mol^{-1}) under cellular conditions of the ATP reaction, m is the number of ATPs produced per reaction turnover, χ is the average stochiometric number of the overall reaction. R is the gas constant and T is the absolute temperature (K). Values of χ and m are proportional to the number of electrons transferred in the overall reaction. The average stochiometric number is the number of times the rate controlling step in the overall reaction occurs per turnover of the overall reaction.
When the energy available is large compared to the energy conserved ($m\Delta G_P$), the thermodynamic driving force approaches one and the rate law is equal to a regular bimolecular rate law. When the energy available is not so large when compared to the energy conserved, the thermodynamic driving force is smaller and F_T becomes smaller than one. When $m\Delta G_P$ becomes larger than ΔG_r, the value of F_T becomes negative, implying that respiration will proceed backwards (Jin and Bethke 2007). In nature, to prevent loss of ATP, a microorganisms will regulate its respiratory chain to prevent reverse electron transfer (Jin and Bethke 2002), which means that $F_T \geq 0$.
The free energy change, ΔG_r, of a redox reaction is given by,

$$\Delta G_r = \Delta G_r^0 + RT \ln \frac{[D^+]^{\nu_{D^+}} [A^-]^{\nu_{A^-}}}{[D]^{\nu_E} [A]^{\nu_A}} \tag{69}$$

Where ΔG_r^0 is the standard free energy change, which is temperature dependent (Amend and Shock 2001)

$$\Delta G_r^0 = \sum_i \nu_{i,r} \Delta G^0 \tag{70}$$

where ΔG^0 is the Gibbs free energy change compounds in the chemical reaction considered. Values of ΔG^0 are dependent on temperature as well (Amend and Shock 2001). Values of ΔG_r^0 are calculated using the program OrganoBioGeoTherm (OBIGT). It is important to include thermodynamic constraints since reactions might be endergonic ($\Delta G^0 > 0$) under standard conditions but exergonic ($\Delta G_r < 0$) under in situ conditions or the other way around.

The energetics of the chemical reactions of interest show very little change over a narrow temperature range near 25°C. However, accurately determining the energetics at a pressure 250 bar and at temperatures between 2°C and 350°C requires accurate thermodynamic properties at this pressure and these temperatures.

Many thermophiles and hyperthermophiles are also barophiles, i.e. the metabolic processes may also be affected by pressure. In general, the effect of pressure on values of the molal Gibbs free energy of formation (ΔG^0) between P_{SAT} and 1 kbar is significantly less than the effect of temperature from 0 to 100°C (Amend and Shock 2001). In other words, at most conditions of biological interest, and this includes our model calculations where pressure is assumed to be a constant 250 bar, the effect of pressure on ΔG^0 is secondary to that of temperature.

Controls over biogeochemical reaction in nature are far more complex than what is usually anticipated. Quantitative estimates of kinetic parameters for biologically mediated reactions represent a collective response of the microbes to a number of environmental factors of which temperature is the most important one (Roychoudhury 2004). Because temperature is such an important and variable factor, it is difficult to obtain reasonable values for the kinetic parameters. This becomes even more complex due to the fact that the kinetic parameters and their temperature dependency differ per microbe (Roychoudhury 2004).

Mesophiles, thermophiles and hyperthermophiles exhibit a temperature optimum at which the rate of reduction or oxidation is highest. For thermophiles the optimum growth temperature lies above 45°C while for hyperthermophiles the optimum and maximum growth temperature are at least 80°C and 90°C, respectively (Amend and Shock 2001). Microbes have been living (and growing) in environments with temperatures as high as 121°C (Kashefi and Lovley 2003), but the upper limit of life remains yet unknown. Microbial ribosomal DNA (rDNA) showing substantial diversity was recovered from black smoker vent water in the Ihaya Basin, Okinawa Trough, at a temperature of >300°C, which is far above the upper temperature limit for life found so far (Takai, Komatsu et al. 2001). In this model, the upper temperature for life is taken to be 150ºC.

To serve as an energy source for an organism, reactions have to be thermodynamically favored but kinetically inhibited. As temperature increases, reaction rates also increase, and at some elevated temperature, abiotic reaction rates are so fast that there is not enough energy gain for an organism to catalyze a reaction. Therefore, at high temperatures, it might be that the rapid abiotic reaction rates that cause reaction to equilibrate that places a limit on life and not temperature itself (Amend and Shock 2001). In other words, at high temperatures, the reaction might be thermodynamically inhibited (F_T=0)

4. Results and discussion

The model that is described in the model set-up is the model that is eventually developed to describe a hydrothermal vent chimney and the results of the model will be discussed later in this chapter. Before this model, several less detailed models have been developed to give insight in the effect and sensitivity of different parameters.

4.1 Diffusion model (constant temperature)

The first model developed is a very basic model considering only diffusion and equilibrium reactions. The values for the rate constants k_i are set to 0, meaning that the rates of the reactions are also zero. The values for the equilibrium constants are independent of temperature and pressure and can be found in table 3. Pressure is taken to be 250 bar ($P=P_0$) and the activity coefficient for each reaction is stated as 1, so concentration equals activity.
Instead of the calculation of the solution coefficients as described in the model set-up, the diffusion coefficient of the solution is calculated using the much simpler linear rate law

$$D^* = D_0(1+\frac{m_1}{m_0}T)\cdot 10^{-6} \tag{71}$$

where D_0 is the diffusivity constant at 0°C and m_1/m_0 equals α, which is the temperature dependency of the diffusion coefficient (Boudreau, 1992). Values for D_0 and α used are listed in appendix 2. The values found for D^* are corrected for salinity and tortuosity. The salinity and tortuosity correction are calculated by

$$S_{corr} = 0.95 - 1\cdot 10^{-3} S \tag{72}$$

$$D^n = \frac{D^{'}\cdot S_{corr}}{1-\log(\varphi^2)} \tag{73}$$

The model ran for two months, with time steps of 10^{-6} yr. The total length of the chimney is taken to be 3 cm, with 1000 nodes in space; this means that the distance between two subsequent nodes represents 30 µm. The temperature is taken to be a constant 100°C throughout the system. The porosity profile is also taken to be constant throughout the system with φ=0.3. Values for the equilibrium constants of the dissociation reactions at a temperature of 100°C and a pressure of 250 bar were calculated using the OBIGT software which uses the SUPCRT92 database. The values can be found in table 3.

Equilibrium Reaction	K_{eq}
$H_2S(aq) \rightarrow HS^-(aq) + H^+(aq)$	$10^{-6.4248}$
$H_2CO_3 \leftrightarrow H^+ + HCO_3^-$	$10^{-6.2875}$
$HCO_3^- \leftrightarrow H^+ + CO_3^{2-}$	$10^{-9.9601}$
$H_2O \leftrightarrow H^+ + OH^-$	$10^{-12.1731}$

Table 3: *Values used for the equilibrium constant K_{eq} for the equilibrium reactions implemented in the model. Values of K_{eq} were calculated by the use of the OBIGT software that uses the SUPCRT92 database.*

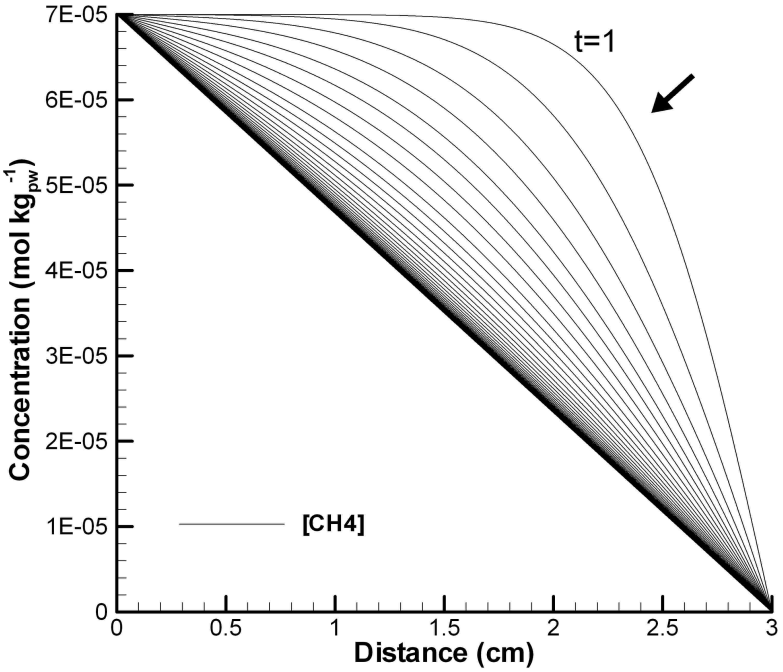

Figure 3*: Approach to steady state for CH_4 versus distance. Each line represents 0.001 year. The concentration is given in mol per kg of pore water. The arrow denotes the direction towards steady state and the line with t=1 denotes the concentration after the first time step.*

To check whether the model is in steady state one has to look at the conservative quantities. All species not involved in an equilibrium reaction (i.e. CH_4, SO_4^{2-}, H_2, O_2) should follow a straight line between their end-member compositions when in steady state. This is true for all of the species not involved in an equilibrium reaction. In figure 3, the approach to steady state for CH_4 is depicted. The ionic species Ba^{2+}, Ca^{2+}, Fe^{2+}, Cu^{+}, Pb^{2+} and Zn^{2+} also follow a straight line between their boundary conditions. These species are conservative because they are not involved in any reaction since no complex- or mineral formation reactions have been included in the model.

The species involved in equilibrium reactions have conservative quantities that should follow a straight line between end-member compositions, as long as the diffusion coefficients of these species are equal or at least comparable. These conservative quantities are alkalinity, total reduced sulfur (S_T) and dissolved inorganic carbon (DIC).

$$Alk = [HCO_3^-] + 2[CO_3^{2-}] + [HS^-] - [H^+] \tag{74}$$

$$DIC = [CO_2(aq)] + [HCO_3^-] + [CO_3^{2-}] \quad (75)$$

$$S_T = [H_2S] + [HS^-] \quad (76)$$

The alkalinities at the boundaries are -0.598 mmol kg_{pw}^{-1} at the hydrothermal vent side and 2.29 mmol kg_{pw}^{-1} at the sea bound side. DIC is 6.0 mmol kg_{pw}^{-1} at the hydrothermal vent side and 2.36 mmol kg_{pw}^{-1} at the seawater side. Total reduced sulfur is 7.30 mmol kg_{pw}^{-1} at the hydrothermal vent side and 0.0 mmol kg_{pw}^{-1} at the seawater side. If the system attained a steady state condition, the values for these quantities in the chimney wall should fall in a straight line between both boundaries. Figure 4a shows that DIC, TRS and alkalinity all fall in a straight line when diffusion coefficients are equal. Once the diffusion coefficients found in appendix 2 are implemented in the model, the lines for DIC, TRS and alkalinity do not fall in a straight line (figure 4b), this is due to the differences between the diffusion coefficients.

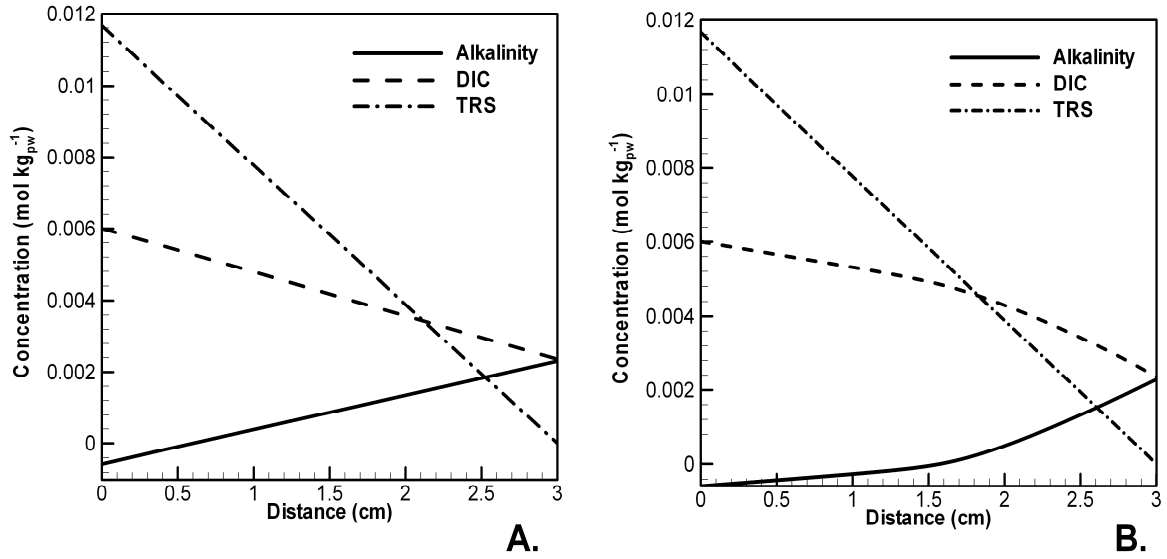

Figure 4: *Plots of total reduced sulfur and DIC, alkalinity versus the distance from the hydrothermal vent after the model ran for 0.2 years. The hydrothermal vent side lies at a distance of 0 cm while the sea bound side lies at a distance of 3 cm. Temperature is assumed to be 100°C throughout the profile. Concentrations are given in mole per kg of porewater. A) Profiles of DIC, TRS and Alkalinity when the diffusion coefficients of all species are equal. B) Profiles of DIC, TRS and Alkalinity when the tracer diffusion coefficients are different (see appendix 2).*

The saturation indices for the different mineral formation reactions have been calculated with the model outcome using equation 63. According to these calculations, anhydrite will precipitate between 0.04 cm and 3.0 cm, pyrrhotite between 1.5 cm and 3.0 cm and all other minerals assumed have saturation indices above zero over the entire range which means that all minerals will be present over the entire range. Chalcopyrite has the highest saturation index over the entire range.

4.2 Diffusion and advection model (constant temperature)

The next model incorporates an advection of 3×10^{-7} m s^{-1} (or 94.9 cm yr^{-1}) inward from the hydrothermal vent side. Inward advection of hydrothermal fluid advects species present in this hydrothermal fluid further towards the seawater side which means that they are available over a wider range of distances. Only advection inward from the hydrothermal vent side is considered, inward advection of seawater is ignored. The results for DIC, TRS and alkalinity are shown in figure 5, from which it becomes clear that advection has a profound effect on species distribution.

The advection of hydrothermal vent fluid inward also affects the SI values and thus the mineral composition when compared to the situation without advection. Andhydrite has a positive saturation index between 0.4 cm and 3 cm, barite has a positive SI value between 0.06 cm and 3 cm and pyrrhotite will precipitation between 1.8 cm and 3 cm. The difference between barite and andhydrite precipitation when compared to the non-advective case is the result of a decrease in the sulphate concentration which is diffusing in the direction of the hydrothermal vent side but advecting in the opposite direction. The pyrrhotite starts precipitating further towards the seawater side when compared to the non-advective model due to an increase in the H^+ concentration towards the seawater side resulting from advection, this increase of protons results in a decrease of the IAP.

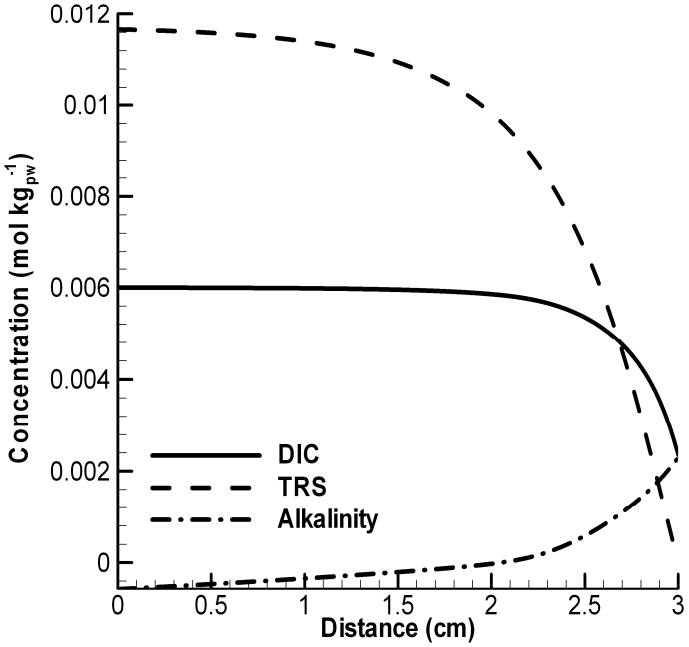

Figure 5: *Dissolved Inorganic Carbon (DIC), Total Reduced Sulfur (TRS) and Alkalinity versus distance from the hydrothermal vent once advection is implemented.*

4.3 Diffusion, advection & reaction model (constant temperature)

In this model, the rate constants for the different microbial redox reactions were added. The rate law used in this model is not the Michaelis-Menten rate law which is often used to model metabolisms for unicellular organism, but a simpler bimolecular rate law in which the rate is dependent on the concentrations of the reactants and a second order rate constant (k_i) (see table 4). Simple bimolecular rate equations are usually able to reproduce the distribution of reactants and rates, although this might not be the case once the temperature gradient is implemented. The rate parameters used are best fitting parameters. In itself, a bimolecular rate equation does not provide insight into the possible thermodynamic limitations, therefore the predictive capability of the equation remains limited (Dale, Regnier et al. 2006).
For methanotrophy, anoxic oxidation of methane (AOM), H_2S and HS^- oxidation, values for the rate constants were found in literature (van Cappellen and Wang 1996), for all the other reactions implemented, no rate constants are found, but they are believed to be orders of magnitude smaller, with the Knallgas reaction having the lowest rate constant. The equilibrium constants for the carbonate system and the sulfide dissociation reaction were taken to be the same as in the previous model (table 3). The temperature was still a constant 100°C throughout the system, the porosity remains a constant throughout the system with φ=0.3. The model ran for 0.2 years with time steps of 10^{-6} year. A complete overview of the reactions and their corresponding rates can be found in appendix 1.

Rate constant	Value	Unit
k_{mt}	$10 \cdot 10^{10}$	$kg/(mol \cdot yr)$
k_{mg}	10^3	$kg/(mol \cdot yr)$
k_{mg2}	10^3	$kg/(mol \cdot yr)$
k_{kn}	10	$kg/(mol \cdot yr)$
k_{so1}	$1.6 \cdot 10^5$	$kg/(mol \cdot yr)$
k_{so2}	$1.6 \cdot 10^5$	$kg/(mol \cdot yr)$
k_{sr}	10^3	$kg/(mol \cdot yr)$
k_{aom}	10^6	$kg/(mol \cdot yr)$

Table 4: *Rate constants used in the diffusion, advection and reaction model (constant temperature) for each of the reactions. The subscripts denote the reactions with mt being methanotrophy, mg methanogenesis using CO_2, mg2 methanogenesis using HCO_3^-, kn denotes knallgas,, so1 sulfide oxidation with H_2S, so2 sulfide oxidation using HS^-, sr being sulfate reduction and aom anoxic oxidation of methane.*

Steady state concentrations of the different species used by microbial metabolisms are given in figure 6, the corresponding rates of reactions for the different metabolisms are shown in figure 7. Once the model is in steady state, the concentration of the different species remain constant, this means that the rate of production/consumption of species is also constant. The steady state production and/or consumption of species is shown in figure 8.
In the graphs, a distinction is made between the model including only diffusion and reaction and the model including diffusion, advection and reaction. This is done to distinguish between the effects of diffusion and advection on the model. As can be seen from the figures 5 to 7, advection changes the distribution of species, the resulting reaction rates and the consumption and production of the different species significantly.

From figure 6 it becomes clear that once the reactions are implemented, species do not follow a straight line between both boundary conditions. When advection is added, the concentration profiles deviate even further from a straight line. Species available in relatively high concentrations at the hydrothermal vent side are pushed further inward due to advection which affects the reaction rates.

Oxygen and hydrogen are not produced in any of the microbial reactions, which can be deducted from the reactions and their stoichiometry. This can also be seen in figure 8A and 8B, were the production of O_2 and H_2 is negative which corresponds to consumption of these species. The oxygen consumption profiles both show that at some point there is no more oxygen consumed since there is no more oxygen available in the vent, this happens at a distance of ~1.25 cm from the hydrothermal vent for the case without advection and at a distance of ~2.0 cm from the hydrothermal vent for the model when advection is included. Due to advection inward from the hydrothermal vent side oxygen is available over a smaller range. The absence of O_2 at the corresponding distances is also seen in figure 6A and in figure 7C and 7D, where the rate of the oxygen consuming reactions (methanotrophy, sulfide oxidation) is zero. The rate of the Knallgas reaction is negligible compared to all the other rates and not plotted in any of the graphs.
The O_2 consumption profile from figure 8B shows two depressions; one at a distance of ~2.35 cm and the other one at a distance of ~2.8 cm. The CH_4 production profile shows a small depression in combination with an apex in the CO_2 profile at ~2.35 cm. This depression in the O_2 profile can thus be explained by methanotrophy which is in line with the optimum in the rate of methanotrophy seen in figure 7D. The larger depression in O_2 consumption at ~2.8 cm is in line with the depression in H_2S production profile and an optimum in the SO_4^{2-} production profile (figure 8F). This second depression is the result of an optimum in the rate of H_2S oxidation (figure 7D).
The hydrogen is consumed as a result of methanogenesis and sulfate reduction. This reduction of CO_2 and SO_4^{2-} is ongoing throughout the profile and only starts to decrease once the concentration of H_2 starts decreasing. Since H_2 is available throughout the vent, H_2 is consumed throughout the vent and methanogenesis en sulfate reduction occur throughout the vent. For methanogenesis, both CO_2 and H_2 become limiting at the seawater side. For sulfate reduction, SO_4^{2-} is limiting at the hydrothermal vent side (Figure 6E), while H_2 is limiting at the seawater side (figure 6C).
The maxima in production of HS^- and HCO_3^- coincide with the maxima in consumption of CH_4 and SO_4^{2-} (figure 8C to 8F), which in their turn correspond to the maximum rate of anoxic oxidation of methane (figure 7A and 7B). The rates of AOM are plotted in different graphs than the other rates since these rates are significantly larger. The fast reaction rates of AOM result in the species profiles of CH_4 and SO_4^{2-} as seen in figure 5A and 5E. The profiles of HCO_3^- and HS^- are also affected by the rate of anoxic oxidation of methane. Due to the low pH of the vent fluid (figure 6F), the profiles of CO_2 and H_2S are also the result of the fast AOM reaction rate. As a result of the low pH, HCO_3^- and HS^- formed by the AOM reaction immediately lose their proton to give CO_2 and H_2S respectively. The AOM reaction occurs over a broader part of the vent, but

at a slower rate once advection is implemented in the model. While the AOM reaction takes place at a distance between 0 and ~1.8 cm in the run without advection, the AOM reaction occurs at distances between 0 and ~2.5 once advection is implemented. The broadening is the result of the advective flux of CH_4 further towards the seawater side. The decrease in the maximum rate results from the decrease in the concentration of sulfate. Besides advection of SO_4^{2-} back towards the seawater side, the decrease in the concentration of sulfate overall is the result of the increased flux of H_2 due to advection, which causes an increase in the overall concentration of H_2 resulting in the maximum rate of sulfate reduction being at a distance of ~2.3 cm instead of ~1.3 cm. So, due to increased availability of hydrogen at the seawater side, resulting in an increased rate of sulfate oxidation closer to the seawater site, less sulfate is diffusing towards the hydrothermal vent side, which causes the maximum rate of AOM to decrease.

Overall, once advection is added to the model, the reduced species available at the hydrothermal vent side are advected further towards the seawater side which results in the availability of oxygen over a smaller area due to increased rates of redox reactions involving oxygen. This causes the oxygen concentration to decrease faster. The decrease in oxygen causes it to diffuse less towards the hydrothermal vent side resulting in a smaller oxic zone.

Saturation index calculation shows not much difference with the previous model since concentration gradients of Ba^{2+}, Ca^{2+}, Fe^{2+}, Cu^{+}, Pb^{2+} and Zn^{2+} do not change due to implementation of the microbial reactions. Anhydrite has a saturation index above zero between 0.44 and 3.0 cm, barite between 0.07 and 3.0 cm and pyrrothite between 1.5 and 3.0 cm. All other minerals have SI values above zero between 0 and 3 cm and are therefore expected to precipitate over the entire range. The only concentrations that change and affect the ion activity products of different minerals are the concentrations of H_2S, H_2, H^+ and SO_4^{2-}, the change in H_2S will affects precipitation of covellite, galena, pyrite, pyrrhotite, sphalerite and wurzite. Changes in the concentration of H^+ affects formation of chalcopyrite, galena, pyrite, pyrrhotite, sphalerite and wurzite while changes in the concentration gradient of H_2 due to implementation of microbial reactions affects the IAP and therefore the saturation index of chalcopyrite, covellite, galena and pyrite. The concentration change of SO_4^{2-} will affect anhydrite and barite precipitation. The changes in the concentrations of the species affecting mineral precipitation and dissolution are not large enough to establish a significant change in the saturation index of the minerals considered. Thus, the likelihood that minerals will or will not precipitate does not change once microbial reactions are implemented because changes in the concentration gradients of H_2, H_2S, H^+ and SO_4^{2-} are not large enough.

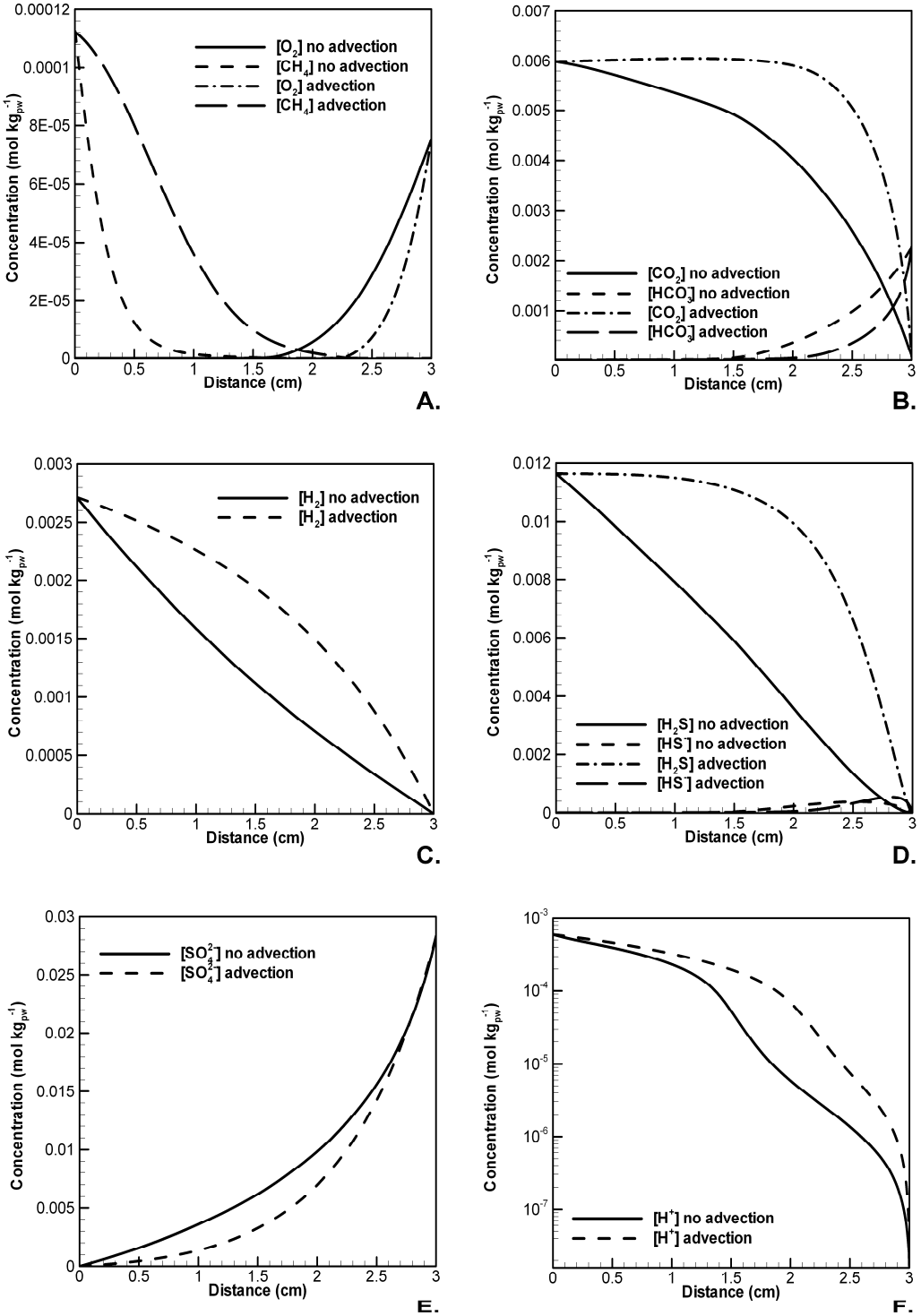

Figure 6: *Steady state concentrations of the species included in the model. The total model time was 0.2 years. Distance represents the distance from the vent with 0 being the hydrothermal fluid side and 3 being the seawater side. Concentrations at the boundaries are assumed to be those of seawater and 21°N EPR hydrothermal fluid (see table 1). The concentration is given in mol per kilogram of porewater (mol kg_{pw}^{-1}). The scales on the y-axes are different.*

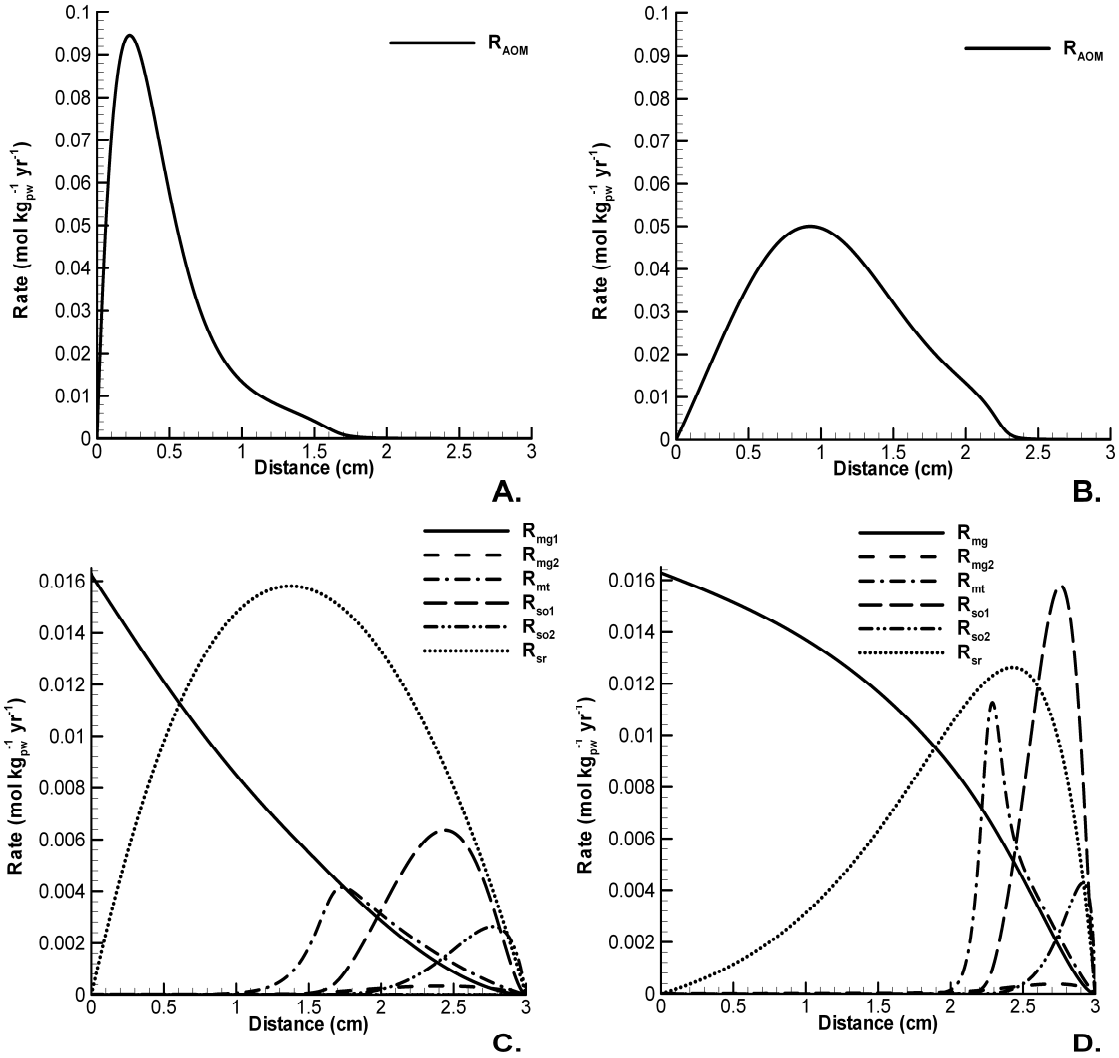

Figure 7: *Reaction rates for the individual reactions.* **A)** *Reaction rate for the anoxic oxidation of methane without advection* **B)** *Reaction rates for the AOM reaction once advection is implemented* **C)** *Reaction rates for the methanogenis with CO_2 (mg1) and HCO_3^- (mg2), methanotrophy (mt), sulfide oxidation with H_2S (so1) and HS^- (so2) and sulfate reduction (sr), advection is not implemented* **D)** *Individual reaction for methanogenesis, methanotrophy, sulfide oxidation and sulfate reduction. The scales on the y-axes are different for the rate of AOM and the other reactions.*

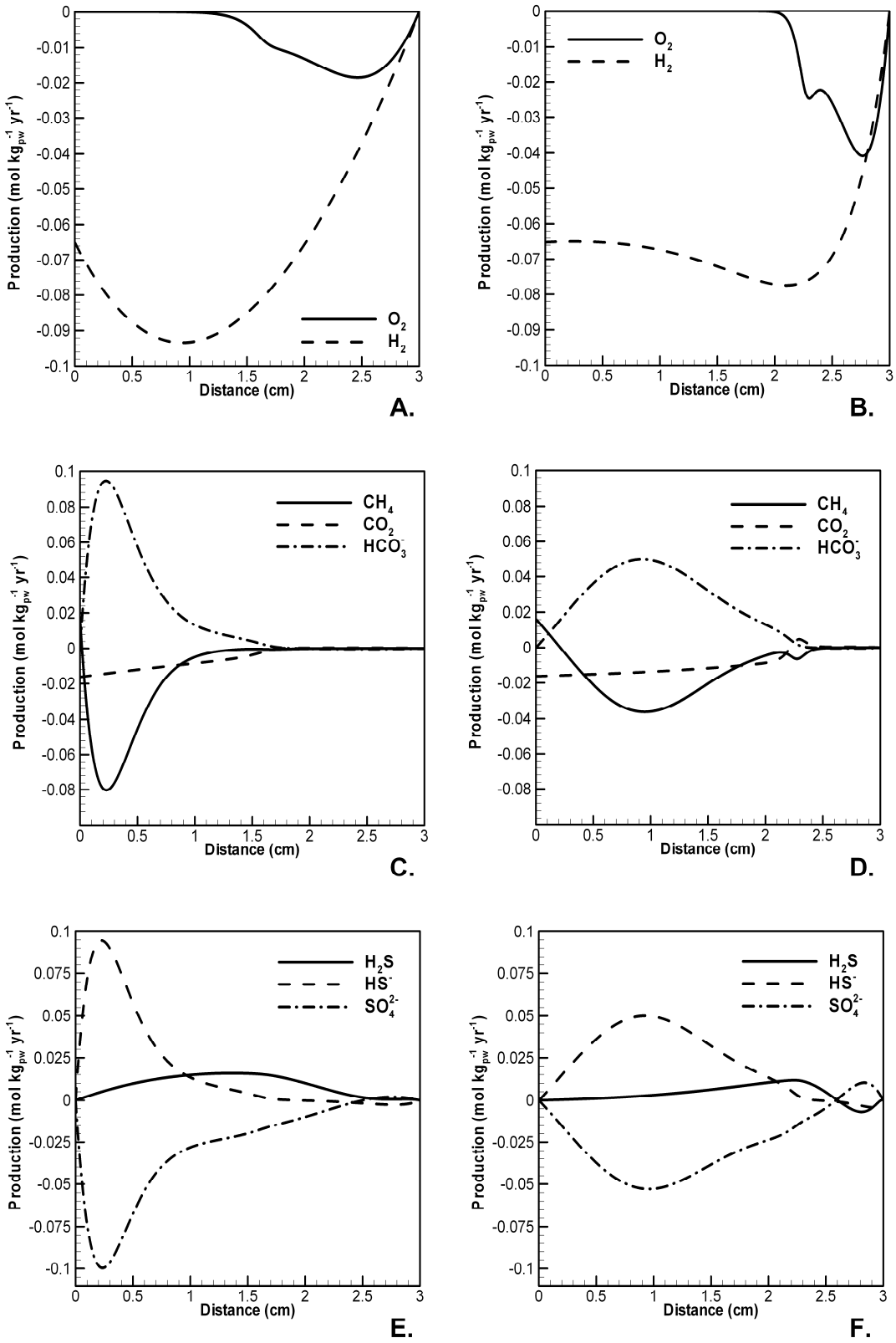

Figure 8: *Production of species as a result of reactions described above. Values of production were calculated using the rate laws for a reaction involving a specific species and the stochiometry of the reactions. A negative production means that the species is consumed. The graphs on the left side shows the production of species without advection. Advection is included in the graphs on the right side. The scales on the y-axes are different.*

4.4 Diffusion, advection and reaction model (temperature gradient)

The most important physical condition affecting the chemistry and biology in a hydrothermal vent chimney is the steep temperature gradient (Tivey 1995). With boundary conditions of 2°C at the seawater side and 350°C at the hydrothermal side, there will be a temperature difference of 348°C over a distance of just 3 cm. Therefore, the next step in our model is the incorporation of the temperature gradient.
As described in the model set-up section, the temperature gradient is dependent on the thermal diffusivity which is determined by the thermal conductivity, heat capacity and density of the rock and pore fluid. The porosity determines the partition between rock and pore fluid and is therefore and important parameter to determine the thermal diffusivity and therefore affects the temperature profile.
Each rock type has a specific thermal conductivity, heat capacity and density which will affect the temperature gradient. Although the hydrothermal vent modeled in this research is a pure anhydrite layer with a constant porosity it is important to realize how differences in mineral composition (rock type) and porosity might affect the thermal diffusivity and thus the temperature profile. A single layer of anhydrite only mimics the first stages of a hydrothermal vent. Therefore, the changes in thermal diffusivity as a function of temperature for an anhydrite layer with porosities of 0.3 and 0.05 are compared to the changes in thermal diffusivity as a function of temperature for a pyrite layer with porosities of 0.3 and 0.05. As can be seen in figure 8A, the change in porosity from 0.3 to 0.05 affects both the anhydrite and pyrite layer. However, the most significant difference between thermal diffusivities is the result of the difference in rock type where the sulfide dominated rock (pyrite) has a much higher thermal diffusivity when compared to anhydrite. This means that the mineral composition of a hydrothermal vent has a major effect on the temperature profile which in turn will affect species distribution.

As described in the model set-up, the diffusion coefficients of the different species are also affected mostly by temperature. This is depicted in figure 9B, where the change in diffusion coefficient for the non-electrolyte CH_4 and the electrolyte SO_4^{2-} are plotted against temperature, respectively. As can be seen in these figures, the diffusion coefficient of both CH_4 and SO_4^{2-} show a 50 fold increase between a temperature of 273.15 K and 623.15 K. These examples show that both for non-electrolyte species and electrolyte species, the diffusion coefficient and hence diffusion is very much affected by large changes in temperature.

The equilibrium constants are temperature dependent and will vary due to the temperature gradient in the vent. The variation in the equilibrium constants will affect the speciation of carbonate and sulfur species, which in turn will affect diffusion and reaction. The effect of temperature and pressure on the equilibrium constants for the different equilibrium reactions, including mineral precipitation and dissolution reactions have been calculated by the use of the OrganoBioGeoTherm software. The dependency of the equilibrium constants as a function of temperature, assuming a constant pressure of 250 bars, was then modeled into the interface.
Reaction rates are not dependent on temperature because in this model, the rate constants are independent of temperature. Indirectly, reaction change are dependent on temperature because the concentration gradients of the species used by microbes are changed as a result of the temperature dependent diffusion.

Instead of a constant value for each species (i.e. initial constant value) an initial input file for each species is implemented in this model including temperature, which is implemented as a species. The input files describe the species and temperature as a straight line between both boundary conditions. The total model time was 0.1 year with time steps of 10^{-6} years.
Once the temperature gradient is implemented as described by the model set-up, the interface (www.geo.uu.nl/~kbrtm) is not sufficient enough to implement temperature and the temperature

dependent diffusion coefficient and temperature as described in the model set-up. To implement temperature and the species dependent, advanced calculation for the diffusion coefficient, a new algorithm was written and implemented in the 'advdiffcoeff.for' subroutine. The complete codes can be found in appendix 3.

The steady state temperature gradient with and without advection is depicted in figure 10, which shows that an advection rate of 3×10^{-7} cm yr^{-1} has an effect on the temperature gradient by increasing the temperature throughout the profile. In the middle of the vent, temperature differences between the situation with and without advection can be up to 50 K. The temperature gradient without advection included is comparable to results found by models from Tivey and McDuff (1990), who found that the temperature gradient is not affected by advection for advection rates up to 2×10^{-7} cm yr^{-1}.
To see the overall effect of the temperature gradient and the advanced diffusion coefficients, the results of the steady state species concentrations are depicted in figure 11, the rates of the individual reactions are depicted in figure 12 and the rates of production and consumption for the different species in the model including the steep temperature gradient and temperature dependent diffusion coefficient are plotted in figure 13.

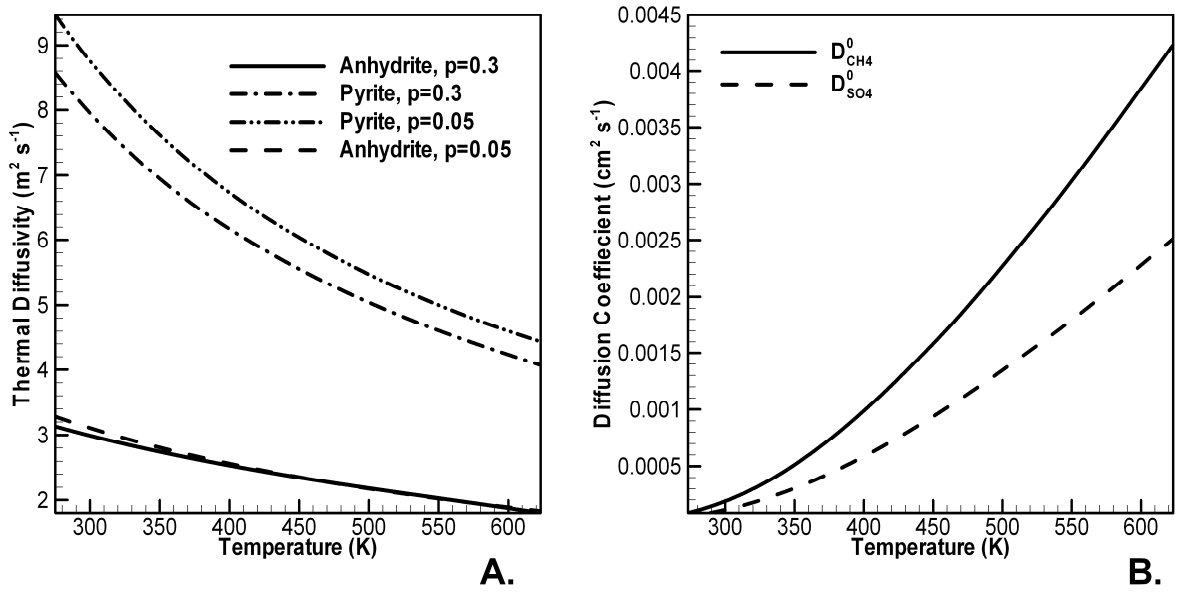

Figure 9: A) *The thermal diffusivity of anhydrite and pyrite as a function of temperature and porosity* **B)** *The value of the diffusion coeffiecient of CH_4 and SO_4^{2-} as a function of temperature.*

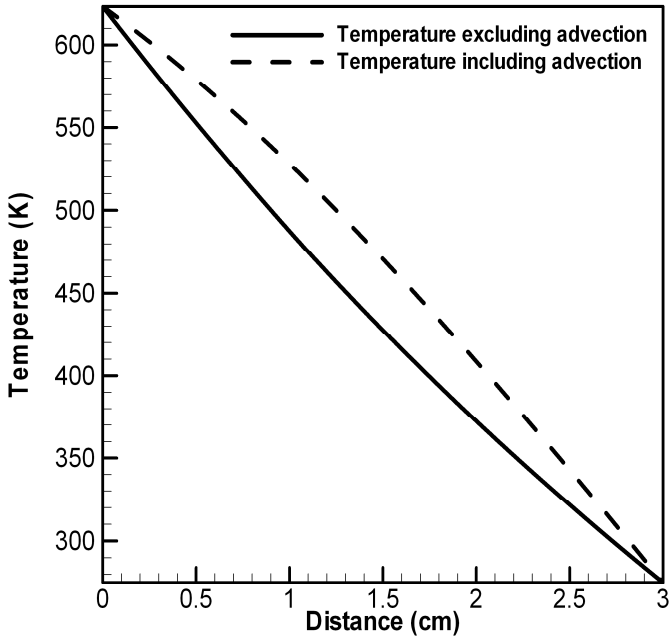

Figure 10: *The temperature profile with and without advection as a function of distance. The distance represents the distance from the vent with 0 being the hydrothermal fluid side and 3 being the seawater side. The rate of advection used was* 3×10^{-7} *cm* yr^{-1}.

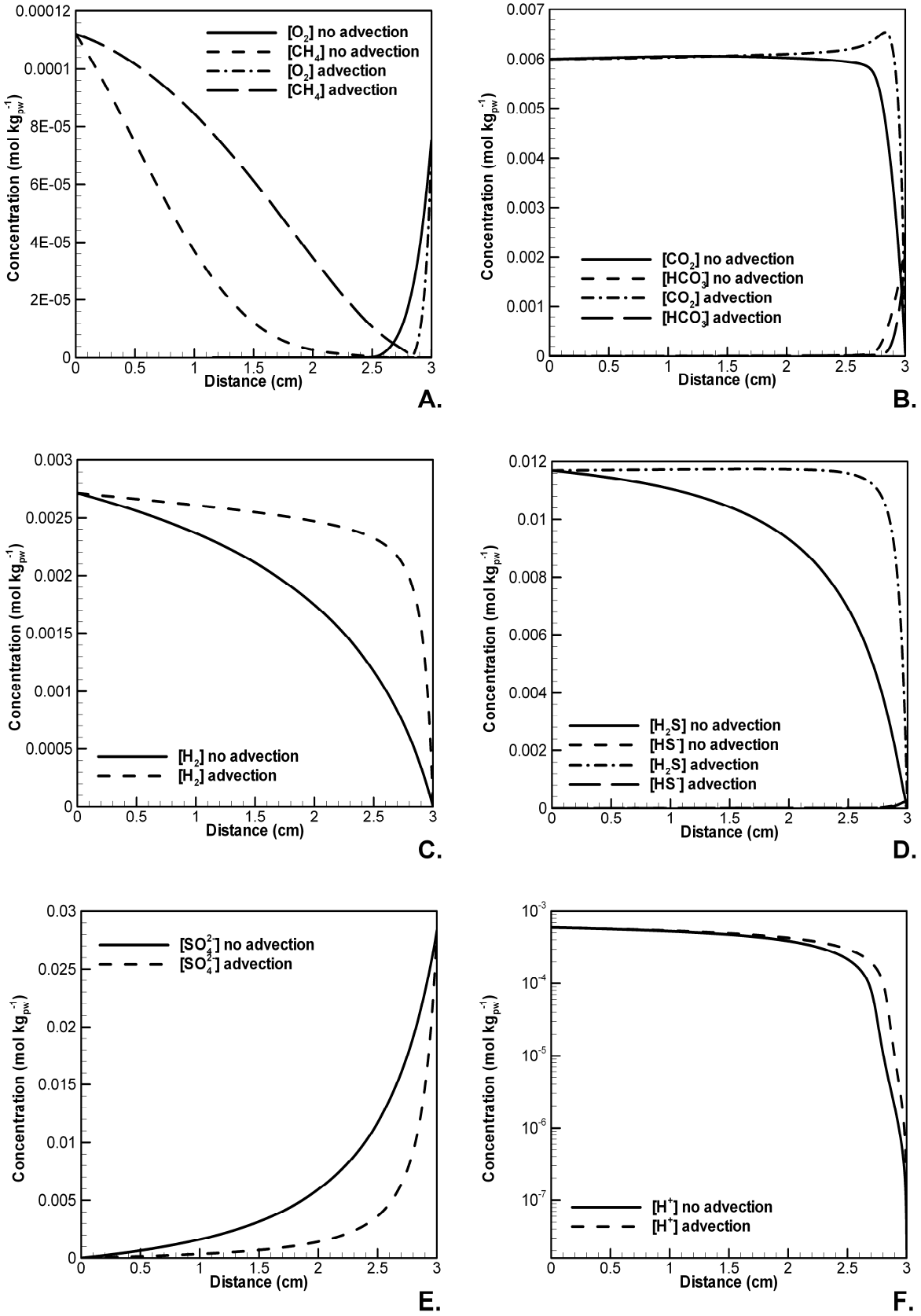

Figure 11: *Steady state concentrations of the species used by microbial metabolism. The total model time was 0.2 years. Temperature and temperature dependent diffusion coefficients were implemented. The distance represents the distance from the vent with 0 being the hydrothermal fluid side and 3 being the seawater side. Concentrations at the boundaries are assumed to be those of seawater and 21°N EPR hydrothermal fluid (see table 1). The concentration is given in mol per kilogram of porewater (mol kg_{pw}^{-1}). The scales of the y-axes are different.*

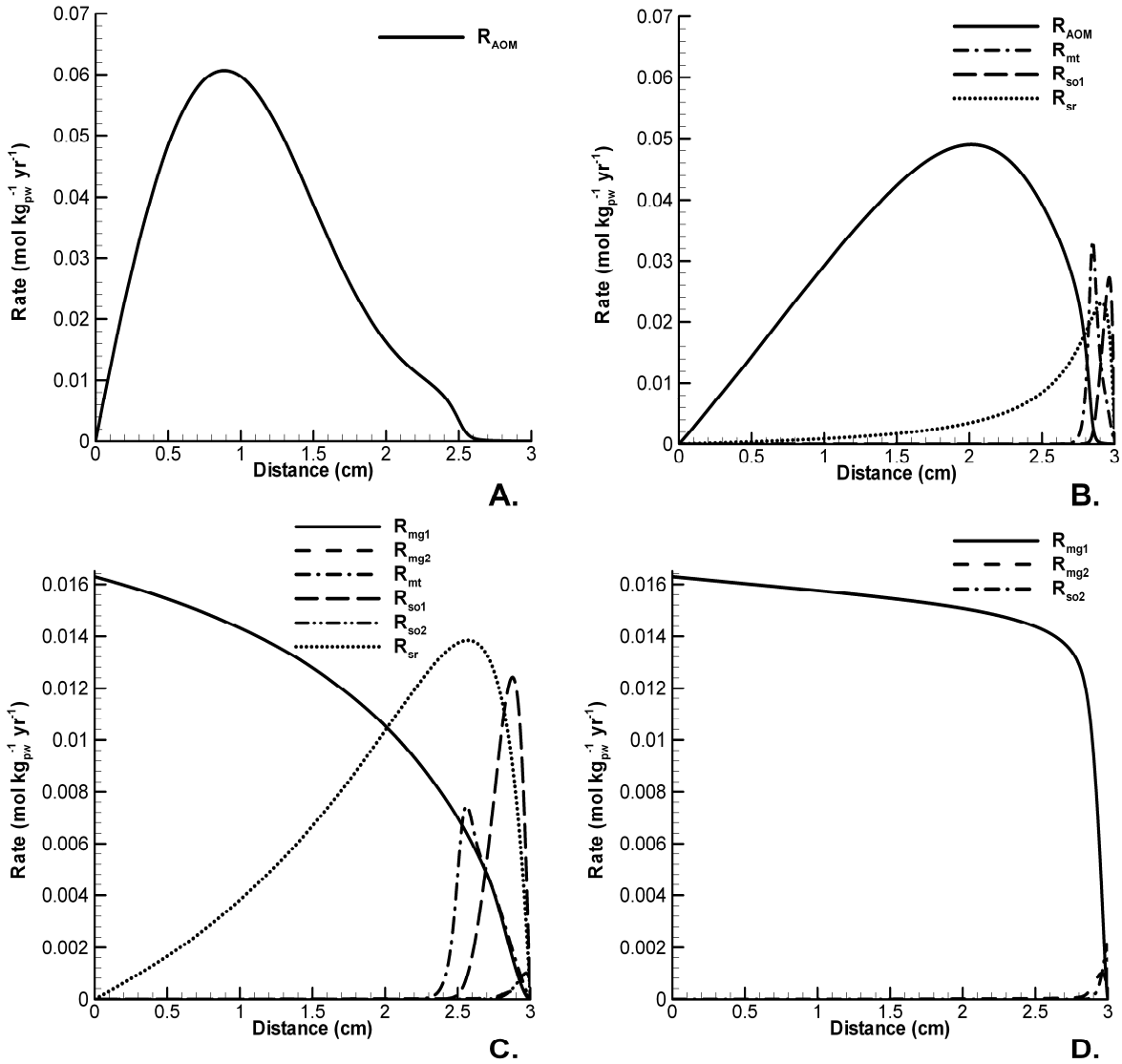

Figure 12: *Rates of individual reactions.* **A)** *Reaction rates of the anoxic oxidation of methane for the model without advection* **B)** *Individual reaction rates for AOM, methanotrophy (mt), H_2S oxidation (so1) and sulfate reduction (sr) for the model with advection* **C)** *Reaction rates for methanogenesis with CO_2 and HCO_3^-, methanotrophy, H_2S oxidation and HS^- oxidation and sulfate reduction for the non-advective model* **D)** *Reaction rates for CO_2 reduction, HCO_3^- reduction and oxidation of HS^-. The scales on the y-axes are different.*

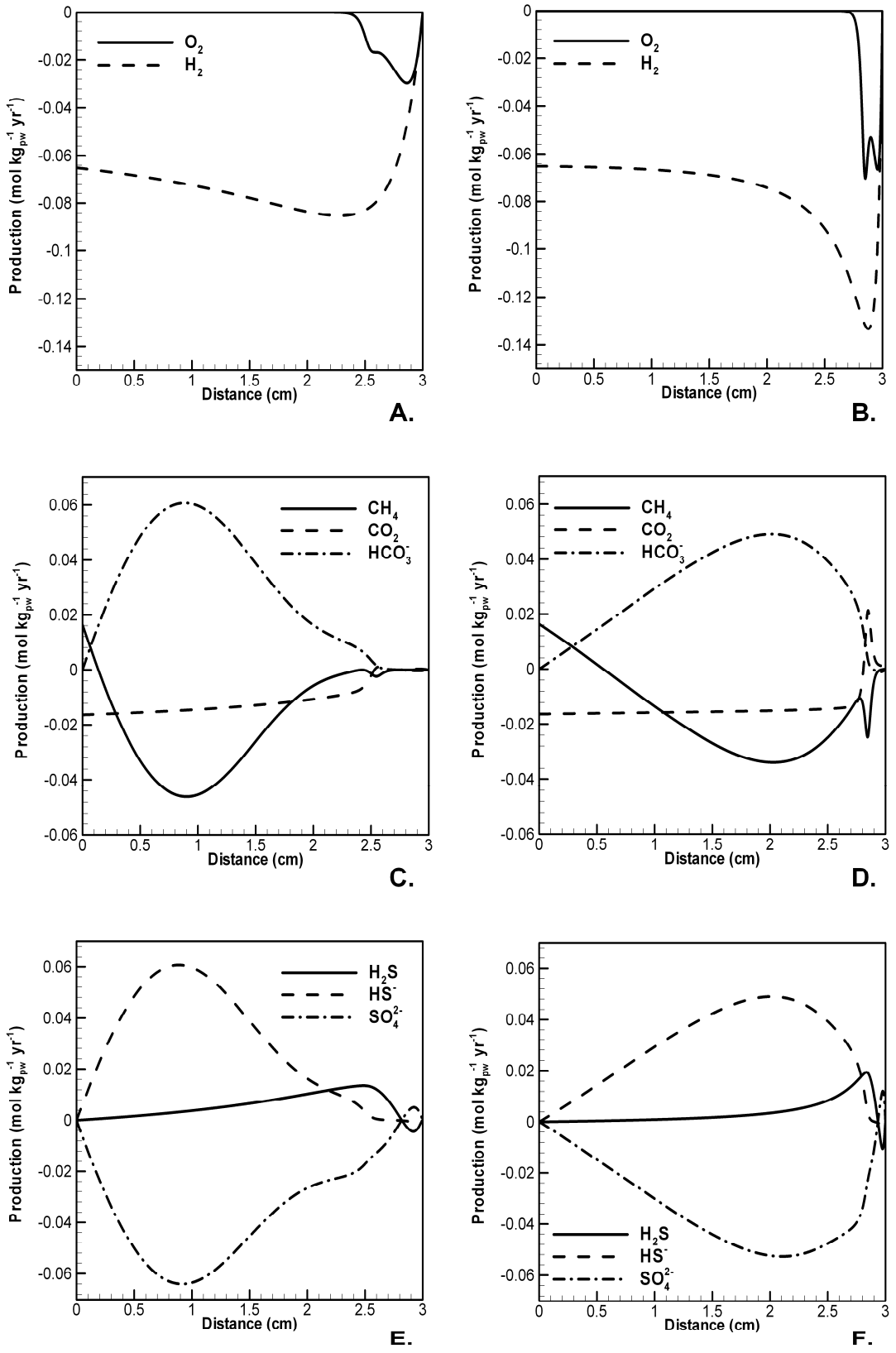

Figure 13: *Production of species as a result of reactions described above. The total model time was 0.2 years. Temperature and temperature dependent diffusion coefficients were implemented. Values of production were calculated using the rate laws for a reaction involving a specific species (e.g. CH_4) above and the stochiometry of the reactions. A negative production means that the species is consumed. The graphs on the left only include transport by diffusion, the graphs on the right include transport by diffusion and advection. The scales on the y-axes are different.*

By combining figures 11 to 13 it becomes clear that AOM significantly affects the species distribution of HS^-, SO_4^{2-}, CH_4 and HCO_3^-. The anoxic oxidation of methane is limited by the availability of CH_4. Once CH_4 is not present at a distance of ~2.6 cm (for the model excluding advection) or ~2.8 cm (for the model including advection) (figure 11A), the rate of reaction for AOM becomes zero (figure 12A and 12B). At this point, both methane and oxygen are available, albeit in small quantities, which causes the rate of methanotrophy to peak (figure 12C and 12B). Even with low concentration of CH_4 and O_2, the rate of methanotrophy is high because of the high reaction rate constant. The peak in the rate of methanotrophy corresponds to the smaller depression in the consumption of CH_4 in both the model with and the model without advection at ~2.6 cm and ~2.8 cm, respectively (figure 13C and 13D).
The AOM reaction results in production of HCO_3^-, as can be seen in figure 13C and 13D. This cannot be seen in figure 11B because once the HCO_3^- is produced it is immediately converted to CO_2 as a result of the relatively low pH throughout the hydrothermal vent (figure 11F).
In both the model excluding advection and the model including advection there are two depressions in the consumption profile of oxygen, although they are located more toward the seawater side and closely together once advection is included. These depressions correspond to the maximum rate of methanotrophy and H_2S oxidation, respectively, which both consume oxygen. The increase in CO_2 at a distance of ~2.85 cm in the model including advection (figure 11B) is also resulting from a peak in the production of CO_2 (figure 13D) resulting from methanotrophy, whose rate is maximum at ~2.85 cm (figure 12B).
Due to the availability of H_2, CO_2 and SO_4^{2-} throughout the profile (figure 11B, 11C and 11E), sulfate reduction and CO_2 reduction take place throughout the entire profile (figure 12B, 12C and 12D) where the maximum rate of sulfate reduction lies at a distance of about 2.6 cm for the non-advective case, and at a distance of about 2.8 cm for the advective case. This corresponds with the depression of H_2 seen in figure 13A and 13B, and the production of H_2S in figure 13E and 13F.

Since the temperature is not a constant 100°C throughout the model anymore but follows the lines as seen in figure 9, the diffusion of species is increased at the hydrothermal vent side. Diffusion rates are increased at the hydrothermal vent side due to the high temperature and decreased at the seawater side due to the decrease in temperature. This can be deduced from figure 11 where the reduced species (CO_2, CH_4, H_2, H_2S and H^+) are available over wider distances when compared to the situation with a constant temperature throughout the profile. Furthermore, O_2 and SO_4^{2-} are diffusing slower in the direction of the hydrothermal vent side due to the lower temperatures and the resulting lower diffusion coefficients at the seawater side.
Thus, the slower diffusion rates at the seawater side results in less availability of oxygen and sulfate towards the hydrothermal vent side. This results in more available oxygen closer to the seawater side which causes the rates of sulfide oxidation and methanotrophy to increase compared to the model with a constant temperature profile.

Once advection is implemented species available at the hydrothermal vent side are pushed further towards the seawater side resulting in a shift of the maximum rates of the different reactions towards the seawater side. Since the temperature also affects the rate of advection of heat (temperature), which results in an increase of temperature when compared to the non-advective case (see figure 10), the diffusion coefficients of the different species are increased further once advection is implemented, so on top of the regular effect of the advection there is an extra temperature effect resulting from this advection. Due to the increased availability of reduced species towards the seawater side, the oxygen consumption is increased, resulting in less diffusion of oxygen towards the hydrothermal vent side. Once advection is included in the model, oxygen is present at distances between ~2.5 and 3.0 cm, mainly due to sulfide and methane oxidation. Both sulfide and methane are pushed further towards the seawater side due to advection resulting in a smaller area of oxygen consumption when compared to the situation

where advection is excluded. Again, rates of the Knallgas reaction are negligible when compared to other reactions and therefore not plotted.

Overall, the oxidative reactions take place at the seawater side at distances between ~2.3 and 3.0 cm for the model excluding advection. This distance shifts towards ~2.65 to 3.0 cm once advection is taken into account. Oxygen diffuses slower in the direction of the hydrothermal vent side because its diffusion coefficient is low due to the low temperatures at the seawater side. Therefore, oxygen consuming reactions are always limited by the availability of oxygen.
The reductive reactions occur throughout the profile, for both the advective model as well as the non-advective model. This is the result of the availability of H_2 throughout the profile. The availability of all reduced species is increased due to faster diffusion as a result of the increased diffusion coefficients due to the high temperatures as the hydrothermal vent side. The anoxic oxidation of methane also affects the concentration profiles to great extent and the rate is limited by the lack of methane at the seawater side of the vent. At the hydrothermal vent side it is limited by less availability of sulfate. This availability of sulfate is also the cause of the shift in the maximum rate of AOM once advection is considered.

The implementation of a temperature gradient affects on mineral stability. The saturation indices are changed as a result from changes in the concentration gradients of the species considered in mineral precipitation reactions. These changes in the concentration gradients are the result from the temperature dependency of the diffusion coefficients.
Furthermore, due to the extreme temperature gradient, the mineral equilibrium constant will change throughout the vent. This will add an extra effect on the stability of the minerals, i.e. the saturation index. Changes in the mineral equilibrium constants have been calculated using the OBIGT software.
Calculation of the saturation indices shows that, except for galena and pyrrhotite, all minerals will precipitate throughout the entire vent. Galena has positive SI values between 0.55 and 3.0 cm. Pyrrhotite has a positive SI index between 0 and 1.44 cm and between 2.85 and 3.0 cm.

4.5 Diffusion, advection & reaction model (temperature gradient), including F_T

The next step is to incorporate the thermodynamic potential factor F_T in the model, which will only affect the reaction rate. Diffusion and advection are only affected indirectly if there would be a change in the species concentration due to changes in the reaction rates. As stated in the model set-up, F_T will have a value between 0 and 1, depending on the temperature and on the concentration of the species necessary for the corresponding microbial reaction. If the thermodynamic potential factor equals 1, there is no thermodynamic limitation on the reaction rate and the reaction rate will be bimolecular. Once the potential factor is smaller than 1, the reaction rate will decrease due to thermodynamic limitations. If F_T is zero, the reaction does not proceed as a result of the thermodynamic limitations.

The model ran for 0.1 yr, with time steps of 10^{-7} years. Again, an initial input file for each file is implemented which describes the species as a straight line between both boundary conditions. For temperature, the initial conditions are implemented in an input file as well, but the steady state conditions from the previous model including advection (figure 9) were used instead of a straight line between the boundary conditions.

The steady state concentrations of the different species are plotted in figure 14, the reaction rates of the individual reactions are plotted in figure 15, the production/consumption of the different species are plotted in figure 16.
In general, reaction are subjected to thermodynamic limitations on the hydrothermal vent side as a result of the high temperatures. Comparing the results from this model (figure 14 to 16) with results from the model without thermodynamic limitations (figure 10 to 12), there are only a few characteristics that stand out.
The most obvious feature is the rate of the AOM reaction, which is zero between a distance of 0 and ~0.55 cm once F_T is included in the model. This means that anoxic oxidation of methane is inhibited due to the thermodynamics of the reaction. This affects the production profiles of CH_4, SO_4^{2-}, HS^- and CO_2, which can be seen in figure 16, where there is no HS^- production and SO_4^{2-} and HCO_3^- consumption. The methane production profile is also altered because CH_4 is only produced by methanogenesis but not consumed by AOM between distances of 0 and ~0.55 cm.
The absence of any microbial reaction on the hydrothermal vent side in this model is in accordance with what is seen in actual hydrothermal vents. Because of the high temperatures, redox reactions are in equilibrium and can proceed abiological. Also, the upper temperature found for life thus far is 121°C (Kashefi and Lovley 2003), so the AOM reaction after 0.55 cm would not occur since the temperature is 270°C at that point, which is far above the upper temperature for life.

The likelihood that a mineral will precipitate has been calculated using the saturation index stated in equation 63. The calculations show that when diffusion, advection, reaction including a temperature gradient and the thermodynamic potential factor are implemented, all minerals, with the exception of galena and pyrrhotite, will precipitate throughout the entire distance of the hydrothermal vent. Galena will only precipitate between 0.60 cm and 3.0 cm while pyrrhotite will precipitate between 0 and 1.42 cm and again between 2.86 and 3.00 cm. The predictions are comparable to the calculations of the previous model since F_T does not affect species concentrations used in the calculations of the saturation index enough to change the saturation indices significantly.

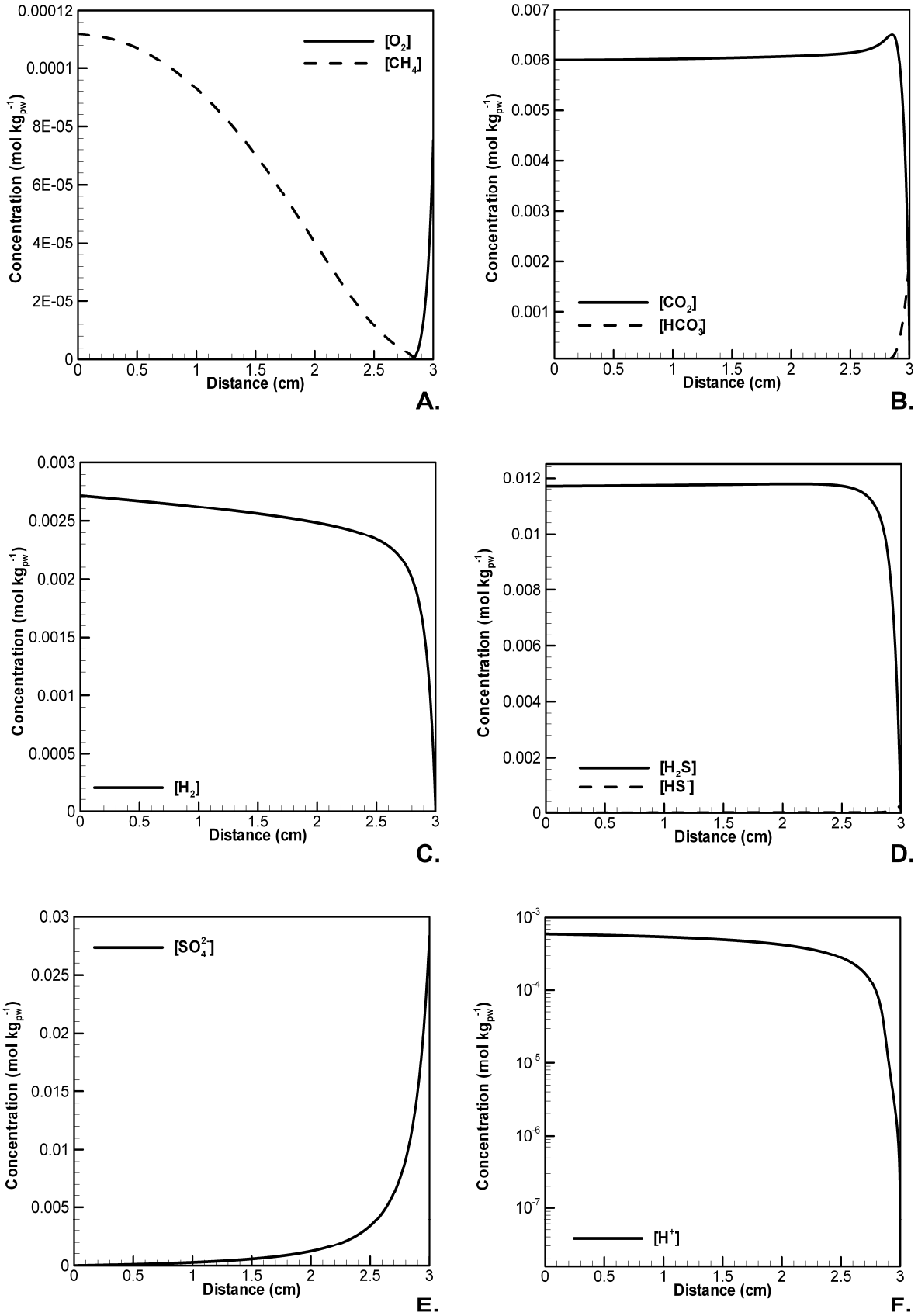

Figure 14: *Steady state concentrations of the species included in the model. The total model time was 0.2 years. Distance represents the distance from the vent with 0 being the hydrothermal fluid side and 3 being the seawater side. Concentrations at the boundaries are assumed to be those of seawater and 21°N EPR hydrothermal fluid). The concentration is given in mol per kilogram of porewater (mol kg_{pw}^{-1}). The scales on the y-axes are different.*

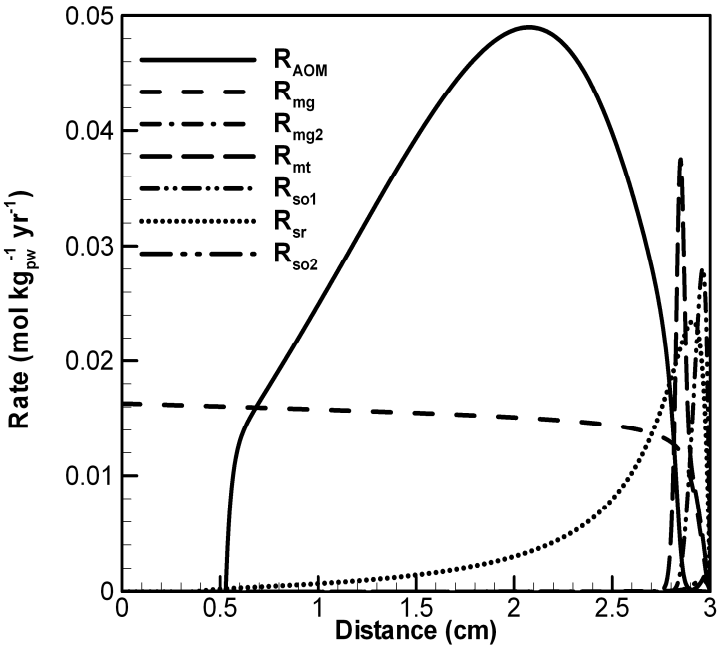

Figure 15*: Reaction rates of the individual reaction. R_{AOM} denotes the reaction rate for anoxic oxidation of methane, R_{mg} denotes the reaction rate of methanogenesis by means of CO_2 reduction, R_{mg2} denotes the reaction rate for methanogenesis by HCO_3^- reduction. The subscribt mt stands for methanotrophy, so1 for H_2S oxidation, so2 for HS^- oxidation. R_{sr} denotes the reaction rate of sulfate reduction.*

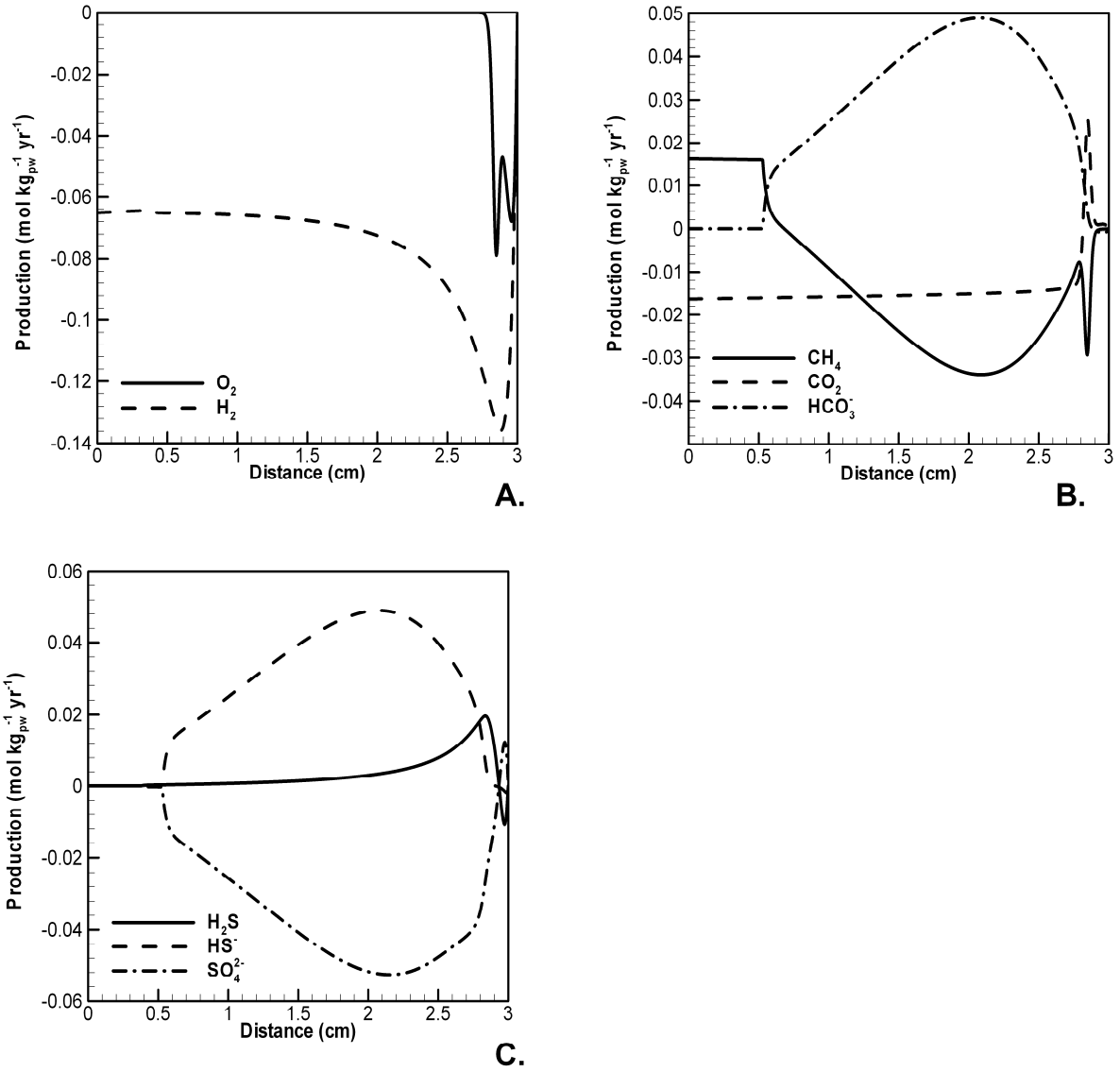

Figure 16: *Production of the different species as a function of distance with 0 being the hydrothermal vent side and 3 being the seawater side.* **A)** *Consumption (i.e. negative production) of O_2 and H_2* **B)** *Production and consumption of CH_4, CO_2 and HCO_3^-* **C)** *Production and consumption of H_2S, HS^- and sulfate.*

The effect of the different parameters on the type of microbial metabolism expected to be found in a hydrothermal vent is summarized in figure 17, which gives a qualitative description of the microbiology of the vents modeled. Once the reaction rate of a specific metabolic reaction was larger that 1 µM kg_{pw}^{-1} yr^{-1}, it is assumed that microbes using this type of metabolism are present in the hydrothermal vent. A rate of 1 µM kg_{pw}^{-1} yr^{-1} is very low, and is the result of a low concentration of one or both of the chemical species that defines the bimolecular rate laws. But bacteria and archaea are able to survive on very low concentrations of a chemical species needed for metabolism, although growth is limited (Baross 1995). Therefore, it is assumed that, even at very low reaction rates, microbes performing a specific metabolism are present.

Other assumptions made to construct figure 17 are that the upper temperature of life is 150°C, thus the dotted lines represent the model outcome, meaning that the reaction rate is larger that 1 µmol kg_{pw}^{-1} yr^{-1}, but because the temperature is above 150°C, no microbes will be present

For methanogenesis and sulfate reduction several bacteria (epsilonproteobacteria, gammaproteobacteria, themodesulfobacteria, Aquificae) and Archaea (Thermoprotei, methanococci, methanopyri) have been isolated (Nakagawa and Takai 2008).
For the anoxic oxidation of methane (AOM) no specific bacteria or archaea have been isolated but it is believed that the AOM reaction is mediated by a consortium of methane-consuming archaea and sulphate-reducing proteobacteria (Thauer and Shima 2006). It is believed that the bacteria and archaea involved in methanogenesis and sulfate reduction and the bacteria and archaea expected to use the AOM reaction pathway are strictly anaerobic, which means that these reactions are inhibited due to the presence of oxygen. This inhibition to oxygen is not included in our model. As can be seen from figure 17, the metabolic reactions for methanogenesis, AOM and sulfate oxidation occur also under oxic conditions. Therefore, these metabolism under oxic conditions are also represented by a dotted line, which means these reaction metabolisms are inhibited in the oxic zone but would be present according to the outcome of the model.

Implementation of advection, a temperature dependent diffusion coefficient (and a temperature gradient) and the thermodynamic potential factor all account for changes in the types of metabolism present in the vent. Advection decreases the presence of methanotrophs and sulfide oxidizers. The model including a temperature gradient and a temperature dependent diffusion coefficient decreases the presence of methanothrophs and sulfide oxidizers even further. Sulfide oxidizers are in this model only present between 2.7 and 3.0 cm while methanotrophs are present between 2.5 and 3.0 cm. Sulfate reducers, methanogens and archaeal and bacterial consortia that use the AOM pathway are present throughout the vent according to the model outcome. But assuming that no microbes survive above temperature of 150°C and that strict anaerobes do not survive in an oxic environment ($[O_2]>1\mu m\ kg_{pw}^{-1}$), all three types of microbes will only be present between 1.9 and 2.8 cm from the hydrothermal vent. Introduction of thermodynamic limitations, decreases the presence of sulfate reducers on the hydrothermal vent side and consortia using the AOM pathway on both the hydrothermal vent side and the seawater side. Methanotrophs are now only present between 2.8 and 3.0 cm from the hydrothermal vent, i.e. next to the seawater side.
Figure 17 shows that introduction of advection, temperature-dependent diffusion and a thermodynamic potential factor decreases the width of the oxic zone and therefore the presence of microbes using oxygen as an oxidation (methanotrophs and sulfide oxidizers). Once the thermodynamics of a metabolic reaction are taken into account, the presence of microbes using metabolisms that do not use oxygen as an oxidizer are altered.

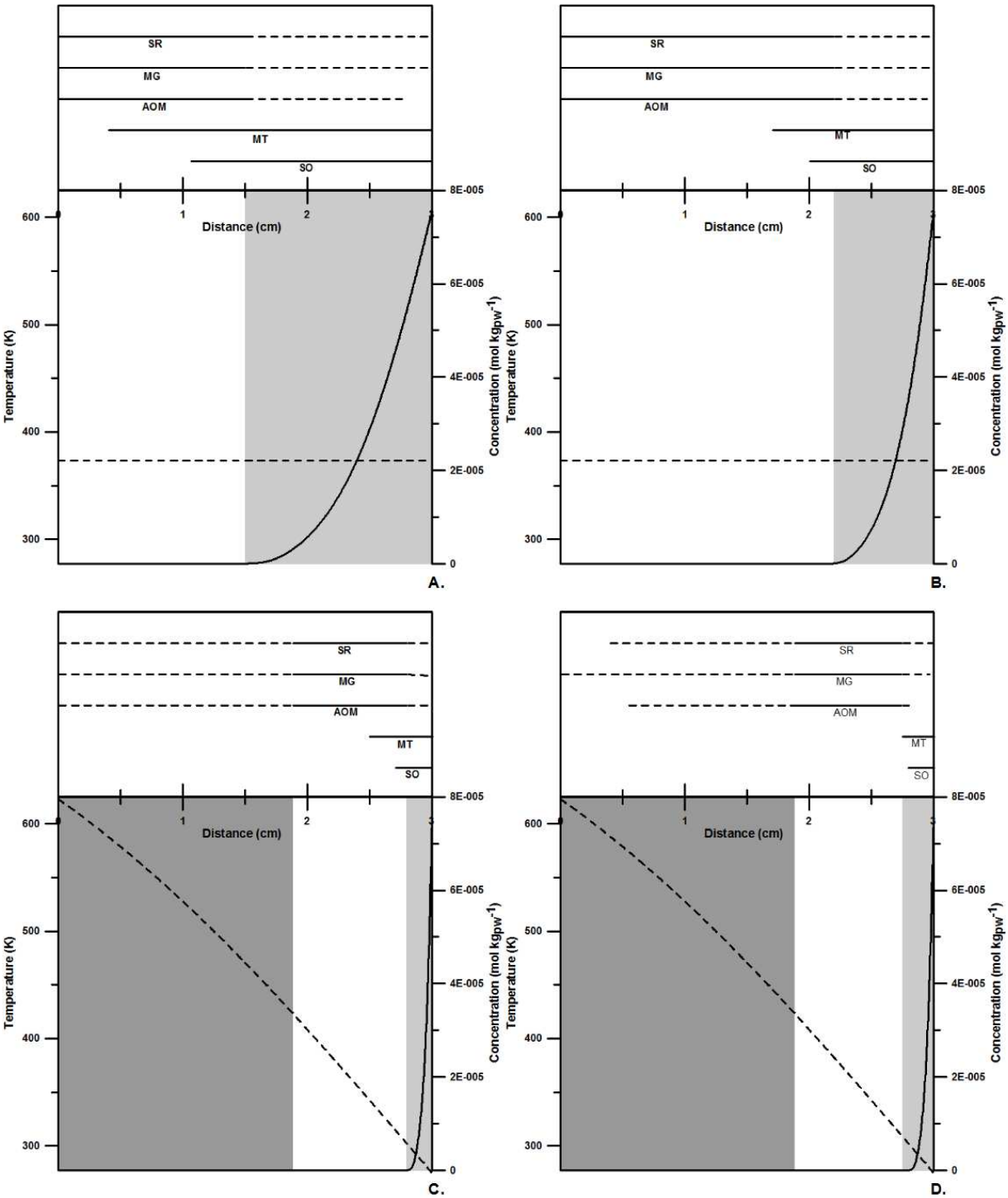

Figure 17: *Qualitative analysis of the different microbial mechanisms present in the different models. Once the rate of a type of metabolism was larger than 1 µmol kg^{-1} yr^{-1}, it is assumed that autotrophs using that metabolism will be present. A dotted line in the upper part of each graph means that according to the model outcome, the metabolic reaction would take place but in real life systems they are inhibited by either temperatures above 150 °C or the microorganisms known to a specific metabolism are strictly anaerobic and would not appear in an oxic zone. A straight black line in the upper parts of each graph shows the metabolisms are present according to the model and not inhibited by high temperatures or oxygen. SR=sulfate reducers, MG=methanogens, AOM=archaeal and bacterial consortia using anoxic oxidation of methane, MT=methanotrophs and SO=sulfide oxidizers. The dotted line in the lower parts of graphs A to D denotes temperature as a function of the distance from the hydrothermal vent, with 0 being the hydrothermal vent side and 3 being the seawater side. The solid line in the lower parts of graphs A to D represents the concentration of oxygen as a function of distance from the hydrothermal vent. The dark grey areas indicate the area were T>150ºC, the light grey areas shows the oxic zone ([O_2>1 µM).* ***A)*** *Model including only diffusion and reaction.* ***B)*** *Model including diffusion, advection and reaction* ***C)*** *Model including diffusion, advection and reaction (temperature gradient).* ***D)*** *Model including diffusion, advection and reaction (temperature gradient) and a thermodynamic potential factor F_T.*

4.6 Changes in the reaction rate constants

To investigate the sensitivity of the model towards the reaction rate constant, the model ran four times with a different set of values for the reaction rate constants. The rate constants used for the different runs can be found in table 5.
The outcome of the different runs is qualitatively described in figure 18, whenever the rate of a metabolic reaction was larger that 1 µmol kg^{-1} yr^{-1}, it is assumed that microbes using energy released by that reaction will be able to reside there.
Figure 18 shows that the change in the reaction rate constant has a profound effect on the microbial distribution in the hydrothemal vent. The differences are mainly the result from differences in the width of the oxic zone. The more oxygen diffused toward the hydrothermal vent side, the more methanotrophs and sulfide oxidizers are present.
The changes in the reaction rates due to changes in the rate constants alter the oxygen concentration throughout the hydrothermal vent which in turn alters the type of microbes present. The further oxygen moves inwards towards the hydrothermal vent side, i.e. the wider the oxic zone becomes, the further inward sulfide oxidizing and methane oxidizing microbes are present. An increase in the oxygen concentration results in an increase in the rate of reaction of reactions that use oxygen as an oxidizer, this is because the rate of reaction is second-order dependent on the concentration of oxygen.

Calculation of the saturation indices of the different minerals considered for each runs shows the same pattern as seen in previous models; all mineral will precipitate between the hydrothermal vent side and the seawater with the exception being galena and pyrrhotite. The only concentration changes affecting the saturation indices of the different minerals are the concentrations of H_2, SO_4^{2-}, H_2S and H^+, while the concentration gradients of Ba^{2+}, Ca^{2+}, Fe^{2+}, Cu^+, Pb^{2+} and Zn^{2+} remain constant, as does the mineral equilibrium constant. Therefore, not much change in the saturation indices of the different minerals in the different runs is seen.

Rate constant	Run 1	Run 2	Run 3	Run 4
k_{mt}	$10 \cdot 10^{10}$*	10^6	10^8	10^6
k_{mg}	10^3	10^6	10^3	10^6
k_{mg2}	10^3	10^6	10^6	10^6
k_{so1}	$1.6 \cdot 10^5$*	10^6	10^3	$1.6 \cdot 10^5$
k_{so2}	$1.6 \cdot 10^5$*	10^6	10^6	$1.6 \cdot 10^5$
k_{sr}	10^3	10^6	10^8	10^5
k_{aom}	10^6*	10^6	10^8	10^4

Table 5: *Values used for the different runs of the diffusion and reaction model. The values from the first run are the actual values for the rate constants as found in literature. *Values from van Cappellen and Wang (1996).*

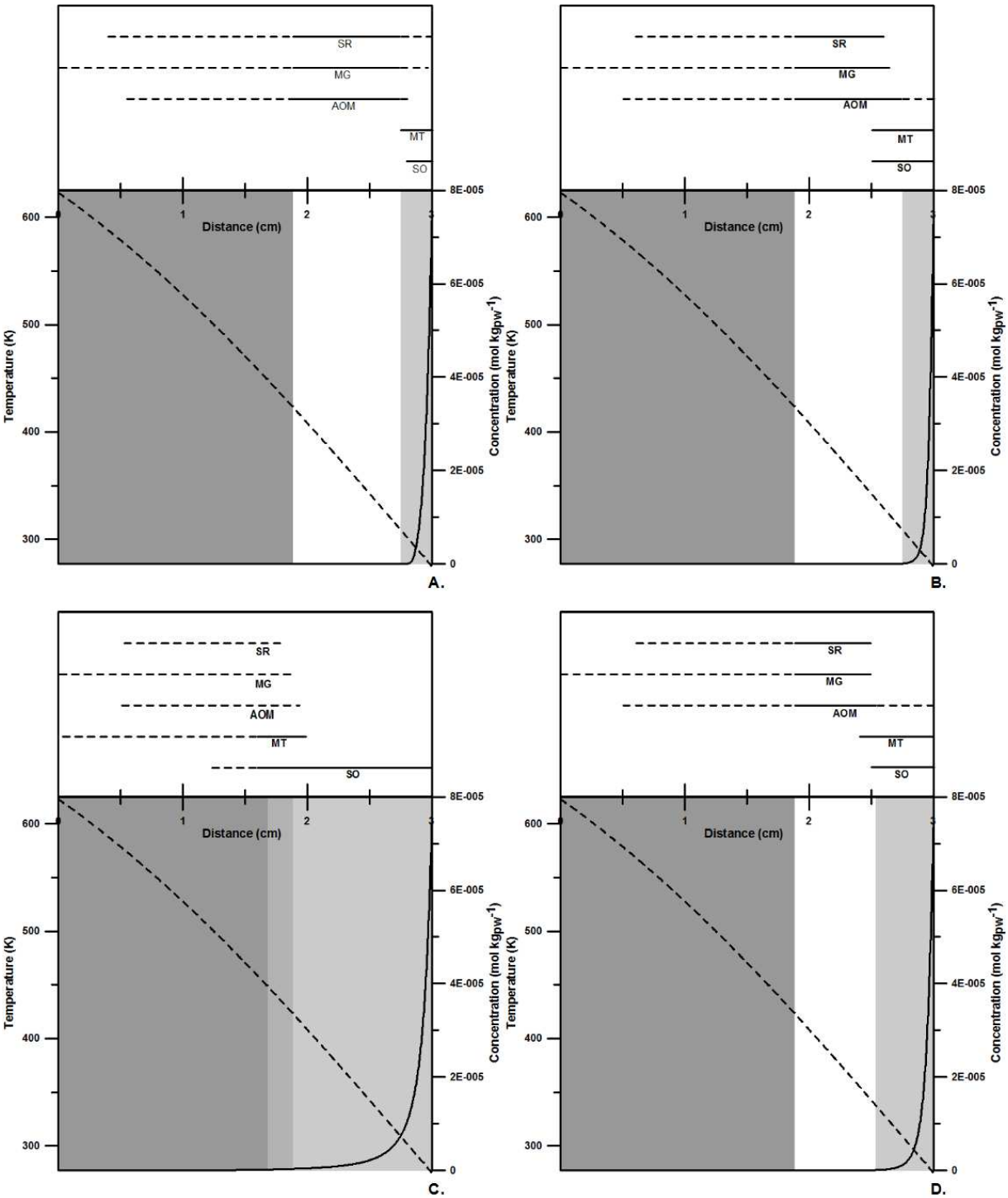

Figuur 28: *Qualitative analysis of the different runs. Once the rate of the metabolic reaction was larger than 1 µmol kg^{-1} yr^{-1}it is assumed that microbes using that type of metabolic pathway are present. A dotted line in the upper part of each graph implies that according to the model outcome, the metabolic reaction would take place, but in real life would not proceed because either the temperature exceeds the upper temperature of life (left side dotted lines) or the microorganisms known to use a specific metabolism are strictly anaerobic (right side dotted lines). A straight line means that at these distances microbes related to the specific metabolism are expected to be present. SR=sulfate reduction, MG=methanogenesis, AOM=anoxic oxidation of methane, MT=methanotrophy and SO=sulfide oxidation. The dotted lines in the lower part of each graph denotes the temperature as a function of the distance. The solid line represents the concentration of oxygen as a function of the distance from the hydrothermal vent. The dark grey area is the area where temperature exceeds 150ºC, the light grey area shows the oxic area of the hydrothermal vent ($[O_2]>1\mu M$). **A)** The microbial distribution for run 1 **B)** The microbial distribution with k-values from run 2 **C)**Run 3 **D)** Run 4. The k-values for the different runs are shown in table 5.*

4.7 The activity coefficient

Due to the level of difficulty of the model, the lack of knowledge of the author and the lack of time it was not possible to include the activity coefficient in the model.
The outcome from the mineral stability calculations according to equation 63 showed that, with the exception of galena and pyrrhotite, all minerals would precipitate over the entire distance, i.e. the saturation index was larger than zero for the model including diffusion, advection, reaction (temperature gradient) and a thermodynamic potential factor. In sampled hydrothermal vents, all of these minerals are found, but not throughout the entire width of the hydrothermal vent. The activity coefficient will alter the saturation index and thus the likelihood of a mineral to precipitate since all electrolyte concentrations are changed due to the activity coefficient in a way that concentration does not equal activity anymore. Also, the direct implementation of the mineral precipitation and dissolution reactions would also improve the model. Tivey and McDuff (1990) implemented mineral precipitation and dissolution reactions and also managed to include the activity coefficient in their model for hydrothermal vent systems. They concluded that the activity coefficients have a profound effect on the activity of the different species involved in mineral precipitation and thus on the precipitation and stability of minerals. Tivey (1995) has done calculations of transport-controlled profiles and corresponding mineral saturation states and found that the outcome reproduced observed mineralogy at five different vent sides. Although the main parameter having an effect on the mineral distribution was temperature, the implementation of the activity coefficient had a profound effect on the concentration gradients of species implemented and the mineralogy (Tivey 1995).
To increase understanding in the interaction between hydrothermal fluids, rocks and microbes, it is important that factors controlling the composition of hydrothermal fluids, minerals present or the type of microbes present are accurately modeled. Therefore, it is suggested that if this model is being expanded, the activity coefficients are added as described in the model set-up.
There are no data available on the effect of the activity coefficients on metabolic reactions that might be present in hydrothermal vent systems. The introduction of the activity coefficients does not affect concentration gradients of non-electrolyte species but will only affect electrolyte species. Tivey and McDuff (1990) showed that the concentration gradient for SO_4^{2-} does not change significantly once the activity coefficient is added. Therefore, the only species used by microbes that directly affected by the activity coefficient are H^+, HCO_3^-, CO_3^{2-}, HS^- and OH^-. Since the concentrations HCO_3^-, CO_3^{2-}, HS^- and OH^- are all dependent on the pH, changes in the activity of H^+ affects all other concentrations, except O_2 and H_2, via the equilibrium reaction (see reaction 45. 46 and 52).

5. Conclusions and further recommendations

Except for the Knallgas reaction, all microbial pathways modeled have a reaction rate which means that there is a thermodynamic drive and no kinetic inhibition for these reactions to occur. Methanotrophs, methanogens, sulfate reducers and sulfide oxidizers are found in several hydrothermal vent sites (Nakagawa and Takai 2008) under the conditions modeled (temperature and boundary conditions) (Tivey and McDuff 1990). Although the model does not include all parameters known to have an effect on chemical concentrations and temperature, it still holds some validity. Sulfate reducers and methanogens are the most dominant metabolism present which has also been predicted by McCollum and Shock (1998) and their mixing model assessing the Gibbs free energy of metabolic reaction pathways. There is no physical evidence available for the use of the AOM pathway by microbes, but according to our model outcome, this pathway is just as useful as sulfate reduction or methanogenesis.
The most important parameter affecting the types of microbial metabolisms present is the temperature gradient. Also, changes in the reaction rate constant can have a very large effect on microbial species distribution.

The calculation of the mineral saturation states with the model outcome does not reproduce or even resembles the mineralogy found in hydrothermal vent systems and therefore, mineral formation reactions need to be added into the model to gain more insight into rock-water-fluid interactions. Mineral deposition gives rise to changes in the physical environment within chimney walls, leading to a well-defined sequence of mineralogical and chemical transformations (Tivey and McDuff 1990).

Besides the parameters described and added in this model, there are much more parameters that can be added or altered to gain more insight into processes and interactions present at hydrothermal vents. However, the modeling microbial dynamics is limited by our understanding of the interactions between functionally diverse groups of (micro)organisms (Nakagawa and Takai 2008). In this model, no threshold values for O_2 or H_2 were taken into account, no symbiosis between organisms is assumed and no inhibition values for different chemical species have been modeled. Competitive and cooperative behaviors among different microorganisms are not considered even though they might play a substantial role, especially when considering the anoxic oxidation of methane. Patterns in chemoautotrophic microbial community structures and activities should be microbially clarified in more detail in various deep-sea vent environments and should be integrated into geochemical thermodynamic modeling (Nakagawa and Takai 2008).
Usually, the Michaelis-Menten reaction path is used for calculation of the rate of microbial metabolism, this is not done because kinetic parameters of energy metabolisms in a variety of chemoautotrophs are as yet unknown (Nakagawa and Takai 2008), this includes kinetic parameters for the metabolisms used in this model.
Besides the microbial reaction pathways modeled here, there are more reaction pathways available for chemoautotrophs. Acetate, nitrogen and metals such as iron are also known to be used by microbes and these microbes have also been found in hydrothermal vent chimneys (Nakagawa and Takai 2008).

The physical environment can also be altered to gain more insight in hydrothermal vents. Advection of hydrothermal vent water at the hydrothermal vent side is taken into account but there is also advection of seawater inward from the seawater side. Advection of seawater inward does occur in observed hydrothermal vents and will affect the model outcome (Tivey and McDuff 1990).
Furthermore, a constant porosity of 0.3 is assumed. In hydrothermal vent systems, precipitation and dissolution of minerals and growth of microbes onto minerals will alter the porosity. Since

mineral precipitation and dissolution changes in time, porosity will also change in time. A coupling between mineral precipitation and dissolution, biomass growth and decay and porosity would improve the physical environment of the modeled hydrothermal vent.
Besides porosity, also tortuosity plays a role in the transport of mass (Tivey and McDuff 1990) and can be implemented in a future model.

Once a 1D model for hydrothermal vents is developed that is capable of accurately reproducing mineral composition, microbial composition and fluid composition observed in nature, one can start changing the boundary conditions into ancient compositions of seawater and hydrothermal vent fluids to see which metabolisms might have originated in ancient hydrothermal vents.

6. Acknowledgements

I would like to thank Pierre Regnier for being my supervisor, Doug LaRowe for helping me start up the project. Much thanks to David Aguilera for his great help and patience with the modeling. Furthermore, I would like to thank my friends and family for all their support and advice, especially the ones who also had to write a thesis.

7. References

Aguilera D.R., Jourabchi P., et al. (2005). "A knowledge-based reactive transport approach for the simulation of biogeochemical dynamics in Earth systems." Geochemistry Geophysics Geosystems **6**(7).

Alt-Epping, P. and L. W. Diamond (2008). "Reactive transport and numerical modeling of seafloor hydrothermal systems: A review." Geophysical Monograph Series **178**: 167-192.

Amend, P. J. and E. L. Shock (2001). "Energetics of overall metabolic reactions of thermophilic and hyperthermophilic archea and bacteria." FEMS Microbiology reviews **25**: 175-243.

Baross, J. A. (1995). Isolation, growth, and maintenance of hyperthermophiles. Plainview, N.Y., Cold Spring Harbor Laboratory Press.

Bethke, C. M. (2008). Geochemical and Biogeochemical Reaction Modeling. Cambridge, Cambridge University Press.

Boudreau, B. P., Ed. (1997). Diagenetic models and their implementation: modelling transport and reactions in aquatic sediments. New York, Springer.

Brailsford, A. D. and K. G. Major (1964). "The thermal conductivity of aggregate of several phases, including porous materials." British Journal of Applied Physics **15**: 313-319.

Clausen, C. and E. Huenges (1995). Thermal conductivity of rocks and minerals. Rock Physics and Phase Relations: A Handbook of Physical Constants, American Geophysical Union.

Crank, J., Ed. (1975). The mathematics of diffusion. Oxford, Oxford University Press.

Dale, A. W., P. Regnier, et al. (2006). "Bioenergetic controls on anearobic oxidation of methane (AOM) in coastal marine sediments: a theoretical analysis." American Journal of Science **306**: 246-294.

Hayduk, W. and H. Laudie (1974). "Prediction of diffusion coefficients for nonelectrolytes in dilute aqueous solutions." American Institute of Chemical Engineers Journal **20**: 611-615.

Helgeson, H. C. (1969). "Thermodynamics of hydrothermal systems at elevated temperatures and pressures." American Journal of Science **267**: 729-804.

Holm, N. G. (1992). "Why are hydrothermal systems proposed as plausible environments for the origin of life?" Origins of Life and Evolution of Biospheres **22**(1-4): 5-14.

Huber, J. A. and J. F. Holden (2008). "Modeling the impact of diffuse vent microorganisms along mid-ocean ridges and flanks." Geophysical Monograph Series **178**(Mag).

Jin, Q. and C. M. Bethke (2002). "Kinetics of electron transfer through the respiratory chain." Biophysical Journal **83**: 1797-1808.

Jin, Q. and C. M. Bethke (2005). "Predicting the rate of microbial respiration in geochemical environments." Geochimica et Cosmochimica Acta **69**(5): 1133-1143.

Jin, Q. and C. M. Bethke (2007). "The thermodynamics and kinetics of microbial metabolism." American Journal of Science **307**: 643-677.

Johnson, J. W., E. H. Oelkers, et al. (1992). "SUPCRT92: A software package for calculating the standard molal thermodynamic properties of minerals, gases, aqueous species, and reactions from 1 to 5000 bar and 0 to 1000°C." Computers & Geosciences **18**(7): 899-947

Karl, D. M., C. O. Wirsen, et al. (1980). "Deep-sea primary production at the Galapagos hydrothermal vents. ." Science **207**: 1345-1347.

Kashefi, K. and D. R. Lovley (2003). "Extending the upper temperature limit for life." Science **301**(5635): 934.

Li, J. H. and S. Gregory (1974). "Diffusion of ions in sea water and in deep-sea sediments " Geochimica et Cosmochimica Acta **38**(5): 703-714.

Lowell, R. P., J. S. Seewald, et al. (2008). "Modeling hydrothermal processes at ocean spreading centers: Magma to microbe - An overview." Geophysical Monograph Series **178**: 1-15.

Lutz, R. A. and M. J. Kennish (1993). "Ecology of hydrothermal vent communities: a review." Reviews of geophysics **31**(3): 211-242.
Marcus, Y. (1994). "A simple empirical model describing the thermodynamics of hydration of ions of widely varying charges, sizes, and shapes." Biophysical Chemistry **51**: 111-127.
McCollum, M. and E. L. Shock (1998). "Fluid-rock interactions in the lower oceanic crust: thermodynamic models of hydrothermal alteration." Journal of Geophysical Research **103**: 547-575.
McCollum, T. M. and P. J. Amend (2005). "A thermodynamic assessment of energy requirements for biomass synthesis by chemolithoautotrophic micro-organisms in oxic and anoxic environments." Geobiology **3**: 135-144.
McCollum, T. M. and E. L. Shock (1997). "Geochemical constraints on chemolithoautotrophic metabolism by microorganisms in seafloor hydrothermal systems." Geochimica et Cosmochimica Acta **61**(20): 4375-4391.
McDuff, R. E. and J. M. Gieskes (1976). "Calcium and magnesium profiles in DSDP interstitial waters: Diffusion or reaction?" Earth and Planetary Science Letters **33**(1): 1-10.
Nakagawa, S. and K. Takai (2008). "Deep-sea vent chemoautotrophs: diversity, biochemistry and ecological significance." FEMS Microbiology Ecology **65**: 1-14.
Oelkers, E. H. and H. C. Helgeson (1988). "Calculation of the thermodynamic and transport properties of aqueous species at high pressures and temperatures: aqueous tracer diffusion coefficients of ions to 1000 C and 5 kb." Geochimica et Cosmochimica Acta **52**: 63-85.
Pitzer, K. S. (1991). Activity coefficients in electrolyte solutions 2nd edition. Boston.
Regnier, P., J. P. O'Kane, et al. (2002). "Modeling complex multi-component reactive-transport systems: towards a simulation environment based on the concept of a knowledge base." Applied Mathematical Modelling **26**: 913-927.
Ribeiro, A. C. F., M. A. Esterso, et al. (2006). "Mean distance of closest approach of ions: Sodium salts in aqueous solutions." Journal of Molecular Liquids **218**(128): 134-139.
Rieger, P. H. (1994). Electrochemistry.
Robinson, R. A. and R. H. Stokes (1965). Electrolyte solutions. London, Buttersworth.
Roychoudhury, A. N. (2004). "Sulfide respiration in extreme environments: A kinetic study." Geomicrobiology Journal **21**(1): 33-43.
Sass, J. H., A. H. Lachenbruch, et al. (1992). "Heat flow from a scientific research well at Cajon pass, California." Journal of Geophysical Research **97**(B4): 2017-5030.
Schrenk, M. O., J. F. Holden, et al. (2008). "Magma-To-Microbe networks in the context of sulfide hosted microbial ecosystems." Geophysical Monograph Series **178**.
Sedlbauer, J. and V. Majer (2000). "Data and models for calculating the standard thermodynamic properties of aqueous non-electrolyte solutes under hydrothermal conditions." European Journal of Mineralogy **12**: 1109-1122.
Sengers, J. V. and J. T. R. Watson (1986). "Improved international formulations for the viscosity and thermal conductivity of water substances." Journal of Physical and Chemical Reference Data **15**(4): 1291-1314.
Shock, E. L. (1992). "Chemical environments of submarine hydrothermal systems." Origins of life and evolution of the biosphere **22**: 67-107.
Shock, E. L., T. M. McCollum, et al. (1993). "Geochemical constraints on chemolithoautotrophic reactions in hydrothermal systems." Origins of Life and Evolution of Biospheres **25**(1-3): 141-159.
Somerton, W. H. (1992). Thermal properties and temperature-related behavior of rock/fluid systems. Amsterdam, Elsevier.
Takai, K., T. Komatsu, et al. (2001). "Distribution of archaea in a black smoker chimney structure." Applied and Environmental Microbiology **67**(8): 3618-3629.
Thauer, R. K. and S. Shima (2006). "Methane and Microbes." Nature **440**: 878-879.

Tivey, M. K. (1995). "The influence of hydrothermal fluid composition and advection rates on black smoker chimney mineralogy: insights from modeling transport and reaction." Geochimica et Cosmochimica Acta **59**(10): 1933-1949.

Tivey, M. K. and R. E. McDuff (1990). "Mineral precipitation in the walls of black smoker chimneys: A quantitative model of transport and chemical reaction." Journal of Geophysical Research **95**(B8): 12, 617-612,637.

van Cappellen, P. and Y. Wang (1996). "Cycling of iron and manganes in surface sediments: A general theory for the coupled transport and reaction of carbon, oxygen, nitrogen, sulfur, iron and manganese." American Journal of Science **296**: 197-243.

Walther, J. V. (1997). "Determination of activity coefficients of neutral species in supercritical H_20 solutions " Geochimica et Cosmochimica Acta **61**(16): 3311-3318.

Waples, D. W. and J. S. Waples (2004). "A review and evaluation of specific heat capacities of rocks, minerals, and subsurface fluids. Part 1: minerals and nonporous rocks." Natural Resources Research **13**(2): 97-122.

Waples, D. W. and J. S. Waples (2004). "A review and evaluation of specific heat capacities of rocks, minerals, and subsurface fluids. Part 2: fluids and porous rocks." Natural Resources Research **13**(2): 123-130.

Wilke, C. R. and P. Chang (1955). "Correlation of diffusion coefficients in dilute solutions." American Institute of Chemical Engineers Journal **1**: 264-270.

Yusufova, V. D., R. I. Pepinov, et al. (1978). "Thermophysical properties of softened seawater and salt solution over a wide temperature and pressure range." Desalination **25**: 269-280.

Zhu, W., M. K. Tivey, et al. (2007). "Permeability-porosity relationships in seafloor vent deposits: Dependence on pore evolution processes." Journal of Geophysical Research **112**: 1-15.

Appendix 1

Microbial redox reaction	**Stoichiometry**	**Rate law**
Anoxic oxidation of methane (AOM)	$CH_4 + SO_4^{2-} \rightarrow HS^- + HCO_3^- + H_2O$	$R_{AOM} = k_{AOM}[CH_4][SO_4^{2-}]$
Sulfate reduction	$SO_4^{2-} + 4H_2 + 2H^+ \rightarrow H_2S + 4H_2O$	$R_{sr} = k_{sr}[SO_4^{2-}][H_2]$
Methanogenesis	$CO_2 + 4H_2 \rightarrow CH_4 + 2H_2O$	$R_{mg1} = k_{mg1}[CO_2][H_2]$
	$HCO_3^- + 4H_2 + H^+ \rightarrow CH_4 + 3H_2O$	$R_{mg2} = k_{mg2}[HCO_3^-][H_2]$
Sulfide oxidation	$H_2S + 2O_2 \rightarrow SO_4^{2-} + 2H^+$	$R_{so1} = k_{so1}[H_2S][O_2]$
	$HS^- + 2O_2 \rightarrow SO_4^{2-} + H^+$	$R_{so2} = k_{so2}[HS^-][O_2]$
Methane oxidation	$CH_4 + 2O_2 \rightarrow CO_2 + 2H_2O$	$R_{mg} = k_{mg}[CH_4][O_2]$
Knallgas reaction	$H_2 + 0.5O_2 \rightarrow H_2O$	$R_{kn} = k_{kn}[H_2][O_2]$
Equilibrium reaction	**Stoichometry**	**Equilibrium constant**
Carbonic acid dissociation	$H_2CO_3 \leftrightarrow HCO_3^- + H^+$	$K_1 = \frac{[HCO_3^-][H^+]}{[H_2CO_3]}$
Bicarbonate dissociation	$HCO_3^- \leftrightarrow CO_3^{2-} + H^+$	$K_2 = \frac{[CO_3^{2-}][H^+]}{[HCO_3^-]}$
Sulfide dissociation	$H_2S \leftrightarrow HS^- + H^+$	$K_s = \frac{[HS^-][H^+]}{[H_2S]}$
Water dissociation	$H_2O \leftrightarrow H^+ + OH^-$	$K_w = [H^+][OH^-]$
Mineral formation reaction	**Stoichiometry**	**Rate law**
Anhydrite formation	$Ca^{2+} + SO_4^{2-} \leftrightarrow CaSO_4(s)$	$IAP_{an} = [Ca^{2+}][SO_4^{2-}]$
Barite formation	$Ba^{2+} + SO_4^{2-} \leftrightarrow BaSO_4(s)$	$IAP_{ba} = [Ba^{2+}][SO_4^{2-}]$
Chalcopyrite formation	$4H_2S + 2Fe^{2+} + 2Cu^+ \leftrightarrow 2CuFeS_2(s) + H_2 + 6H^+$	$IAP_{ch} = \frac{[Fe^{2+}]^2[Cu^+]^2}{[H_2][H^+]^6}$

Appendix 1 (continued)

Mineral formation reaction	Stoichiometry	IAP (Ionic Acitivity Product)
Covellite formation	$2Cu^{+} + 2H_2S \leftrightarrow 2CuS(s) + H_2 + 2H^{+}$	$IAP_{co} = \frac{[H_2S]^2[Cu^{2+}]^2}{[H_2][H^{+}]^2}$
Galena formation	$Pb^{2+} + H_2S \leftrightarrow PbS(s) + 2H^{+}$	$IAP_{ga} = \frac{[Pb^{2+}][H_2S]}{[H^{+}]^2}$
Pyrite formation	$2H_2S + Fe^{2+} \leftrightarrow FeS_2(s) + H_2 + 2H^{+}$	$IAP_{py} = \frac{[Fe^{2+}][H_2S]^2}{[H_2][H^{+}]^2}$
Pyrrhotite formation	$H_2S + Fe^{2+} \leftrightarrow FeS(s) + 2H^{+}$	$IAP_{FeS} = \frac{[Fe^{2+}][H_2S]}{[H^{+}]^2}$
Sphalerite formation	$H_2S + Zn^{2+} \leftrightarrow ZnS(s) + 2H^{+}$	$IAP_{sp} = \frac{[Zn^{2+}][H_2S]}{[H^{+}]^2}$
Wurzite formation	$H_2S + Zn^{2+} \leftrightarrow ZnS(s) + 2H^{+}$	$IAP_{wu} = \frac{[Zn^{2+}][H_2S]}{[H^{+}]^2}$

Appendix 2: *The different parameters used in the model and their values*

Parameter	Description	Value	Unit	Reference
V_{b,H_2}	Molar volume of H_2	28.5	$cm^3\ mol^{-1}$	Hayduk and Laudie (1974)
V_{b,O_2}	Molar volume of O_2	27.9	$cm^3\ mol^{-1}$	Hayduk and Laudie (1974)
V_{b,CO_2}	Molar volume of CO_2	37.3	$cm^3\ mol^{-1}$	Hayduk and Laudie (1974)
V_{b,CH_4}	Molar volume of CH_4	37.7	$cm^3\ mol^{-1}$	Hayduk and Laudie (1974)
V_{b,H_2S}	Molar volume of H_2S	35.2	$cm^3\ mol^{-1}$	Hayduk and Laudie (1974)
r_{s,H^+}	Stokes' law radius of H^+	26	pm	Rieger (1994)
r_{s,HCO_3^-}	Stokes' law radius of HCO_3^-	226	pm	Marcus (1994)
r_{s,HS^-}	Stokes' law radius of HS^-	238	pm	Marcus (1994)
$r_{s,CO_3^{2-}}$	Stokes' law radius of CO_3^{2-}	254	pm	Marcus (1994)
r_{s,OH^-}	Stokes' law radius of OH^-	212	pm	Marcus (1994)
$r_{s,SO_4^{2-}}$	Stokes' law radius of SO_4^{2-}	231	pm	Rieger (1994)
$r_{s,Ba^{2+}}$	Stokes' law radius of Ba^{2+}	254	pm	Marcus (1994)
$r_{s,Ca^{2+}}$	Stokes' law radius of Ca^{2+}	271	pm	Marcus (1994)
r_{s,Cu^+}	Stokes' law radius of Cu^+	233	pm	Marcus (1994)
$r_{s,Fe^{2+}}$	Stokes' law radius of Fe^{2+}	291	pm	Marcus (1994)
$r_{s,Pb^{2+}}$	Stokes' law radius of Pb^{2+}	261	pm	Marcus (1994)
$r_{s,Zn^{2+}}$	Stokes' law radius of Zn^{2+}	295	pm	Marcus (1994)
$\alpha_\gamma^{H^+}$	The distance of closest approach for H^+	9	Å	Kielland (1937)
$\alpha_\gamma^{CO_3^{2-}}$	The distance of closest approach for CO_3^{2-}	4.5	Å	Kielland (1937)
$\alpha_\gamma^{HCO_3^-}$	The distance of closest approach for HCO_3^-	4	Å	Kielland (1937)

Appendix 2 (continued)

Parameter	Description	Value	Unit	Reference
$\alpha_{\gamma}^{HS^-}$	The distance of closest approach for HS^-	3.5	Å	Kielland (1937)
$\alpha_{\gamma}^{SO_4^{2-}}$	The distance of closest approach for SO_4^{2-}	4	Å	Kielland (1937)
$\alpha_{\gamma}^{Ba^{2+}}$	The distance of closest approach for Ba^{2+}	5	Å	Kielland (1937)
$\alpha_{\gamma}^{Ca^{2+}}$	The distance of closest approach for Ca^{2+}	6	Å	Kielland (1937)
$\alpha_{\gamma}^{Cu^{+}}$	The distance of closest approach for Cu^{+}		Å	Kielland (1937)
$\alpha_{\gamma}^{Fe^{2+}}$	The distance of closest approach for Fe^{2+}	6	Å	Kielland (1937)
$\alpha_{\gamma}^{Pb^{2+}}$	The distance of closest approach for Pb^{2+}	4.5	Å	Kielland (1937)
$\alpha_{\gamma}^{Zn^{2+}}$	The distance of closest approach for Zn^{2+}	6	Å	Kielland (1937)
D_{0,CH_4}	Tracer diffusion coefficient of CH_4	527.01192	$cm^2\ yr^{-1}$	Boudreau (1992)
D_{0,CO_2}	Tracer diffusion coefficient of CO_2	605.91	$cm^2\ yr$	Boudreau (1992)
D_{0,HCO_3^-}	Tracer diffusion coefficient of HCO_3^-	159.681456	$cm^2\ yr$	Boudreau (1992)
$D_{0,CO_3^{2-}}$	Tracer diffusion coefficient of CO_3^{2-}	136.64	$cm^2\ yr$	Boudreau (1992)
D_{0,O_2}	Tracer diffusion coefficient of O_2	722.66904	$cm^2\ yr$	Boudreau (1992)
D_{0,H_2}	Tracer diffusion coefficient of H_2	1388.5344	$cm^2\ yr$	Boudreau (1992)
D_{0,H_2S}	Tracer diffusion coefficient of H_2S	662.7096	$cm^2\ yr$	Boudreau (1992)
D_{0,HS^-}	Tracer diffusion coefficient of HS^-	328.1990	$cm^2\ yr$	Boudreau (1992)
$D_{0,SO_4^{2-}}$	Tracer diffusion coefficient of SO_4^{2-}	154.01088	$cm^2\ yr$	Boudreau (1992)
D_{0,H^+}	Tracer diffusion coefficient of H^+	1716.73344	$cm^2\ yr$	Boudreau (1992)
D_{0,OH^-}	Tracer diffusion coefficient of OH^-	817.11806	$cm^2\ yr$	Boudreau (1992)

Appendix 2 (continued)

Parameter	Description	Value	Unit	Reference
$D_{0,Ba^{2+}}$	Tracer diffusion coefficient of Ba^{2+}	128,1239	cm^2 yr	Boudreau (1992)
$D_{0,Ca^{2+}}$	Tracer diffusion coefficient of Ca^{2+}	113,6074	cm^2 yr	Boudreau (1992)
$D_{0,Cu^{+}}$	Tracer diffusion coefficient of Cu^{+}	106,9803	cm^2 yr	Boudreau (1992)
$D_{0,Fe^{2+}}$	Tracer diffusion coefficient of Fe^{2+}	104,4557	cm^2 yr	Boudreau (1992)
$D_{0,Pb^{2+}}$	Tracer diffusion coefficient of Pb^{2+}	140,7469	cm^2 yr	Boudreau (1992)
$D_{0,Zn^{2+}}$	Tracer diffusion coefficient of Zn^{2+}	104,4557	cm^2 yr	Boudreau (1992)
α_{CH_4}	Temperature dependency of the diffusion coefficient for CH_4	0.0	Dimensionless	Boudreau (1992)
α_{CO_2}	Temperature dependency of the diffusion coefficient for CO_2	0.0	Dimensionless	Boudreau (1992)
$\alpha_{HCO_3^-}$	Temperature dependency of the diffusion coefficient for HCO_3^-	0.054347826	Dimensionless	Boudreau (1992)
$\alpha_{CO_3^{2-}}$	Temperature dependency of the diffusion coefficient for CO_3^{2-}	0.04595843	Dimensionless	Boudreau (1992)
α_{O_2}	Temperature dependency of the diffusion coefficient for O_2	0.0	Dimensionless	Boudreau (1992)
α_{H_2}	Temperature dependency of the diffusion coefficient for H_2	0.0	Dimensionless	Boudreau (1992)
α_{H_2S}	Temperature dependency of the diffusion coefficient for H_2S	0.0	Dimensionless	Boudreau (1992)
α_{HS^-}	Temperature dependency of the diffusion coefficient for HS^-	0.02625	Dimensionless	Boudreau (1992)
$\alpha_{SO_4^{2-}}$	Temperature dependency of the diffusion coefficient for SO_4^{2-}	0.047540984	Dimensionless	Boudreau (1992)
α_{OH^-}	Temperature dependency of the diffusion coefficient for OH^-	0.042239	Dimensionless	Boudreau (1992)
α_{H^+}	Temperature dependency of the diffusion coefficient for H^+	0.028584559	Dimensionless	Boudreau (1992)
$\alpha_{Ba^{2+}}$	Temperature dependency of the diffusion coefficient for Ba^{2+}	0,04335	Dimensionless	Boudreau (1992)
$\alpha_{Ca^{2+}}$	Temperature dependency of the diffusion coefficient for Ca^{2+}	0,049722	Dimensionless	Boudreau (1992)
$\alpha_{Cu^{+}}$	Temperature dependency of the diffusion coefficient for Cu^{+}	0,046608	Dimensionless	Boudreau (1992)

Appendix 2 (continued)

Parameter	Description	Value	Unit	Reference
$\alpha_{Fe^{2+}}$	Temperature dependency of the diffusion coefficient for Fe^{2+}	0,045317	Dimensionless	Boudreau (1992)
$\alpha_{Pb^{2+}}$	Temperature dependency of the diffusion coefficient for Pb^{2+}	0,044395	Dimensionless	Boudreau (1992)
$\alpha_{Zn^{2+}}$	Temperature dependency of the diffusion coefficient for Zn^{2+}	0,045619	Dimensionless	Boudreau (1992)
e_0	Charge of an electron	$1.602*10^{-19}$	Coulomb	
N_A	Avagadro's number	$6.02214179*10^{23}$	mol^{-1}	
R	Gas constant	8.314472	$J\ K^{-1}\ mol^{-1}$	
k_b	Boltzmann's constant	$1.3806504*10^{-23}$	$J\ K^{-1}$	

Appendix 3: *The subroutines advdiffcoeff and transcoeff_MT have been changed manually because the web-distributed Knowledge-Based Reactive Transport Model (KBRTM) was not sufficient to model the termperature-dependent diffusion coefficient and temperature dependent advection.*

```
      subroutine advdiffcoeff()

      include 'common_geo.inc'
      include 'common.inc'

c**********************************************************************
! define your advection velocities and diffusion coefficients.       *
! advection and dispersion coefficients are defined at faces and nodes,*
! i.e. 1,2,...,nx  (the values @ nodes are only needed for the flux or *
! gradient boundary conditions)                                       *
! w acts on solids and solutes                                        *
! q acts only on solutes                                              *
! Dmol acts only on solutes (can be overwritten)                      *
! Disp acts only on solutes                                           *
! Db acts on solids and solutes                                       *
! depth can be referred to as x(j)                                    *
!                                                *
! disp is the total diffusion coefficient for a species k at face j   *
! vd is the advection velocity of a dissolved species at face j       *
! vp is the advection velocity of a solid species at face j           *
!                                                *
! CM, July 2002                                                       *
c**********************************************************************

      real*8 dsol,dmix,db,fac_sal,vq,lbd0_w,lbdT_w,lbd0_r,lbdT_r,
     * lbd_ratios,lambda_r,kappa_r,rhocp_av
      integer isolid

     do j=1,nx
        vd(j) = 0.0d0
        vs(j) = 0.0d0
        if (iw.eq.0) then ! constant w
       w = w0
        else
!       user defined w
!       w = ...
        end if

        if (iq.eq.0) then ! constant q
          vq = q0/(por(j)*area(j))
        else
!       user defined v
!       vq = ...
        end if

      vd(j)=vd(j)-(w0*(1-por0)*porX)/((1-porX)*por(j))+vq
      vs(j)=vs(j)+w0*(1-por0)/(1-por(j))
```

```
          dmix = aL*dabs(vq)          ! dispersion

          if(idb.eq.0) then                    ! bioturbation
            db = db0
       else
        ! user defined bioturbation coefficient
!       db = ...
        db = db0/2.0d0*erfcc((x(j)-dbdepth)/attdb)
c        db = db0/2.0d0*erfcc((x(j)-40.0d0)/1.0d0)
c          db=0.1d0
c          if (x(j).gt.15.0d0) db=0.d0
          end if

       do k = 1,ncomp
            disp(k,j) = 0.0d0

        fac_sal = (9.5d-01 - 1.d-03 * salin)


!               dsol = fac_sal*dsol_0(k)*(1.d0+f_T(k)*t_celsius)! Dmol(T,S)
          dsol = fac_sal*dsol_0(k)*(1.d0+f_T(k)*(temp_kelvin(j)-273.15))
               dsol = dsol/(1.0d0-dlog(por(j)*por(j)))                    ! in situ Dmol



               if (i_hitemp.eq.1) then !!IF HI TEMP ACTIVATED
                                                    !! THEN MAKE
CALCULATIONS USING
       !!                                           !! NON LINEAR
RELATIONSHIPS



          dyn_vis_0=2.414E-4*10**(247.8/(temp_kelvin(j)-140))

          if (k.eq.1)      then                    !IF SPECIES 1 IS O2
               dsol=0.148911091*temp_kelvin(j)/(dyn_vis_0*Vb_O2)
          else if (k.eq.2) then                !IF SPECIES 2 IS CH4
               dsol=0.148911091*temp_kelvin(j)/(dyn_vis_0*Vb_CH4)
          else if (k.eq.3) then          !IF SPECIES 3 IS CO2
               dsol=0.148911091*temp_kelvin(j)/(dyn_vis_0*Vb_CO2)
          else if (k.eq.5) then          !IF SPECIES 5 IS H2
               dsol=0.148911091*temp_kelvin(j)/(dyn_vis_0*Vb_H2)
          else if (k.eq.6) then          !IF SPECIES 6 IS H2S
               dsol=0.148911091*temp_kelvin(j)/(dyn_vis_0*Vb_H2S)

          !!!!CALCULATES THE TRACER DIFFUSION COEFFICIENT OF NON-
ELECTROLYTE SPECIES
```

```
        else if (k.eq.4) then              !IF SPECIES 4 IS CO3
                lim_con_CO3=10**7*far*1*echar/
     &          (6*3.14159*dyn_vis_0*254E-10)

                dsol=31548960*R_gas*temp_kelvin(j)*lim_con_CO3/
     &                  (1*far*far)

        else if (k.eq.7) then              !IF SPECIES 7 IS HCO3
                lim_con_HCO3=10**7*far*1*echar/
     &          (6*3.14159*dyn_vis_0*226E-10)

                dsol=31548960*R_gas*temp_kelvin(j)*lim_con_HCO3/
     &                  (1*far*far)

        else if (k.eq.8) then              !IF SPECIES 8 IS H+
                lim_con_Hplus=10**7*far*1*echar/
     &          (6*3.14159*dyn_vis_0*26E-10)

                dsol=31548960*R_gas*temp_kelvin(j)*lim_con_Hplus/
     &                  (1*far*far)

        else if (k.eq.9) then              !IF SPECIES 9 IS HS-
                lim_con_HS=10**7*far*1*echar/
     &          (6*3.14159*dyn_vis_0*238E-10)

                dsol=31548960*R_gas*temp_kelvin(j)*lim_con_HS/
     &                  (1*far*far)

        else if (k.eq.11) then             !IF SPECIES 11 IS OH-
                lim_con_OH=10**7*far*1*echar/
     &          (6*3.14159*dyn_vis_0*212E-10)

                dsol=31548960*R_gas*temp_kelvin(j)*lim_con_OH/
     &                  (1*far*far)

        else if (k.eq.12) then             !IF SPECIES 12 IS SO42-
                lim_con_SO4=10**7*far*2*echar/
     &          (6*3.14159*dyn_vis_0*231E-10)

                dsol=31548960*R_gas*temp_kelvin(j)*lim_con_SO4/                !dsol in
cm2/yr (therefore multiplied by 31548960)
     &                  (2*far*far)

        !! CALCULATES THE DIFFUSION COEFFICIENT OF IONS AND
ELECTROLYTES

        else if (k.eq.10) then !! IF SPECIES IS TEMPERATURE
                                                !! THIS NUMBER NEEDS TO BE ADAPTED
FOR EACH PROBLEM
```

```
      !! CHECK SPECIES NUMBER OF TEMPERATURE AT TEMP.F

                        lbdT_w=3E-14*(temp_kelvin(j)-273.15)**5-2E-11*
     &                 (temp_kelvin(j)-273.15)**4+2E-8*
     &                 (temp_kelvin(j)-273.15)**3-1E-5*
     &                 (temp_kelvin(j)-273.15)**2+0.0021*
     &                 (temp_kelvin(j)-273.15)+0.574
                        lbd0_r=lbd25_r*(1.007+25*(0.0037-0.0074/lbd25_r))
                        lbdT_r=lbd0_r/(1.007+(temp_kelvin(j)-273.15)*
     &                   (0.0036-0.0072/lbd0_r))
                        lbd_ratios=(1-lbdT_w/lbdT_r)/(2+lbdT_w/lbdT_r)
                        lambda_r=lbdT_r*(1-2*por(j)*lbd_ratios)/
     &                         (1+por(j)*lbd_ratios)
                        rhocp_av=por(j)*rhocp_f+(1-por(j))*rhocp_r
                        kappa_r=lambda_r/rhocp_av


                        disp(k,j)=kappa_r  !!! CAREFUL!!!!!!!!!!!!



c                       write(*,*) "kappa_r= ",kappa_r


      end if  ! end IF SELECTION OF SPECIES FORMULATION



                    if (k.ne.10) then  ! IF IS NOT TEMPERATURE, THEN CORRECT
FOR SALINITY AND TORTUOSITY

                        fac_sal = (9.5d-01 - 1.d-03 * salin)
                        dsol=dsol*fac_sal
                        dsol=dsol/(1.0d0-dlog(por(j)*por(j)))

                    end if



            end if !end IF HI TEMPERATURE


            if (k.ne.10) then  ! IF IS NOT TEMPERATURE, THEN CORRECT FOR
SALINITY AND TORTUOSITY

            isolid=0
            call issolid(k,isolid)    ! set isolid to 1 if k is a solid

            if (isolid.eq.1) then
          disp(k,j) = db
```

```
              if (dsol.gt.0.0d0) then
                write(*,*) 'molecular diffusion for solid? ok...'
                disp(k,j) = disp(k,j)+dsol
                pause 'hit any key to continue'
              end if
            else
                  disp(k,j) = dmix + dsol + db
                end if


        end if  ! IF IS NOT TEMPERATURE...



      enddo  ! do k = 1,ncomp

    enddo ! do j=1,nx

c**********************************************************************
c   additional properties outside the domain                         *
c   required for flux boundary conditions, done by linear extrapolation*
c**********************************************************************
     do ii=1,2
          if (ii.eq.1) then
            i = 1
            id = -1
          end if
          if (ii.eq.2) then
            i = nx
            id = 1
          end if
      vs(i+id)=vs(i)+(vs(i-id)-vs(i))/(x(i-id)-x(i))*(x(i+id)-x(i))
      vd(i+id)=vd(i)+(vd(i-id)-vd(i))/(x(i-id)-x(i))*(x(i+id)-x(i))
          do k=1,ncomp
        disp(k,i+id) = disp(k,i) +
    +        (disp(k,i-id)-disp(k,i))/(x(i-id)-x(i))*(x(i+id)-x(i))

                if (dabs(disp(k, i+id)).lt.1.0d-30) then
               disp(k,i+id)=0.0
                end if

          end do
        end do

c**********************************************************************
c overwrite ghost points here below if desired                       *
c the depth of the ghost points is set in gridsetup.f                *
c**********************************************************************
!      vs(0) =
!          vd(0) =
```

```
!         vs(nx+1) =
!         vd(nx+1) =
!         do k=1,ncomp
!           disp(k,0) =
!           disp(k,nx+1) =
!         end do


c*************************************************************************
c   check of physics: 0>=disp                                          *
c*************************************************************************
     do ii=0,nx+1
           do k=1,ncomp
        if (disp(k,ii).lt.0.0d0) then
              write(*,*) 'disp<0->set to 0', ii, x(ii),k
              disp(k,ii)=0.0d0
                    !stop
            end if
       end do
          end do

          end


c*************************************************************************
c   complimentary error function as function available                 *
c   based on Chebyshev fitting, taken from Press et al.                *
c   promoted to double precision                                      *
c*************************************************************************
      FUNCTION erfcc(x)
      REAL*8 erfcc,x
      REAL*8 t,z
      z=dabs(x)
      t=1./(1.d0+0.5d0*z)
      erfcc=t*dexp(-z*z-1.26551223d0+t*(1.00002368d0+t*(.37409196d0+t*
     *(.09678418d0+t*(-.18628806d0+t*(.27886807d0+t*(-1.13520398d0+t*
     *(1.48851587d0+t*(-.82215223d0+t*.17087277d0)))))))))
      if (x.lt.0.d0) erfcc=2.d0-erfcc
      return
      END
```

```
c               TRANSPORT coefficients

c*********************************************************************
c       the transport equation is discretized and written in matrix form *
c     Amat*Cvect = dvect, where Amat turns out to be tridiagonal       *
c     the steady state coefficients are similar to the transient ones  *
c     except that components due to the time derivative are not added  *
c     see separate documentation file for details what is solved (&how)*
c                                                *
c     CM, July 2002                                    *
c*********************************************************************

      SUBROUTINE transcoeff_MT(k,aa,bb,c,di)

          include 'common_geo.inc'
      include 'common.inc'
      include 'common_drive.inc'

      real*8 DI(nx),AA(nx),C(nx),BB(nx),alphirr(nx)
          integer itransp,isolid
          real*8 vap,vam,va,ma,mb,mc,gradD,grade,gradv,ep,em,ea,gb,gac,
     &       gd, vvv, deltaxx, deltaxup, deltaxdown

c*********************************************************************
c       no transport ?                                   *
c     if itransp is <> 0 after the call to notransport, the species is *
c     not being transported at all. If so, set all coefficients to 0,  *
c     note that in the transient code you never get here for a species *
c     that is not transported (saves time), and it is done here only   *
c     for the steady state problem                       *
c                                                *
c     CM, July 2002                                    *
c*********************************************************************
      itransp = 0
          call notransport(k,itransp)      ! itransp set to 1 if not transported
          if (itransp.ne.0) then
!       do j=1,nx,2


        do j=3,nx-2,2       ! only interior, else tridag fails
             aa(j) = 0.0D0
          bb(j) = 1.0d0 ! 0.0D0
          c(j)  = 0.0D0
          di(j) = co(j) ! 0.0d0
        end do


            bb(1) = 1.0d0
            di(1) = sp(k,1)
            aa(1) = 0.d0
```

```
            c(1)  = 0.d0
            bb(nx) = 1.0d0
            di(nx) = sp(k,nx)
            aa(nx) = 0.d0
            c(nx)  = 0.d0
            return
        end if


            if (ixirr.eq.0) then

            do i=1,nx
                    alphirr(i)=0.d0
            enddo

            else if (ixirr.eq.1) then

            do i=1,nx
                    alphirr(i)=alph0*exp(-xirratt*x(i))
            enddo

            else if (ixirr.eq.2) then

            do i=1,nx
                    alphirr(i)=alph0*exp((xirr1-x(i))/xirr2)/(1+exp((xirr1-x(i))/xirr2))
            enddo

            end if


c           xirr=0.7D0                                          !MT irrigation
c           x1=7.0
c           x2=0.8
c           do i=1,nx                                           !MT irrigation
c                   alphirr(i)=alph0*exp(-xirr*x(i))        !MT irrigation
c                   alphirr(i)=alph0*exp((x1-x(i))/x2)/(1+exp((x1-x(i))/x2))

c                   write(*,*) alphirr(i), i, x(i)
c           enddo                                               !MT irrigation
c***********************************************************************
c           regular transport                                   *
c     - half timestep if doing strang splitting                 *
c     - check if a species is a solid (isolid=1) or a solute,   *
c       because this has an effect on the selection which transport    *
c       parameters and theta (por*area or (1-por)*area) is used       *
c     - then calculate the coefficients in the interior of the domain  *
c     - then calculate the boundary nodes                       *
c     - add time dependence                                     *
c     - double timestep again (restore) if doing strang splitting      *
c                                                               *
```

```
c     CM, July 2002                                          *
c*************************************************************************


c*************************************************************************
c     half time step if doing strang splitting (restore at the bottom) *
c*************************************************************************
      if (isplit.eq.1) then
            delt = delt*0.5d0
           end if

c*************************************************************************
c     solid species?                                         *
c*************************************************************************
      isolid = 0
           call issolid(k,isolid)      ! 1 indicates solid

c*************************************************************************
c     interior nodes                                         *
c*************************************************************************
      do j=3,nx-2
            deltaxx=x(j+1)-x(j-1)
            deltaxdown=x(j)-x(j-2)
            deltaxup=x(j+2)-x(j)

       if (k.eq.10) then !! IF SPECIES IS TEMPERATURE
                                                    !! THIS NUMBER NEEDS TO BE ADAPTED
FOR EACH PROBLEM
          !! CHECK SPECIES NUMBER OF TEMPERATURE AT TEMP.F

          vvv=vd(j)*(rhocp_f/rhocp_r) ! vd(j)-(w0*(1-por0)*porX)/((1-porX)*por(j))+vq
           !! direct advection velocity is not affecting temperature
              eta=por(j)
              ai=alphirr(j)

           else  !! IS SPECIES IS NOT TEMP, THEN PROCEED AS USUAL
        if (isolid.eq.1) then                ! get the right advection velocity and eta
              eta=(1-por(j))
                    vvv= vs(j)
                    ai=0.
            else
                    vvv= vd(j)
             eta=por(j)
                    ai=alphirr(j)
            end if

      end if ! END OF IF STATEMENT REGARDING IF SPECIES IS TEMP.


            aa(j) = (-vvv/deltaxx - (disp(k,j)+disp(k,j-2))/2/
```

```
     &     (deltaxx*deltaxdown))*delt
           bb(j) = 1 + (vvv + ai*deltaxx + (disp(k,j)+disp(k,j-2))
     &                 /2/deltaxdown
     &                 +(disp(k,j)+disp(k,j+2))/2/deltaxup)*delt/deltaxx
       c(j) = -(disp(k,j)+disp(k,j+2))/2/(deltaxx*deltaxup)*delt
           di(j) = sp(k,j) + ai*spb(k,1)*delt

          end do

c*************************************************************************
c     boundary nodes                                    *
c*************************************************************************
      do ii=1,2

           if (ii.eq.1) then
                 j=1
                 deltaxup=(x(3)-x(1))
           endif
           if (ii.eq.2) then
                 j=nx
                 deltaxdown=(x(nx)-x(nx-2))
           endif

c*************************************************************************
       ! fixed concentration
c*************************************************************************
       if (ibc(k,ii).eq.0) then
         aa(j) = 0.0d0
            c(j) = 0.0d0
            bb(j) = 1.0d0
            di(j) = spb(k,ii)
           else
                 deltaxx=x(j+1)-x(j-1)

c*************************************************************************
        ! flux or gradient condition
c*************************************************************************
        if (isolid.eq.1) then      ! get the right velocity and eta
              vvv = vs(j)
        else
              vvv=vd(j)
        end if


c*************************************************************************
        ! known gradient
            if (ibc(k,ii).eq.1) then
          aa(j)= (-vvv/deltaxx - disp(k,j)/(deltaxx*2*(x(j)-x(j-1))))
     &           *delt
            bb(j)= 1 + (vvv/deltaxx + disp(k,j)/(deltaxx*2*(x(j)-x(j-1))))
```

```
     &                *delt
               c(j)=0.
               di(j)=sp(k,j)+spb(k,ii)*disp(k,j)*2*delt/deltaxx
             end if
c*************************************************************************
             ! known flux (advective and diffusive)
             if(ibc(k,ii).eq.2) then
                   if (j.eq.1) then
                         aa(j)= 0.
                         bb(j)= 1 + (vvv/deltaxx + (disp(k,j)+disp(k,j+2))/2
     &                   /(deltaxx*deltaxup))*delt
            c(j) = -(disp(k,j)+disp(k,j+2))/2/(deltaxx*deltaxup)*delt
                di(j)=sp(k,j)+spb(k,ii)*delt/(eta*(x(j+1)-x(j-1)))
                   else
                     aa(j)=(-vvv/deltaxx - (disp(k,j)+disp(k,j-2))/2
     &                         /(deltaxx*deltaxdown))*delt
                         bb(j)=1 + (disp(k,j)+disp(k,j-2))/2
     &                         /(deltaxx*deltaxdown)*delt
                         c(j)=0.
                         di(j)=sp(k,j)+spb(k,ii)*delt/(eta*(x(j+1)-x(j-1)))
                   end if
              end if
             end if
           end do

c*************************************************************************
c     restore time step if doing strang splitting                *
c*************************************************************************
      if (isplit.eq.1) then
            delt = delt*2.0d0
           end if

!          if (k.eq.1) then
!            write(*,*) 'show'
!          if (co(nx-2).lt.0.505d0) then
!                   write(*,*) 'show'
!      end if
!          end if


      RETURN
      END
```